Diseño de polianilinas nanoestructuradas para aplicaciones termoeléctricas y sensores

Autora: Laura Horta Romarís

Tesis doctoral UDC / 2018

Directoras: Dra. María José Abad López Dra. Victoria González Rodríguez

Programa regulado por el RD 99/2011:

Programa oficial de doctorado interuniversitario en Física Aplicada

UNIVERSIDADE DA CORUÑA

A mi increíble y querida familia

AGRADECIMIENTOS

Hace tres años, comenzaba una nueva etapa de mi vida llena de aprendizaje y desarrollo científico y personal. Ahora esta etapa termina con la presentación de esta tesis doctoral y aunque estas líneas aparezcan en el inicio son las últimas en ser escritas, quiero dejar patente mi agradecimiento a todos aquellos que de un modo u otro han contribuido a la realización de esta tesis, ya que no tengo duda de que este trabajo también les pertenece.

A los directores del Centro de Investigaciones Tecnológicas, Dr. José Manuel Vilariño y Dra. Anne Gosset, a los directores del Departamento de Física y Ciencias de la Tierra, Dr. Joaquín López y Dr. Óscar Cabeza, por permitir el desarrollo de esta tesis doctoral. Al director del Grupo de Polímeros, Dr. Luis Barral, y por extensión, a todos sus miembros, por darme la oportunidad de trabajar y aprender con ellos.

A Dr. Senentxu Lanceros, Dr. Pedro Costa, João Teixeira y todo el grupo ESM (Universidade do Minho), por su colaboración y asesoramiento, durante mi estancia en Portugal y también después de ella, gracias.

Al Dr. Francisco Rivadulla y a sus compañeros del CIQUS (USC) por permitirme hacer las medidas de Seebeck y aportarnos una visión más completa y rigurosa de la parte más abstracta de nuestro estudio.

A mis magníficas directoras de tesis, Dra. Victoria González y Dra. María José Abad. A Victoria gracias por tener paciencia y escucharme en todas mis dudas, ensayos, terquedades, reflexiones y por darme aliento con los experimentos más complejos. A María por tus conocimientos y sobre todo, por saber transmitirlos, ayudándome con todas mis dudas, por ser mi guía, por tus buenos consejos tanto en lo laboral como en personal. Gracias por la orientación, el apoyo y todo lo que he aprendido de vosotras. No puedo estar más agradecida de la oportunidad que me habéis dado, de lo que he crecido tanto personal como en lo profesional, del cariño y apoyo que he recibido, por vuestra cercanía, porque siento que en Ferrol se queda parte de mi familia.

A Dra. Aurora Lasagabáster, imposible no cogerte cariño, gracias por todo lo que nos divertimos contigo, tu espontaneidad, y sobre todo por tu rigurosa forma de enseñar,

tu perfección innata y por el esfuerzo que le has dedicado a esta tesis. A Dra. Ana Ares, por tu saber escuchar, tus anécdotas con las que siempre nos reímos, tus buenos consejos, y ayudarme en todo lo que estuviera de tu mano y como no, por nuestro viaje a Croacia. A Paula, por todo, no hay palabras que lleguen para expresar todo lo que me has dado y lo mucho que te quiero, por los buenos momentos y no tan buenos, por ser una de mis alegrías diarias, por tu fuerza contagiosa y por todo el amor que nos das, ¡gracias!. A Xoán, porque… "¿qué haríamos sin ti en el laboratorio?" Gracias por tu profesionalidad y sobre todo por enseñarme y ayudarme en todo lo que he necesitado. A Rosalía, por su complicidad y ser mi apoyo en la primera etapa de esta tesis. A Dra. Sonia Dopico también agradecerte darme respuesta en todas mis dudas durante el inicio de esta etapa. A Fini, en primer lugar, por tu ayuda en el laboratorio, por tu apoyo sobretodo en mi primera etapa de esta tesis, por plena confianza que me has dado y espero haber sabido responderte, te estoy especialmente agradecida. A Alejandra y a Elena por transmitirme tan buena energía en esta última etapa de tesis.

En realidad, todos vosotros miembros del laboratorio, tanto de plásticos como de química, os considero parte de mi familia, me alegro de haber compartido estos años a vuestro lado y de que me ayudarais a seguir aprendiendo de la vida en todos sus aspectos y tener tan buen recuerdo de esta etapa, siempre os tendré en mi corazón.

A mis amigas y amigos por estar siempre ahí y por los buenos momentos que pasamos que hacen que todo sea más fácil.

Finalmente quiero dedicar esta tesis a mi familia, porque siempre habéis creído en mí, no puedo ser más afortunada de la piña que somos. A mis padres, a mis abuelos y abuelas por la educación que me han dado y su amor constante e incondicional. Sin ellos nada de esto sería posible. A mis hermanas, Alicia e Irene, lo sois todo para mí. A Joaquín por sacarme siempre una sonrisa y ser uno de los motivos de mi felicidad.

¡Muchísimas gracias a todos!

RESUMEN

Dentro del conjunto de los polímeros intrínsecamente conductores, la polianilina (PANI) presenta una gran versatilidad en cuanto a su síntesis y propiedades que la hacen adecuada para un amplio campo de aplicaciones.

Dentro de este contexto, la presente tesis tiene como objetivo el diseño y caracterización de nuevas polianilinas que combinen buenas propiedades (eléctricas, termoeléctricas, estabilidad térmica o piezorresistivas) con un coste asequible y con menor impacto medioambiental. Para ello se estudió la influencia del HCl, DBSA (ácido dodecilbencensulfónico) y NaSIPA (sal de sodio del ácido 5-sulfoisoftálico) como dopantes y de distintas rutas de síntesis sencillas y respetuosas con el medio ambiente, para la obtención de las PANIs. Así mismo, con el fin de mejorar las propiedades mecánicas del polímero sintetizado y reducir costes, se elaboraron nuevos materiales compuestos utilizando acetato de polivinilo como matriz polimérica y polianilina como carga conductora. Tanto las polianilinas sintetizadas como sus compuestos se han caracterizado por TGA, FTIR, Análisis Elemental, XRD y TEM. Las propiedades eléctricas, termoeléctricas y piezorresistivas se han estudiado en función del tipo de dopante, tipo de síntesis y cantidad de polianilina (en el caso de los compuestos), analizando el potencial uso de estos materiales en sensores y generadores termoeléctricos.

Entre los distintos polímeros estudiados: las PANIs dopadas con DBSA obtenidas tanto por ruta de síntesis directa como por la indirecta, muestran las mejores propiedades para su uso en sensores térmicos; sin embargo, la PANI-NaSIPA muestra la mejor eficiencia termoeléctrica; los materiales compuestos de látex con un 30% en masa de PANI-HCl presentaron la conductividad de la PANI original obteniendo un buen balance de propiedades piezorresistivas y coste económico.

RESUMO

Dentro do conxunto dos polímeros intrinsecamente condutores, a polianilina (PANI) presenta unha grande versatilidade en canto a súa síntese e propiedades que a fan axeitada para un amplo campo de aplicacións.

Neste contexto, a presente tese ten como obxecto o deseño e caracterización de novas polianilinas que combinen boas propiedades (eléctricas, termoeléctricas, estabilidade térmica ou piezorresistivas) cun custo asumíbel e con menor impacto medioambiental. Para iso, estudouse a influencia do HCl, DBSA (ácido dodecilbencensulfónico) e NaSIPA (sal de sodio do ácido 5-sulfoisoftálico) coma dopantes e distintas rutas de síntese, sinxelas e respectuosas co medio ambiente, na obtención das polianilinas. Ase mesmo, co fin de mellorar as propiedades mecánicas do polímero sintetizado e reducir custos, elaboráronse novos materiais compostos empregando acetato de polivinilo como matriz polimérica e a PANI como carga condutora. Tanto as polianilinas sintetizadas coma os seus compostos, caracterizáronse por TGA, FTIR, análise elemental, XRD e TEM. As propiedades eléctricas, termoeléctricas e piezorresistivas estudáronse en función do tipo de dopante, tipo de síntese e cantidade de polianilina (no caso dos compostos), para avaliar o potencial uso destes materiais en sensores e xeradores termoeléctricos.

Entre os distintos polímeros estudados: as PANIs dopadas con DBSA, obtidas tanto por ruta de síntese directa como pola indirecta, amosaron as mellores propiedades para seu uso en sensores térmicos; con todo, a PANI-NaSIPA mostra a mellor eficiencia termoeléctrica; namentres que os materiais compostos de látex cun 30% en masa de PANI-HCl presentaron a condutividade da PANI orixinal, obtendo un bo balance entre as propiedades piezorresistivas e custo económico.

ABSTRACT

Among the class of materials known as intrinsically conducting polymers, polyaniline (PANI) stands out due to the great versatility of synthetic methods and properties which greatly enlarge its fields of applications.

Within this context, the scope of the present doctoral thesis is the design and characterization of novel polyanilines which combine suitable physical properties (electrical conductivity, thermoelectric performance, thermal stability or piezoresistivity) with affordability and less environmental impact. In order to fulfill this aim, the first part of this work studies the influence on PANI properties of HCl, dodecylbenzenesulfonic acid (DBSA) and 5- sulfoisophtalic acid sodium salt (NaSIPA) as dopants and several simple and ecofriendly synthetic routes. Furthermore, with the purpose of improving the mechanical properties of PANI together with cost reduction, new composite materials were designed using poly(vinyl acetate) (PVAc) as polymer matrix and PANI as conductive filler. Both doped PANIs and the PANI-PVAc composites had been analyzed by means TGA, FTIR, Elemental Analysis, XRD and TEM. The electrical, thermoelectric and piezoresistive properties had been studied as a function of the type of dopant, synthetic route and PANI content, in the case of the PANI-PVAc composites, so as to evaluate the potential application of these materials as sensors and thermoelectric generators.

As a conclusion, PANI doped with DBSA and synthesized either by the so called “direct” or “indirect” routes, are the best candidates for thermal sensors; however, PANI-NaSIPA offers the highest thermoelectric efficiency, whereas polyaniline–poly(vinyl acetate) latex nanocomposites (PANI– PVAc) with 30% PANI-HCl (weight%), which preserve the conductivity values of pristine PANI, present a worthy compromise between piezoresistive properties and affordability.

ÍNDICE:

Índice

Capítulo 1: Introducción

1. Polímeros conductores ... 3
1.1. Polímeros intrínsecamente conductores ... 3
2. Compuestos poliméricos conductores ... 14
2.1. Conducción eléctrica y percolación ... 15
3. Polímeros conductores en termoelectricidad ... 19
3.1. El conflicto de las propiedades termoeléctricas ... 23
3.2. Generador termoeléctrico: funcionamiento, eficiencia y diseño ... 31
4. Polímeros conductores en sensores ... 34
Referencias ... 37

Capítulo 2: Objetivos

1. Relevancia de los objetivos propuestos ... 50
2. Estructura de la memoria de la tesis ... 51

Capítulo 3: Cyclic temperature dependence of electrical conductivity in polyanilines as a function of the dopant and synthesis method

1. Introduction ... 55
2. Experimental ... 56
2.1. Materials synthesis ... 56
2.2. Characterization ... 57
3. Results and discussion ... 59
3.1. Morphological properties ... 59
3.2. Chemical composition by FTIR, elemental analysis and XPS ... 61
3.3. X-ray diffraction studies ... 66
3.4. Thermal behavior ... 68
3.5. Thermal stability of DC conductivity ... 70
4.Conclusions ... 75
Supplementary material ... 76
References ... 77

Capítulo 4: Thermoelectric properties and intrinsic conduction processes in DBSA and NaSIPA doped polyanilines

1. Introduction ... 83
2. Experimental ... 85
2.1. Materials synthesis ... 85
2.2. Characterization ... 85
3. Results and discussion ... 88
3.1. Electrical conductivity ... 88

3.2. Seebeck coefficient 92
3.3. Thermal conductivity 95
3.4. Figure of merit 96
4. Conclusions 98
Supplementary material 99
References 108
Capítulo 5: Multifunctional electromechanical and thermoelectric polyaniline-poly(vinyl acetate) latex composites for wearable devices
1. Introduction 111
2. Experimental 113
2.1. Materials 113
2.2. Composite preparation 113
2.3. Composite characterization 114
3. Results and discussion 117
3.1. Morphological and structural characterization 117
3.2. Electrical properties 123
3.3. Thermoelectric properties 124
3.4. Mechanical properties 125
3.5. Thermal stability 126
3.6. Electromechanical response 127
3.7. Thermoresistive properties 130
4. Conclusions 132
Supplementary material 133
References 138
Capítulo 6: Conclusiones 144
Anexos
I-Financiación recibida 148
II-Contribuciones a congresos 152
III-Portada de artículos 155

Índice de figuras

Capítulo 1

Figura 1. Estructura del poliacetileno (PA) y su monómero el etileno. 4
Figura 2. Estructura de polímeros intrínsecamente conductores típicos. 5
Figura 3. Efecto del dopaje en polímeros conductores. 5
Figura 4. Diagrama energético de bandas de un semiconductor. 6
Figura 5. Diagrama energético de la formación del polaron, bipolaron y las bandas de bipolaron en función del nivel de dopaje. 7
Figura 6. Unidades repetitivas dentro de la estructura de la PANI. 8
Figura 7. Polimerización química de la anilina. 9
Figura 8. Diferentes formas de la PANI A) antes de la protonación, B) después de la protonación, y C) formación del bipolaron y D) polaron 10
Figura 9. Camino de conducción de la PANI donde los signos positivos representan el radical catión N como un hueco y los signos negativos representan un N neutro 10
Figura 10. Estructura heterogénea de PANI. 11
Figura 11. Mecanismos de transporte intra e intercadena. 12
Figura 12. CPCs según su conductividad eléctrica y aplicaciones . 14
Figura 13. Esquema de distribución de (a) red segregada y (b) aleatoria en un CPC. 17
Figura 14. ZT de los TE inorgánicos típicos en función de los años . 21
Figura 15. ZT de materiales TE orgánicos: poli(3,4–etilendioxi–tiofeno) (PEDOT), polianilina (PANI) y polipirrol (PPY). Número de artículos publicados en TE orgánicos en los últimos 20 años según las bases de datos de Scopus y Web of Science 23
Figura 16. Densidad de estados en un polímero conductor incluyendo los estados extendidos y localizados. 25
Figura 17. Optimización de ZT según el nivel dopaje. 26
Figura 18. Efecto del dopaje secundario en la conformación del material antes de la adición del dopante (a) y después (b y c) 29
Figura 19. A) Efecto termoeléctrico y B) unión p-n. 31
Figura 20. Generador termoeléctrico inorgánico. 32
Figura 21. Materiales termoeléctricos orgánicos (OTE) compatibles con procesado 2D fácilmente personalizable en distintas conformaciones. 33

Capítulo 3

Figure 1. TEM images of the PANI samples showing their morphology: A) PANI-HCl (P1), B) PANI-DBSA direct synthesis (P2), C) PANI- DBSA indirect synthesis (P3) and D) PANI-NaSIPA (P4). The magnification is 6000x and the scale bar in the Figures is 5µm. The insets magnification is 50000x and the corresponding scale bar is 500 nm. 60

Figure 2. A) PANI emeraldine base (EB) and its different protonated forms. B) FTIR spectra of PANI bases and PANI salts: PANI-HCl (P1), PANI-DBSA direct synthesis (P2), PANI-DBSA indirect synthesis (P3) and PANI-NaSIPA (P4).....63

Figure 3. TGA and DTG curves (A) and temperature intervals with corresponding weight losses for the different degradation events (B) of PANI-HCl (P1), PANI-DBSA direct synthesis (P2), PANI-DBSA indirect synthesis (P3) and PANI-NaSIPA(P4) samples from 35 to 700 ºC at 10 ºC/ min under oxygen atmosphere. 69

Figure 4. DC conductivity behavior as a function of temperature: A) from 25 to 200 °C at 2 ºC/min for PANI-HCl (P1), PANI-DBSA direct synthesis (P2), PANI-DBSA indirect synthesis (P3) and PANI-NaSIPA (P4) samples. B) from 50 to 350 °C at 10ºC/min for P2 and P3 samples. 72

Figure 5. Cyclic temperature dependence of the DC electrical conductivity between 30 to 70 ºC for A) PANI-DBSA direct synthesis (P2) and B) PANI-DBSA indirect synthesis (P3). 74

Figure S1. Normalized X-ray diffraction patterns for the polyaniline emeraldine base (P1 Base) and its different protonated forms: PANI-HCl (P1), PANI-DBSA direct synthesis (P2), PANI-DBSA indirect synthesis (P3) and PANI-NaSIPA (P4). 76

Capítulo 4

Figure 1. Chemical structure of PANI-base and doped polyanilines, PANI-NaSIPA and PANI-DBSA. 86

Figure 2. Electrical conductivities of PANI-DBSA and PANI-NaSIPA at various molar acid concentrations at room temperature.....88

Figure 3. S/N ratio calculated by elemental analysis as a function of the molar acid concentration. 89

Figure 4. Schematic drawing proposed for the layered structure of PANI-DBSA. 91

Figure 5. TEM images of A) PANI-DBSA 1.25M_50Kx and B) PANI-NaSIPA 1.25M_50Kx. 92

Figure 6. Seebeck coefficients of PANI-DBSA and PANI-NaSIPA at various molar concentrations at room temperature. 93

Figure 7. Temperature dependence of the Seebeck coefficient of PANI-DBSA 1M and PANI-NaSIPA 0.5M. 93

Figure 8. Thermal conductivity of A) PANI-DBSA B) PANI-NaSIPA at 300, 325 and 350 K.....95

Figure 9. ZT values of PANI-DBSA and PANI-NaSIPA at different acid molar concentrations and 300 K. ..97

Figure S1. Scheme of the home-made device that measures the Seebeck coefficient. 99

Figure S2. Voltage before and after applying current (A) and adjustment of voltage curves after applying thermal gradient (B). 100

Figure S3. Correlation between electrical conductivity and doping level for PANI-DBSA.....101

Figure S4. Normalized FTIR spectra of PANI-base and PANI protonated with increasing amounts of DBSA. 102

Figure S5. Normalized FTIR spectra of PANI-base and PANI protonated with increasing amounts of NaSIPA in the spectral range between 1900-600 cm^{-1}. 102

Figure S6. Correlation between the red shift of the bencenoid band wavenumber and doping level of PANI-DBSA (R^2=0.85) (A) and PANI-NaSIPA (R^2=0.99) (B). 103

Figure S7. XRD patterns of PANI salts prepared with increasing DBSA (A) and NaSIPA (B) molar concentrations. 104

Figure S8. A) Variation of the intensity of the layer ordering reflections of PANI-DBSA as a function of the doping level; B) Variation of the d spacing of the layer ordering reflections of PANI-DBSA as a function of the doping level. 106

Capítulo 5

Figure 1. TEM images of A) PVAc latex film and B) P30L70 dispersion at x15000 magnification and C) P30L70 x40000 magnification. 118

Figure 2. AFM micrographs of P30L70 obtained with a conductive tip. Two types of distinct surface structures 3D (A and B) and 2D (D and E) respectively for: A) topography; B) electrical current intensity; C) Example of the C-AFM measurement. 119

Figure 3. FTIR spectra of PANI, PVAc latex and the composite film P30L70: A) between 3700 and 2600 cm^{-1} and B) 1800 and 600 cm^{-1} 120

Figure 4. Fraction of bound carbonyl groups ($\boldsymbol{fb}$) of PVAc versus wt.% PANI from a fit of two Gaussian bands to the carbonyl region of the ATR spectra. The dashed line is an exponential fit to the data. 121

Figure 5. X-ray diffraction patterns of PVAc film, neat PANI, and PANI-PVAc composites of increasing PANI content. 122

Figure 6. Composite electrical conductivity (σ) (in semi-log plot, green circles) and Seebeck coefficient (blue squares) as a function of the volume fraction of PANI(%) (ρ). The insert shows a log–log plot of the composite conductivity as a function of $\rho-\rho_c$, where σ_0 is the effective conductivity of PANI within the matrix; ρ_c is the percolation threshold and t is the critical exponent dependent on the dimensions of the lattice. 123

Figure 7. Illustration of electromechanical behaviour: A) Cycles for P10L90 for 5% of deformation at 5 $mm \cdot min^{-1}$ and B) GF sensitivity (Eq. 3) as function of the PANI content in the composites. 128

Figure 8. Piezoresistive sensitivity of PANI-PVAc composites: A) GF of P10L90 up to 10% strain and P20L80 and P30L70 up to 20% strain at 5 $mm \cdot min^{-1}$; B) GF up to 5% of deformation at several velocities (1, 5 and 10 $mm \cdot min^{-1}$); C) GF as a function of the number of cycles; D) Cycle stability of the piezoresistive response of P10L90 at 5% deformation and 5 $mm \cdot min^{-1}$ over 100 cycles. 130

Figure 9. Thermoresistive behaviour of P10L90 from 20 to 40 °C (A) and from 20 to 100 °C (B) at 10 $°C \cdot min^{1}$. 131

Figure S1. A) Carbonyl region of the FTIR absorption spectra of composites of increasing PANI concentration. The intensities of the spectra are normalized with respect to the peak of free C=O; B) Fit of two Gaussians to the data for the P30L70 film. The areas under the two peaks are assigned to bound ($\nu_{C=O\cdots HN}$) and free ($\nu_{C=O}$) carbonyl groups. 133

Figure S2. Shifts of PANI FTIR bands upon increasing the PANI %wt in PANI-PVAc composites: A) wanumbers of the δ_{NH^+} (squares) and Quinoid band (Q) (circles) and B) bencenoid band (B). 135

Figure S3. Stress-strain curves until rupture of pure PVAc and PANI-PVAc composites: P10L90, P20L80 and P30L70 136

Figure S4. Changes in conductivity of P10L90, P20L80 and P30L70 composites after tensile testing. 137

Figure S5. TGA and DTG (inset) curves of PANI-HCl, PVAc and PANI-PVAc composites: P10L90, P20L80 and P30L70. 137

Índice de tablas

Capítulo 1

Tabla 1. Aplicaciones de la polianilina y sus propiedades. 13

Tabla 2. Principales materiales usados como sensores químicos basados en PANI 35

Capítulo 3

Table 1. Experimental procedure for the synthesis conditions of doped PANI 57

Table 2. XPS surface compositions (atomic percentage), doping levels and electrical conductivity of PANI salts 66

Table 3. The d-spacing, relative intensity, interchain separation, crystallite size and degree of crystallinity (X_c)-of the four PANI salts. 67

Table S1. Chemical compositions of PANI salts and base powders obtained by Elemental Analysis. S/N and C/N ratios are given on molar base. 76

Capítulo 4

Table S1. Peak positions (2θ), d-spacings (d x10^{-10}m), normalized intensities (I), crystallite size (L x10^{-10}m) and degree of crystallinity (X_c%) of PANI-DBSA samples of increasing acid molar concentration. 105

Table S2. Peak positions (2θ), d-spacings (d x10^{-10}m), normalized intensities (I), crystallite size (L x10^{-10}m) and degree of crystallinity (X_c%) of PANI-NaSIPA samples of increasing acid molar concentration. 107

Capítulo 5

Table 1. Composition of PANI-PVAc composites. 114

Table 2. Summary of the characteristic degradation temperaturas of PANI, PVAc and PANI-PVAc composites taken from the minima of DTG curves and tensile parameters from the stress-strain curves. 125

ABREVIATURAS

AFM	microscopía de fuerza atómica (*atomic force microscopy*)
APS	peroxodisulfato de amonio (*ammonium peroxodisulphate*)
BTFMSI	bis (trifluorometilsulfonil) imida (*bis(trifluoromethylsulfonyl)imide)*
Bzs	bencenosulfonato (*benzenesulfonate*)
CB	negro de carbono (*carbon black*)
CNP	nanopartículas de carbono (*carbon nanoparticles*)
CNT	nanotubo de carbono (*carbon nanotube*)
CP	polímero conductor (*conductive polymer*)
CPC	compuesto polimérico conductor (*conductive polymer composite*)
CSA	ácido canforsulfónico (*camphorsulfonic acid*)
DBSA	ácido dodecilbencensulfónico (*dodecylbenzensulfonic acid*)
DOS	densidad de estados (*density of states*)
EB	emeraldina base (*emeraldine base*)
EPDM	caucho de etileno propileno dieno (*ethylene-propylene-diene monomer*)
DMSO	dimetilsulfóxido (*dimethyl sulfoxide*)
DMF	dimetilformamida (*dimethylformamide*)
NMP	N-metil-2-pirrolidona (*N-methyl-2-pyrrolidone*)
EG	Etilenglicol (*ethylene glicol*)
ES	emeraldina sal (*emeraldine salt*)
EVA	etilenvinilacetato (*ethylene vinyl acetate*)
FTIR	espectroscopía de infrarrojo por transformada de Fourier (*Fourier-transform infrared spectroscopy*)
GF	factor de deformación (*gauge factor*)
GO	óxido de grafeno (*graphene oxide*)
H_2SO_4	ácido sulfúrico (*sulfuric acid*)
H_3PO_4	ácido fosfórico (*phosphoric acid*)
HBF_4	ácido fluorobórico (*fluoroboric acid*)
HCl	ácido clorhídrico (*hydrochloric acid*)
HNTs	nanotubos de halloysita (*halloysite nanotubes*)
HOMO	orbital molecular más alto ocupado (*highest occupied molecular orbital*)
Hz	hidracina (*hydrazine*)
ICP	polímero intrínsecamente conductor (*intrinsically conducting polymer*)
LED	diodo emisor de luz *(light emmitting diode*)
LUMO	orbital molecular más bajo ocupado (*lowest unoccupied molecular orbital*)
MWCNT	nanotubos de carbono multicapa (*multi-walled carbon nanotubes*)
NaSIPA	sal de sodio del ácido 5-sulfoisoftálico (*5-sulfoisophtalic acid sodium salt*)
NR	caucho natural (*natural rubber*)
NRB	caucho de nitrilo-butadieno (*nitrile butadiene rubber*)
NSA	ácido 2-naftalensulfónico (*2-naphthalenesulfonic acid*)
NT	nanotubo (*nanotube*)
OLED	diodo orgánico de emisión de luz (*organic light-emitting diode*)
OTE	termoeléctrico orgánico (*organic thermoelectric*)
P3HT	poli(3-hexiltiofeno-2,5-diil) (*poly(3-hexylthiophene-2,5-diyl)*)
PAA	ácido poliacrílico (*polyacrylic acid*)
PANI	polianilina (*polyaniline*)
PBMA	polimetacrilato de butilo (*butyl polymethacrylate*)
PC	policarbonato (*polycarbonate*)

PE	polietileno (*polyethylene*)
PEDOT	poli(3,4–etilendioxi–tiofeno) (*poly(3,4-ethylenedioxythiophene)*)
PEO	bloque de polietilenglicol (*poly(ethylene glycol)-block*)
PF	factor de potencia (*power factor*)
PBMA	poli(n-butil metacrilato) (*poly (butyl methacrylate)*)
PMDS	polidimetilsiloxano (*polydimethylsiloxane*)
PMMA	polimetacrilato de metilo *(poly(methyl methacrylate)*
PPO	bloque de polipropilenglicol (*(propylene glycol)-block)*
PPP	poli(p-fenileno) (*poly (p-phenylene)*)
PPV	poli(p-fenil vinileno) (*poly (p-phenyl vinylene)*)
PPY	Polipirrol (*polypyrrole*)
PS	Poliestireno (*polistyrene*)
PSS	Poliestireno sulfonado (*sulfonated polystyrene*)
P1	PANI-HCl
P2	PANI-DBSA por síntesis directa (*PANI-DBSA by direct synthesis*)
P3	PANI-DBSA por síntesis indirecta (*PANI-DBSA by indirect synthesis*)
P4	PANI-NaSIPA
PT	politiofeno (*polythiophene*)
PVA	polivinil alcohol (*polyvinyl alcohol*)
PVAc	polivinil acetato (*polyvinyl acetate*)
PVC	policloruro de vinilo (*polyvinylchloride*)
RT	temperatura ambiente (*room temperatura*)
SBR	caucho de poliestireno-butadieno (*polystyrene-butadiene rubber*)
SBS	estireno-butadieno-estireno (*styrene-butadiene-styrene*)
s-CPC	compuesto polimérico conductor segregado (segregated conductive polymer composite)
SWCNT	nanotubos de carbono monocapa *(single-walled carbon nanotube)*
TE	termoelectricidad, termoeléctrico (*thermoelectricity, thermoelectrical*)
TEG	generador termoeléctrico (*thermoelectric generator*)
TEM	microscopía electrónica de transmisión (*transmission electron microscopy*)
TGA	análisis termogravimétrico (*thermogravimetric analysis*)
Tos	anión del ácido p-toluensulfónico (tosilato) (*p-toluenesulfonic acid (tosylate*)
WOS	Web of Science
XPS	espectroscopia fotoelectrónica de rayos–X (*X–ray photoelectron spectroscopy*)
XRD	difracción de rayos X (*X–ray diffraction*)
ZT	figura de mérito (*figure of merit*)
β-NSA	ácido β-naftaleno sulfónico (β-*naphthalene sulfonic acid*)

CAPÍTULO 1:

Introducción

INTRODUCCIÓN

El desarrollo de la sociedad actual demanda más innovaciones referentes a nuevas fuentes de energía, limpias y sostenibles que se conviertan realmente, en una alternativa a los combustibles fósiles, a la energía nuclear o a la energía térmica. Dentro de este contexto los polímeros conductores pueden emplearse en dispositivos capaces de producir o almacenar energía limpia. Estos materiales presentan una baja densidad y unas buenas propiedades mecánicas, así como un bajo coste, combinación difícil de obtener con materiales convencionales de tipo metálico o cerámico.

1. Polímeros conductores

Los polímeros conductores (*conductive polymers* o *conducting polymers*, CP) combinan las propiedades de los polímeros convencionales como ligereza, bajo coste y buena procesabilidad con propiedades de conducción eléctrica [1,2] .

En este contexto, caben señalar los polímeros intrínsecamente conductores (ICP) con propiedades de conducción inherentes del material y los compuestos poliméricos conductores (CPC), donde cargas conductoras son dispersadas en una matriz polimérica aislante compuesta por uno o más tipos de polímeros [3]. Estos últimos suscitan un gran interés desde los ámbitos académico e industrial.

1.1. Polímeros intrínsecamente conductores

Según la Unión Internacional de Química Pura y Aplicada, más conocida por sus siglas en inglés IUPAC, define un polímero intrínsecamente conductor (ICP) como un polímero eléctricamente conductor compuesto de macromoléculas que tienen secuencias conjugadas de dobles enlaces a través de las cadenas [4]. Es precisamente, debido a la presencia del sistema π electrónicamente conjugado a lo que deben su capacidad de conducción, ya que se logra una deslocalización electrónica a lo largo de la cadena polimérica, que sirve como una vía para el transporte de cargas[2,5,6].

En la **Figura 1** se puede ver la estructura del ICP más simple derivado del etileno, el poliacetileno. La configuración electrónica del monómero, etileno, ayuda a comprender la presencia de dobles enlaces alternos en el polímero formado en la reacción de polimerización por adición. En la molécula de etileno, los dos átomos de C presentan 3 orbitales híbridos

sp^2 y un orbital $2p_z$ libre sin hibridar. Entre dos orbitales híbridos sp^2 de los dos átomos de carbono, se forma un enlace σ_{C-C} y los otros orbitales híbridos sp^2 se unen a átomos de hidrógeno mediante enlaces σ_{C-H}, mientras que los orbitales $2p_z$ de los dos átomos de carbono que se disponen perpendiculares al plano y se solapan lateralmente dando lugar al enlace π_{C-C}.

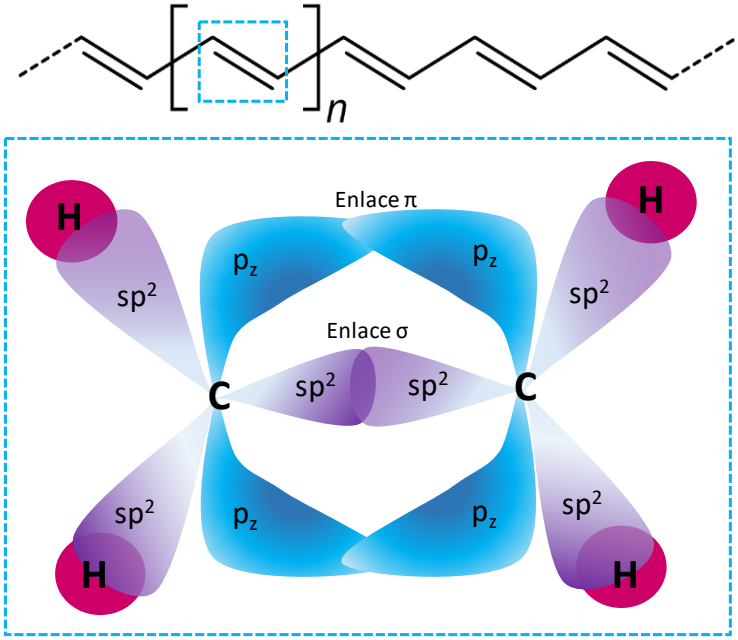

Figura 1. Estructura del poliacetileno (PA) y su monómero el etileno.

Desde el descubrimiento del poliacetileno por Shirakawa y col.[6] en 1977, el desarrollo de los polímeros conductores se ha acelerado a un ritmo inesperadamente rápido y se han descubierto una gran variedad de ICPs [7,8]. Entre los más destacados se encuentran el polipirrol (PPY), la polianilina (PANI), el poli(p-fenileno) (PPP), el poli(p-fenil vinileno) (PPV), politiofeno (PT) y sus derivados más conocidos el poli(3,4-etilendioxitiofeno) (PEDOT) y el poli(3-hexiltiofeno-2,5-diil) (P3HT) (**Figura 2**).

Los ICPs presentan una conductividad en el rango de los materiales semiconductores, aunque esta conductividad se puede ver aumentada por el efecto de agentes de transferencia de carga usados para generar, por oxidación o reducción, cargas positivas o negativas, lo que conoce como dopante [4]. El concepto de dopaje es el tema central y unificador que distingue los polímeros conductores de todos los demás tipos de polímeros [9]. El dopaje es un proceso reversible, cuyo proceso inverso se conoce como desdopaje. Estas reacciones se puede llevar a cabo química o electroquímicamente [2,8].

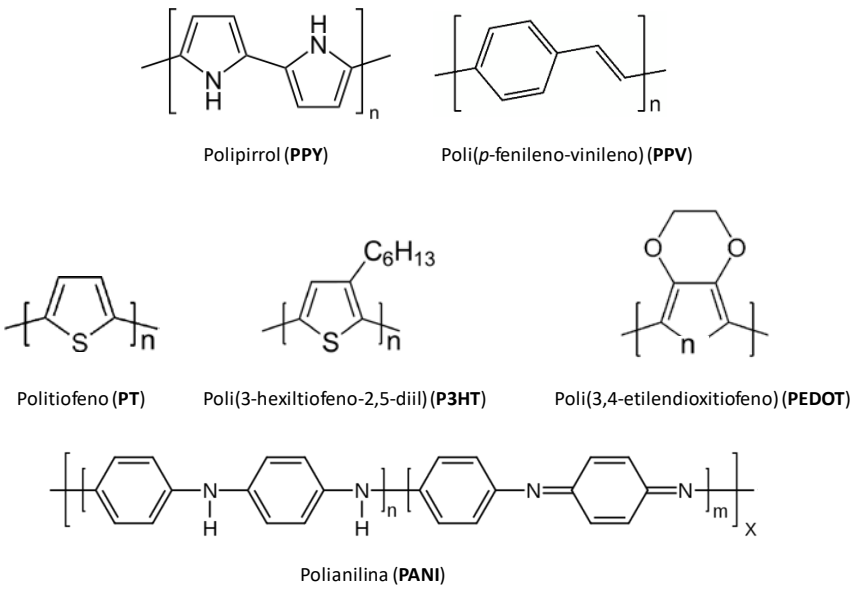

Figura 2. Estructura de polímeros intrínsecamente conductores típicos.

El uso de dopantes puede incrementar la conductividad eléctrica varios órdenes de magnitud, dependiendo del nivel de dopaje alcanzado (**Figura 3**). Ajustando adecuadamente el nivel de dopaje, se puede variar fácilmente la conductividad entre la forma no dopada (aislante o semiconductora) y la completamente dopada (altamente conductora) del polímero [2]. Sin embargo, en la mayoría de las aplicaciones se llega a conductividades del rango de los semiconductores, aunque el nivel de dopaje sea alto.

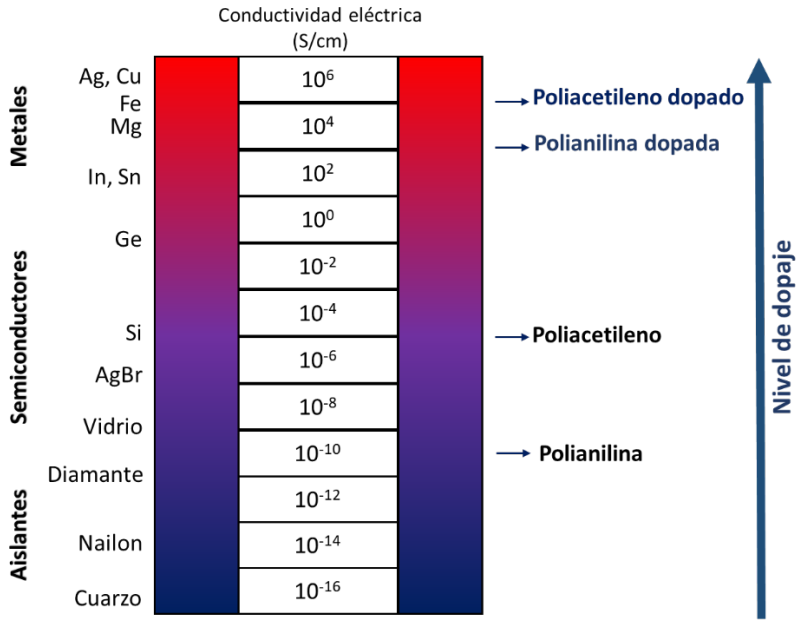

Figura 3. Efecto del dopaje en polímeros conductores [2].

Al dopar se introducen cargas en la cadena principal del polímero, lo cual modifica sus propiedades eléctricas. Estas cargas pueden ser electrones libres o cargas positivas

denominadas “huecos”. Según el tipo de portadores de carga, sean huecos o electrones, se hablará de semiconductores tipo p o n, respectivamente. Los procesos de dopaje y desdopaje de los ICPs se producen mediante reacciones rápidas y sencillas.

La conducción eléctrica en los ICPs se explica mediante la Teoría de Orbitales Moleculares (TOM). Para el caso de moléculas pequeñas con un número definido de átomos, los orbitales atómicos se combinan para dar orbitales moleculares con niveles energéticos discretos. Los orbitales de menor energía se llenan con electrones adquiriendo un carácter enlazante, sin embargo, los orbitales con energía más alta están vacíos, por consiguiente, adquieren un comportamiento antienlazante. Cuando el número de átomos aumenta formando una red tridimensional, los orbitales moleculares se solapan formando bandas, y entre la banda de orbitales moleculares enlazante y la banda de orbitales moleculares antienlazantes, aparece un salto energético (*band gap*) (**Figura 4**). A la banda inferior, ocupada por los electrones que participan en el enlace, se le llama banda de valencia y a la banda superior formada por los electrones libres, aquellos que se han desligado de sus átomos y pueden moverse libremente, banda de conducción.

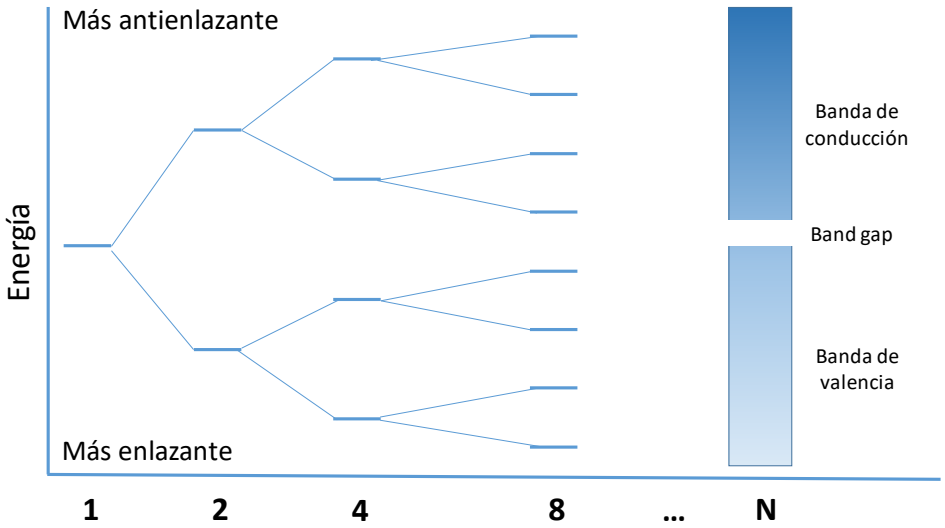

Figura 4. Diagrama energético de bandas de un semiconductor.

Por tanto, la estructura electrónica de polímeros conjugados se divide en dos partes: las bandas σ y las bandas π organizadas en niveles energéticos enlazante y antienlazante. Mientras que en el caso de polímeros saturados sólo existe la banda σ, y, la excitación de electrones se promoverá hacia la banda σ^* antienlazante, generando una

inestabilidad estructural. Sin embargo, en el caso de los polímeros conjugados la transición electrónica dentro de la banda π no produce la rotura de la cadena del polímero, por eso se comportan como conductores. Los polímeros conductores tal como son sintetizados son relativamente aislantes, debido a que tienen un salto energético relativamente amplio. Con el dopaje, la conductividad eléctrica aumenta debido a que se crean niveles energéticos disponibles entre el orbital más alto ocupado (HOMO) y el orbital más bajo desocupado (LUMO). Al aumentar el nivel de dopaje se aumenta el número de estados disponibles hasta la aparición de bandas. Estos estados disponibles se pueden describir, desde un punto de vista físico, como una distorsión geométrica intramolecular en el sistema π, caracterizada por un cambio en la alternancia de la longitud de los enlaces y se conocen como polaron o bipolaron (**Figura 5**).

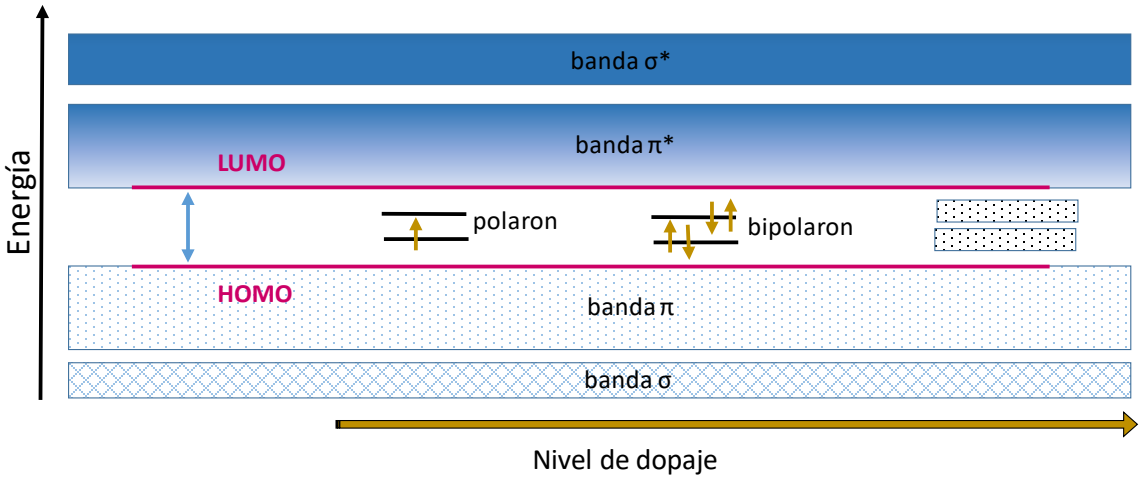

Figura 5. Diagrama energético de la formación del polaron, bipolaron y las bandas de bipolaron en función del nivel de dopaje.

Esta capacidad para conducir la corriente eléctrica de los ICPs, posibilita que algunos como el PEDOT, la PANI y el PPY, se utilicen en aplicaciones prácticas en áreas muy diversas como electrónica, electricidad, termoelectricidad, electroquímica, electromagnetismo, electromecánica, electroluminiscencia, electroreología, membranas y sensores entre otros [10–14].

En la siguiente sección se tratará en profundidad del ICP objeto de esta tesis, la polianilina.

Polianilina: síntesis, estructura y doping

Dentro del conjunto de los polímeros intrínsecamente conductores la polianilina presenta una serie de características que la diferencian de la mayoría de ICP, entre las que se encuentran:

- Su cadena principal no presenta una sucesión ininterrumpida de enlaces C–C π-conjugados, sino una alternancia de anillos aromáticos y átomos de nitrógeno entre ellos que dan lugar a unidades repetitivas del tipo bencenoide y quinoide.

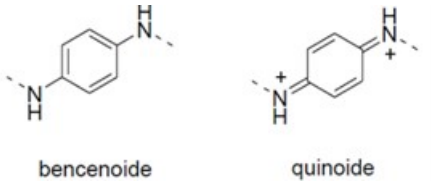

Figura 6. Unidades repetitivas dentro de la estructura de la PANI.

- Debido a la presencia de átomos de nitrógeno en la cadena principal presenta un tipo de dopado químico especial por protonación, esto es, la PANI es dopada con ácidos próticos y desdopada mediante bases.
- La PANI presenta tres estados de oxidación diferentes lo que permite variar su conductividad eléctrica en un rango de 10^{-7} a 3 x 10^{2} S/cm [15].
- El estado dopado de mayor conductividad eléctrica es altamente estable en condiciones ambientales normales (en presencia de aire, humedad, CO_2, etc.) al contrario de lo que sucede con los estados dopados de la mayoría de ICPs.
- La síntesis convencional de PANI es mucho más económica, debido al bajo precio del monómero de anilina, y sencilla que la del resto de ICPs.

Como contrapunto, la PANI presenta una solubilidad baja, comparada con otros de los polímeros más estudiados como el PEDOT. Aunque esta solubilidad puede verse mejorada por el uso de determinados dopantes como veremos más adelante. Además, aunque presente una temperatura de degradación alta, comparada con otros ICPs como el PPY, no es garantía de que la conductividad se mantenga estable a temperaturas elevadas.

En cuanto a su síntesis, en general, la PANI puede sintetizarse por polimerización electroquímica y por polimerización química oxidativa de la anilina, por diferentes rutas de síntesis como polimerización acuosa y polimerización por emulsión [16] .

En la polimerización electroquímica, la anilina es oxidada en el ánodo de una celda electroquímica gracias a la corriente eléctrica. Esta técnica tiene la ventaja de generar menos residuos y obtener una PANI más pura que la polimerización química, pero, por la contra, sólo se pueden obtener películas delgadas y el rendimiento general de la polimerización es bajo. Además, lo más habitual, es que las películas obtenidas se depositen directamente sobre una superficie conductora, hecho que hace que el polímero esté conectado eléctricamente a una superficie metálica, imposibilitando las mediciones eléctricas en el plano de la película, debido a la presencia del sustrato metálico.

En la polimerización química la anilina es oxidada mediante un compuesto oxidante en presencia de un ácido, que actúa como dopante (**Figura 7**).

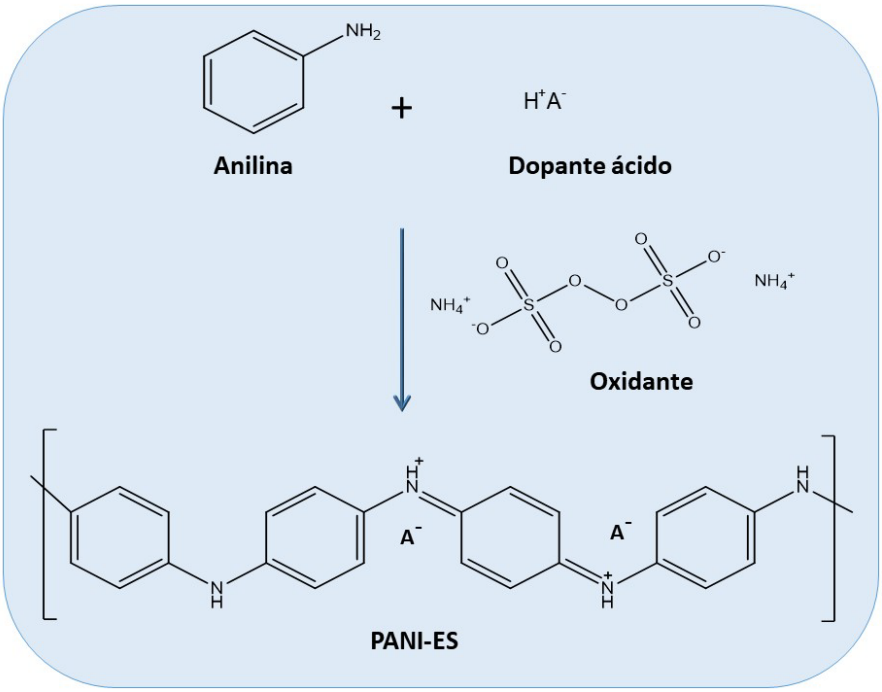

Figura 7. Polimerización química de la anilina.

Al inicio de la polimerización oxidativa, se forma la PANI base o emeraldina base (PANI-EB) que se comporta como aislante eléctrico, pero en el momento de adición del dopante, en este caso un ácido, se protonan las iminas formándose la especie conocida como emeraldina sal (PANI-ES). Esta estructura, a través de una reacción redox, adquiere la estructura de bipolaron que evoluciona a una forma más estable, el polaron (**Figura 8**), que, como ya se ha indicado anteriormente, está directamente relacionada con la capacidad de estos polímeros para conducir la electricidad. Desde un punto de

vista químico, en el polaron de la PANI, un catión radical de un nitrógeno actúa como hueco comportándose como un portador de carga. El electrón del nitrógeno adyacente (neutro) salta a ese hueco y ese hueco se convierte en neutro. Por tanto, cuando un electrón comienza a moverse en un sentido a través de la cadena polimérica hay un hueco moviéndose en dirección opuesta (**Figura 9**) permitiendo que exista conducción eléctrica.

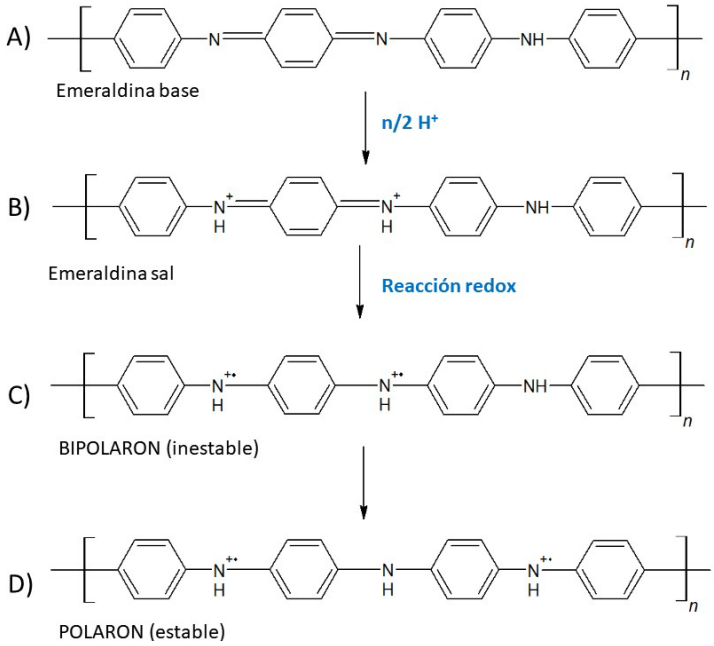

Figura 8. Diferentes formas de la PANI A) antes de la protonación, B) después de la protonación, y C) formación del bipolaron y D) polaron

Además, hay que tener en cuenta que la conductividad eléctrica en materiales orgánicos, se ve afectada de manera notoria por su orden estructural. La polianilina es semicristalina, un sistema heterogéneo con una región cristalina (ordenada) dispersa en una región amorfa (desordenada) como muestra la **Figura 10**.

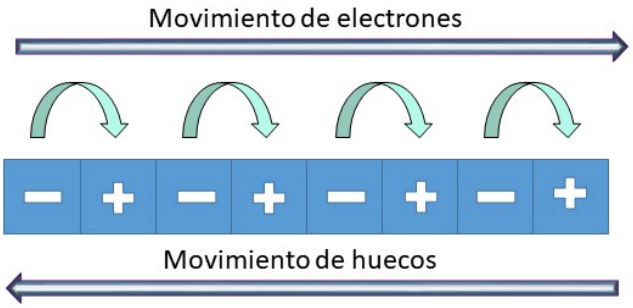

Figura 9. Camino de conducción de la PANI donde los signos positivos representan el radical catión N como un hueco y los signos negativos representan un N neutro [10].

La conducción en la región cristalina ocurre por *hopping* de portadores de carga a través del polaron (**Figura 8D**) permitiendo el movimiento de portadores a lo largo de la cadena, lo que se conoce como el transporte intracadena (**Figura 11**). Para conseguir un transporte entre las cadenas, es necesario acercar los contactos intermoleculares para permitir una transferencia de carga eficiente entre moléculas a través de las uniones de niveles electrónicos π. Esta transferencia se consigue gracias a la conformación coplanar de las cadenas, produciendo un "apilamiento π" (*π-π stacking*) [17](**Figura 11**) que permite transporte intercadena, que intensifica las fuerzas de Van der Wals. Dentro de los dominios cristalinos, el transporte de carga puede ser altamente anisotrópico debido a diferencias en el acoplamiento electrónico entre moléculas. Estas regiones están rodeadas de zonas amorfas, no conductoras, por lo que el conjunto de la conductividad depende de los puentes que conecten las regiones cristalinas y las zonas amorfas.

El dopante, que aparecerá como contraión de la cadena polimérica, será crucial en la morfología y en las propiedades macroscópicas del polímero final[18,19]. Dependiendo de la naturaleza química del ácido que actuará como dopante, se hablará de polimerización por emulsión (ácido orgánico) o polimerización acuosa (ácido inorgánico). La polimerización química acuosa, comparada con la anterior, es una de las técnicas más empleadas debido a que es más respetuosa con el medio ambiente (no usa disolventes halogenados), permite trabajar a temperatura ambiente y con tiempos de reacción más cortos.

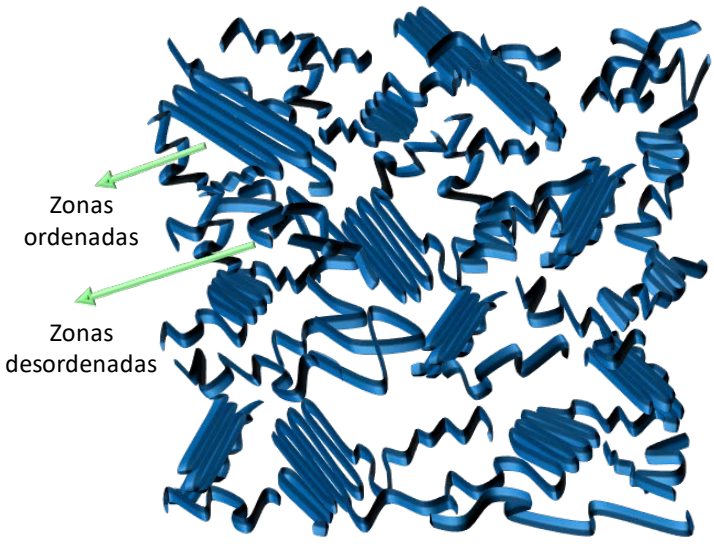

Figura 10. Estructura heterogénea de PANI [10,20].

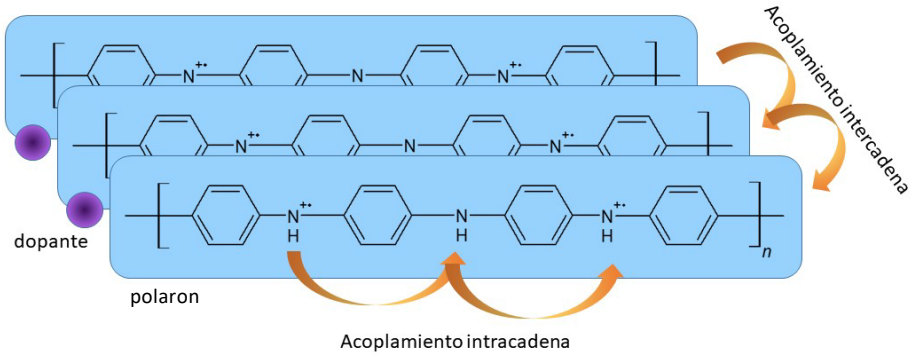

Figura 11. Mecanismos de transporte intra e intercadena.

Atendiendo a la naturaleza del dopante, se ha visto que el uso de dopantes inorgánicos, (HCl, H_3PO_4 [21], H_2SO_4 [21], HBF_4 [22] etc.) aumenta la conductividad eléctrica [21] del polímero, pero presenta una menor estabilidad térmica que los dopantes orgánicos (DBSA [23], NaSIPA [19,24], CSA [25], etc.). Esto es debido a que los dopantes inorgánicos suelen tener un tamaño menor y son más fáciles de eliminar a temperaturas más bajas (inferiores a 100°C), por el contrario, debido al tamaño más grande de los dopantes orgánicos, suelen ser estables hasta 250°C [19].

En cuanto a sus propiedades físicas, uno de los principales inconvenientes de la polianilina es su solubilidad, ya que, es prácticamente insoluble en la mayoría de los disolventes convencionales. Para mejorar su procesabilidad, cara a la elaboración de materiales compuestos, numerosos estudios se han centrado en sintetizar una PANI más soluble. Como ejemplo, Cao y col. [26] que han sintetizado PANI en presencia de ácido dodecilbencensulfónico (DBSA) ya que no solo actúa como dopante, sino que el ácido libre o en exceso también ejerce de plastificante [27], mejorando así su solubilidad y posterior procesabilidad.

En ocasiones resulta interesante combinar las propiedades de los ácidos inorgánicos y orgánicos, es decir, una buena conductividad eléctrica y mayor estabilidad térmica. Esto es posible a través de rutas de síntesis indirectas, conocidas como procesos de desdopaje/redopaje [19,24], en los que se dopa el polímero con un ácido inorgánico, se desdopa con hidróxido amónico y se vuelve a dopar con un ácido orgánico, obteniendo así un polímero con propiedades mejoradas respecto al polímero obtenido por síntesis directa.

Las propiedades de las PANIs hacen posible su uso en un amplio espectro de aplicaciones, algunas de las cuales se citan a continuación a modo de ejemplo (**Tabla 1**).

Tabla 1. Aplicaciones de la polianilina y sus propiedades.

Propiedades	**Aplicaciones relacionadas**
Conductor eléctrico intrínseco	Adhesivos conductores [28], tintas [29] y pinturas [30] Materiales plásticos [31] y tejidos [32]antiestáticos Circuitos electrónicos por *inkjet printing* [33,34]
Cambia la viscosidad reversiblemente bajo un campo eléctrico	Material electroreológico [35–37]
Cambia de conductividad eléctrica y color según sea expuestos a ácidos, bases o sustancias neutras	Sensores químicos [38] (NH_3, CO_2, NO_2,CO,Cl_2, O_3, H_2…)
Cambia de morfología por procesos de protonación-desprotonación y oxidación-reducción	Membranas para separación de gases y solutos neutros [39,40] Actuadores de cambio de pH [41]
Presenta altos valores de capacitancia	Capacitadores [42] y dispositivos de almacenamiento de memoria [43]
Habilidad para absorber y reflejar la radiación electromagnética	Dispositivos de apantallamiento de interferencias electromagnéticas [44]
Pueden cambiar de estado altamente conductor a aislante	Dispositivos de memoria digital [45,46]
Respuesta electromecánica	Músculos artificiales [47]
Habilidad para acumular y transformar energía	Electrodos en baterías recargables [48,49] Ventanas electrocrómicas e inteligentes [50]
Cambia de dador a aceptor electrónico según su estado de oxidación Emite color bajo excitación	Uniones p-n Celdas solares Diodos emisores de luz orgánicos (OLEDs) [51,52]

Sin embargo, todavía no se ha explorado todo su potencial como polímero conductor de bajo coste, de ahí el interés que suscita la investigación en la optimización de sus propiedades eléctricas y su aplicación en nuevos dispositivos.

2. Compuestos poliméricos conductores

Para abaratar el coste y mejorar la procesabilidad de los ICPs surgen los compuestos poliméricos conductores (CPCs), que constan de una matriz polimérica no conductora y un material que actúa como carga [4]. Debido a su fácil procesado, bajo coste y su versatilidad pueden usarse en distintas aplicaciones dependiendo de su conductividad eléctrica (**Figura 12**).

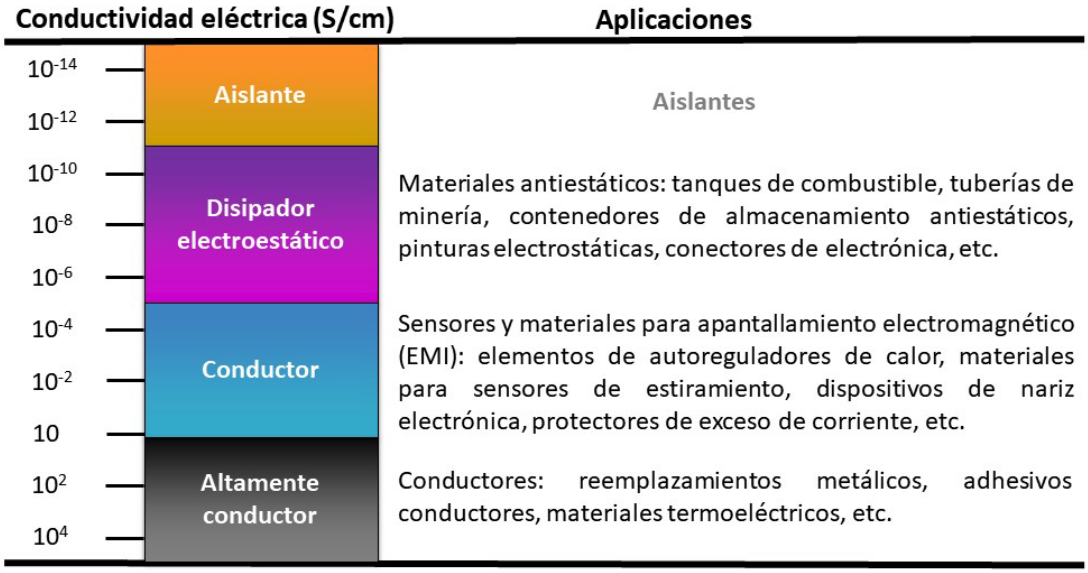

Figura 12. CPCs según su conductividad eléctrica y aplicaciones [3].

Las cargas conductoras pueden clasificarse en función de su tamaño (micro o nano), según su dimensión, 3D (partículas o esferas), 2D (láminas), 1D (fibras o whiskers) y según la naturaleza química (metálica u orgánica).

Respecto a la naturaleza de las cargas conductoras, las nanopartículas metálicas y los nanotubos de carbono son los más comúnmente empleados para fabricar una gran variedad de nanocompuestos de altas prestaciones [53–55].

Las nanopartículas metálicas (Au, Ag, Pd, Cu, Ni,[56] etc.) aportan excepcionales propiedades como conductividad eléctrica y térmica a los polímeros aislantes [57,58]. Pero estas nanopartículas no se dispersan con facilidad en matrices poliméricas [59] y son tóxicas [60].

En cuanto a las cargas de origen orgánico, los nanotubos y nanofibras de carbono son las más utilizadas ya que presentan una baja densidad y una extremadamente alta relación de aspecto. Sin embargo, tienden a agregarse dentro de la matriz polimérica,

tienen elevado coste y escasa interacción interfacial con los polímeros [61] así como una elevada toxicidad asociada a su tamaño nanométrico y forma fibrilar. En este sentido, se ha realizado la polimerización in situ donde se obtiene el compuesto al mismo tiempo que polimeriza la anilina. Este tipo de polimerización se ha llevado a cabo en presencia de CNTs [62], oxido de grafeno [63,64], nanocelulosa [65], platino [66], óxidos de hierro [67], SiO_2 [68]y mercurio[69] entre otros.

También se ha estudiado el uso de PANI como cargas orgánicas en matrices poliméricas [70] con el objetivo de mejorar la procesabilidad y las propiedades mecánicas de la PANI pura. Se han obtenido compuestos poliméricos conductores fundamentalmente a través de dos métodos[23]:

- Mezclado en fundido: El polímero que sirve de matriz, se funde o se reblandece antes de su mezclado con las cargas conductoras. En este proceso se usan polímeros termoplásticos como los copolímeros de etileno y vinil acetato (EVA)[23], polietileno (PE)[71], polivinil alcohol (PVA)[72,73], polimetacrilato de butilo (PBMA)[74] , polimetacrilato de metilo y policloruro de vinilo (PMMA y PVC)[75], policarbonato (PC)[76], etc. Así mismo, también se han utilizado polímeros elastoméricos en la preparación de compuestos de PANI como cauchos de nitrilo-butadieno (NRB)[77] o cauchos de etileno propileno dieno (EPDM)[78,79].
- Mezclado en disolución/dispersión: este método engloba la disolución/dispersión de la polianilina y una matriz polimérica ya sea en el mismo disolvente o diferente, agitación de la mezcla y eliminación del disolvente por secado [80,81].

El mezclado en fundido es el método más usado para la producción de los compuestos a gran escala, ya que permite utilizar los métodos de transformación habituales en la industria de polímeros. Sin embargo, el mezclado en disolución permite obtener una dispersión más homogénea, pero presenta la dificultad de que se necesita un disolvente común.

2.1. Conducción eléctrica y percolación

La conductividad eléctrica de los CPCs se basa en una red continua conductora que se va formando al añadir cargas conductoras, como ICPs, a la matriz polimérica aislante. Cuando se alcanza un valor crítico de partículas conductoras, el CPC exhibe una

transición de aislante a conductor, produciéndose un aumento drástico en la conductividad, de varios órdenes de magnitud, cuando se empiezan a formar los primeros caminos conductores [3]. Este valor crítico de carga conductora se define como concentración umbral de percolación o threshold (ρ_c). Al aumentar el contenido de carga conductora, se van formando caminos adicionales en el seno de la matriz polimérica, aumentando gradualmente así la conductividad hasta llegar a un valor máximo y constante.

La conductividad de un CPC puede describirse empíricamente a través de la ley de la potencia:

$$\sigma = \sigma_0(\rho - \rho_c)^t \quad \textbf{(1)}$$

Donde σ representa la conductividad eléctrica, σ_0 la conductividad de las partículas conductoras y t es el exponente crítico relacionado con la dimensionalidad de la red. Según este modelo, t≈2 y t≈1.3 se asignan a redes conductoras de 3D y 2D, respectivamente. Sin embargo, se ha comprobado que los valores experimentales pueden desviarse ligeramente de los valores predichos.

Redes segregadas

Una forma de disminuir la concentración umbral de percolación es mediante el control morfológico del material, formando lo que se conoce como redes segregadas de compuestos poliméricos conductores (s-CPCs) [82]. En este tipo de estructuras, las partículas conductoras se distribuyen en un volumen restringido de la matriz en lugar de disponerse aleatoriamente a través de todo el compuesto (**Figura 13**). Esto provoca un aumento sustancial de la densidad efectiva de los caminos conductores, para una concentración determinada de partículas conductoras. Esta estructura facilita la formación de una red conductora donde existe un mayor contacto entre las partículas conductoras, con la mínima cantidad de relleno y consecuentemente, se reduce de forma importante el valor de la concentración umbral de percolación con respeto a los compuestos conductores tradicionales[3].

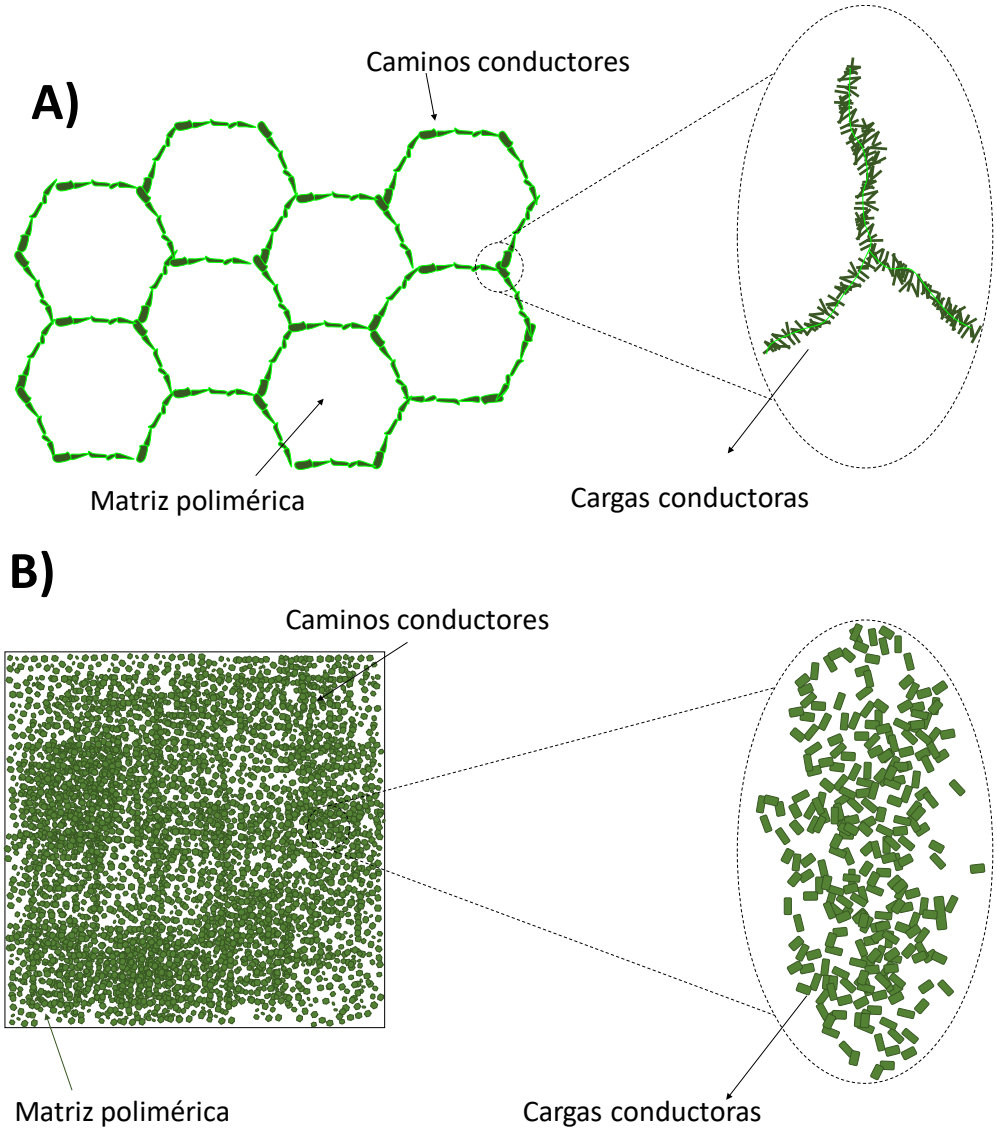

Figura 13. Esquema de distribución de (a) red segregada y (b) aleatoria en un CPC.

Existen tres métodos para la formación de redes segregadas de partículas conductoras en una matriz aislante: compresión directa, mezclado en fundido y mediante la tecnología látex. Siendo este último método el que se va a utilizar en la presente tesis.

Tecnología látex

Se conoce como látex a cualquier emulsión de micropartículas poliméricas en medio acuoso. Cuando se dispersan partículas conductoras en látex y una vez evaporado el disolvente, las partículas conductoras quedan retenidas dentro del espacio intersticial entre las partículas de látex, formando lo que se conoce como red segregada [3,83–85]. Este tipo de microestructura mejora las propiedades de transporte de carga a una concentración de relleno baja.

Esta tecnología permite obtener s-CPCs a temperatura ambiente o ligeramente superior, es asequible, desde el punto de vista económico, y respetuoso con el medioambiente, ya que se lleva a cabo en disolución acuosa evitando así disolventes tóxicos o inflamables [3,86,87].

Las matrices que se usan habitualmente para este método son elastómeros termoplásticos como polivinilalcohol (PVA), polivinil acetato (PVAc), poliestireno (PS), o termoestables como caucho natural (NR), caucho de poliestireno-butadieno (SBR) entre otros.

Utilizando este método, Miriyala y col. [88] prepararon s-CPC con partículas de látex de (PVAc) y negro de carbono (CB) demostrando que el uso de partículas de látex redujo el umbral de percolación eléctrica de 8,17% a 1,21% en volumen mediante la formación de redes segregadas conductoras. En otros estudios se utilizó una técnica similar para preparar CPCs con varios tipos de rellenos, tales como CNTs [89] y grafeno [90]. Dalton y col. [91] pusieron de manifiesto que se podía obtener una reducción significativa en el umbral de percolación eléctrica mediante el bloqueo de CNT en una retícula de cristales coloidales, predominantemente hexagonal compacta (HCP), de partículas de látex. Los autores demostraron que la exclusión de los CNT del volumen interior de las partículas de látex promovió la formación de una red segregada no aleatoria.

Aunque la mayoría de los trabajos en s-CPCs se centran en CNTs como cargas, también se ha utilizado la tecnología látex usando polímeros intrínsecamente conductores. En este sentido, se puede preparar materiales compuestos a través de la polimerización de la anilina, en presencia de una matriz polimérica de látex [92–96] o a través de mezcla física [97,98] de PANI en una dispersión de matriz polimérica de látex. Gospodinova y col. [97] han obtenido mezclas conductoras poliméricas a través de mezcla física de PANI con PVA y EVA. Haba y col. [98] comprobaron que la mezcla física de una dispersión acuosa de anilina-DBSA con un polímero acuoso, por ejemplo, PMMA y PS, permite obtener films conductores (10^{-2} a 10^{-3} S / cm) con contenidos muy bajos de PANI-DBSA (1-2% en masa). El umbral de percolación de tales mezclas es extremadamente bajo (~0.5% en peso de PANI-DBSA). Estas mezclas exhiben niveles de conductividad similares con el mismo contenido de PANI, lo que indica un mecanismo común en la formación de la estructura conductora, independientemente de la matriz polimérica. Esto es debido a la

gran estabilidad de la dispersión acuosa de PANI-DBSA, ya que la presencia de moléculas DBSA en exceso forman un fuerte enlace de hidrógeno con las partículas PANI-DBSA, creando aglomerados. Al mezclar la dispersión acuosa PANI-DBSA con una emulsión acuosa de otro polímero, los aglomerados PANI se desintegran para formar una dispersión visualmente homogénea[99].

En esta línea, se han hecho algunos estudios de mezclas de PANI utilizando PVAc como matriz [100–104]. En estos compuestos, los grupos carbonilo del PVAc forman un enlace de hidrógeno con los grupos amino de la PANI, lo que permite mejorar la solubilidad original de la PANI. De este modo, Kanhegaokar y col [101]. realizaron una comparativa de mezclas de PANI con PVAc, a través de polimerización in situ y mezcla física, obteniendo un valor de percolación del 7% y 20% en masa de PANI, respectivamente. La conductividad de los compuestos se encuentra entre 10^{-2}-10^{-1} S/cm, con valores más altos para la polimerización in situ. Recientemente, Levin y col. [105] han obtenido una red segregada de PANI en una matriz de PVAc latex, con un valor de threshold extremadamente bajo de 0,6 % en masa de PANI y una conductividad máxima para los compuestos estudiados de 2,8 S/cm para 5% en masa de PANI.

A la vista de estos antecedentes, la obtención de compuestos conductores mediante tecnología látex, es una vía de trabajo de gran interés para el desarrollo de materiales flexibles, con buenas propiedades eléctricas y mediante un proceso de fabricación sostenible y económico.

3. Polímeros conductores en termoelectricidad

Hoy en día, debido al calentamiento global asociado a los combustibles fósiles y al constante crecimiento del coste de la energía, se hace necesaria la búsqueda de nuevas fuentes de energía más limpias y sostenibles [106–110]. Como es bien sabido, los sistemas actuales de producción de energía eléctrica son poco eficientes y desperdician entre el 40 y 60% del calor consumido. Ese calor residual, en muchos casos, no se puede reutilizar para producir más energía eléctrica por los métodos tradicionales (por ejemplo, a través de una turbina), puesto que se encuentra acumulado en fluidos a temperaturas bajas, poco rentables para este proceso. Por estas razones, existe una gran demanda de nuevas tecnologías enfocadas a la recuperación del calor ambiental y su conversión en energía eléctrica.

Dentro de este contexto, la termoelectricidad suscita gran interés, por su aplicación en dispositivos que generan energía eléctrica (generadores termoeléctricos) o que produzcan una diferencia de temperaturas (enfriadores de Peltier). Aunque es un fenómeno físico, que fue descubierto en el siglo XIX por Thomas Johann Seebeck y Jean Charles Athanase Peltier, no fue hasta hace pocas décadas cuando la investigación en dispositivos termoeléctricos ha resurgido con fuerza. La termoelectricidad se presenta como una de las posibles soluciones a la crisis energética actual y a nuestra dependencia de los combustibles fósiles, ya que permite aprovechar el calor residual emitido por diversas fuentes como chimeneas, tubos de escape, e incluso calor humano y convertirlo en energía eléctrica [110–116], a través de generadores termoeléctricos (TEG). Este tipo de tecnología es una solución económica, limpia, que no genera residuos tóxicos y respetuosa con el medio ambiente. Además, estos dispositivos presentan gran versatilidad, en cuanto a su diseño, y larga vida útil [117,118]. Hoy en día, se comercializan enfriadores de Peltier, para aplicaciones de aire acondicionado, con un cuarto de la eficiencia alcanzada en sistemas convencionales. También ya se están utilizando generadores TE en vehículos, que aprovechan el calor del tubo de escape, y aumentan la autonomía del vehículo hasta en un 10% [119]. Sin embargo, aunque ya se comercializan muchos dispositivos termoeléctricos (TE), basados sobretodo en materiales semiconductores inorgánicos, a temperaturas de trabajo alrededor de la temperatura ambiente, el número de aplicaciones es limitado debido a su baja eficiencia, estando lejos de competir con las formas convencionales de generación energía y/o refrigeración[120].

La historia de los materiales termoeléctricos **(Figura 14)** está directamente asociada a su eficiencia termoeléctrica medida como la figura de mérito ZT [121], **Ec. (2)**, que depende de conductividad eléctrica (σ) y térmica (k), coeficiente de Seebeck (α)y de la temperatura de uso (T).

$$ZT = \frac{\alpha^2 \sigma}{k} T \qquad \textbf{(2)}$$

Desde el hallazgo de la termoelectricidad, se usaron semiconductores inorgánicos basados principalmente en aleaciones de teluro, bismuto y antimonio llegando a alcanzar un valor máximo de ZT∼1. Durante muchos años este valor de ZT permaneció

estancado, pero fue a principios de los 90, cuando los trabajos de L.D. Hicks y M. S. Dresselhaus [122] centrados en la mecánica cuántica, sirvieron para abrir un nuevo camino en el diseño de materiales termoeléctricos. La aportación fundamental de la nanotecnología fue la de disminuir la conductividad térmica, típicamente alta de los materiales inorgánicos, alcanzando así una eficiencia termoeléctrica mucho mayor que la conseguida anteriormente. Este hito cambió la naturaleza de la investigación termoeléctrica: en lugar de seleccionar materiales semiconductores disponibles en la naturaleza, se comenzó a diseñar nuevos materiales termoeléctricos de síntesis o modificados.

Unos años más tarde, se descubrieron las skutteruditas [123],estructuras de tierras raras y metales de transición con P, Sb y As, principalmente utilizadas para aplicaciones de altas temperaturas[124] (más de 600°C). A principios de los 2000, las superredes de $BiTe/Sb_2Te_3$[125] y *quantum dots* de PbSeTe/PbTe [126] constituyeron notables mejoras alcanzando valores de ZT∼2-2.5.

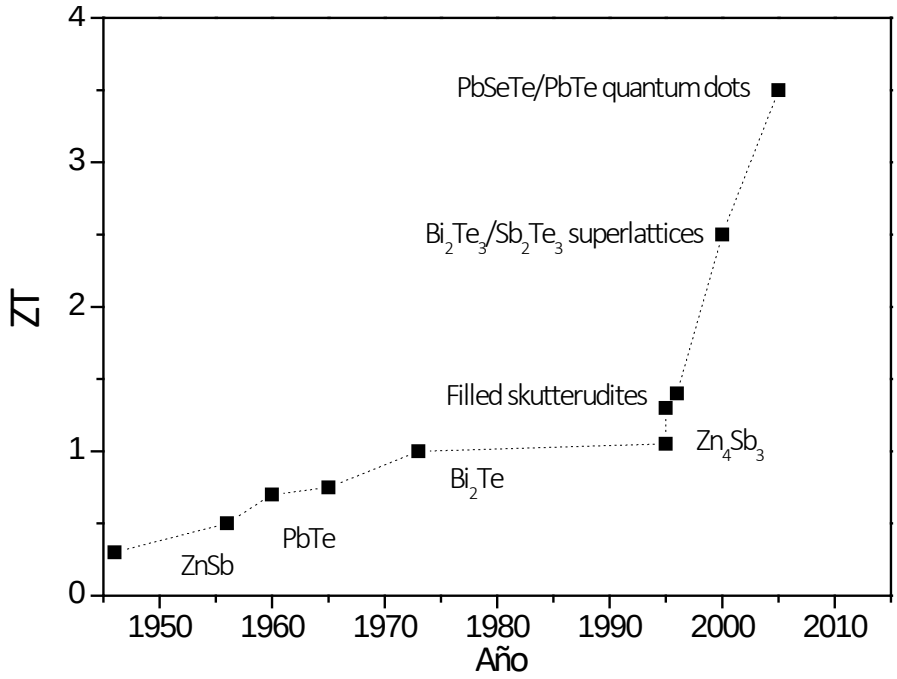

Figura 14. ZT de los TE inorgánicos típicos en función de los años [110,127].

La eficiencia de los materiales TE, depende de la temperatura de trabajo. La mayoría de los materiales anteriormente descritos, alcanzan su eficiencia máxima a temperaturas superiores a 400°C [128]. Actualmente, los materiales termoeléctricos que funcionan a bajas temperaturas o ambiente suelen ser de Bi_2Te_3 y sus aleaciones [17,125,129]. Estos

elementos son poco abundantes en la naturaleza, por lo que se incrementa su coste, además, durante su proceso de extracción existe riesgo de toxicidad y contaminación medioambiental.

Actualmente, existen materiales TE inorgánicos con una buena relación coste/eficiencia para su uso en generadores termoeléctricos que aprovechan el calor residual en un rango de temperaturas medio-alta. Sin embargo, no son rentables cuando las variaciones de temperatura son menores de 135°C [130]. En este tipo de aplicaciones, los materiales termoeléctricos orgánicos pueden ser una buena alternativa. Sintetizados a partir de moléculas abundantes en la naturaleza, sus propiedades TE son fácilmente modificables durante la síntesis y además, permiten mayor versatilidad en cuanto al diseño de los dispositivos debido a flexibilidad. Los dispositivos fabricados con materiales orgánicos, aunque son menos eficientes en determinadas aplicaciones que los inorgánicos, se han convertido, recientemente, en un tema de gran interés para la comunidad científica. Asimismo, presentan una síntesis fácilmente escalable para la producción en masa a un coste relativamente bajo y a baja temperatura.

En el campo de los termoeléctricos orgánicos (OTEs), los polímeros conductores han ganado terreno en dispositivos electrónicos y generadores termoeléctricos [131,132]. Entre ellos se encuentran como principales candidatos el PEDOT[133,134,143–152,135,153–162,136,163–165,137–142] y la PANI[166,167,176–185,168,186,169–175], aunque también hay algunos trabajos con PPY[187–189]. Los estudios realizados desde principios de los 2000, arrojan una gran diversidad de valores de ZT (**Figura 15**), que abarca un rango de varios órdenes de magnitud para estos polímeros conductores, y más aún, si se le añaden polímeros compuestos conductores con partículas de carbono (grafeno o nanotubos) o partículas inorgánicas (Ag, derivados de Bi_2Te_3, etc.). El PEDOT, dentro de los OTEs, es uno de los más estudiados en la bibliografía científica, y con los valores de eficiencia termoeléctrica más altos (ZT∼1)[135]. La PANI aunque ha sido menos estudiada, en combinaciones con partículas de carbono, también ha logrado valores cercanos a la unidad [168] (ZT∼0.74).

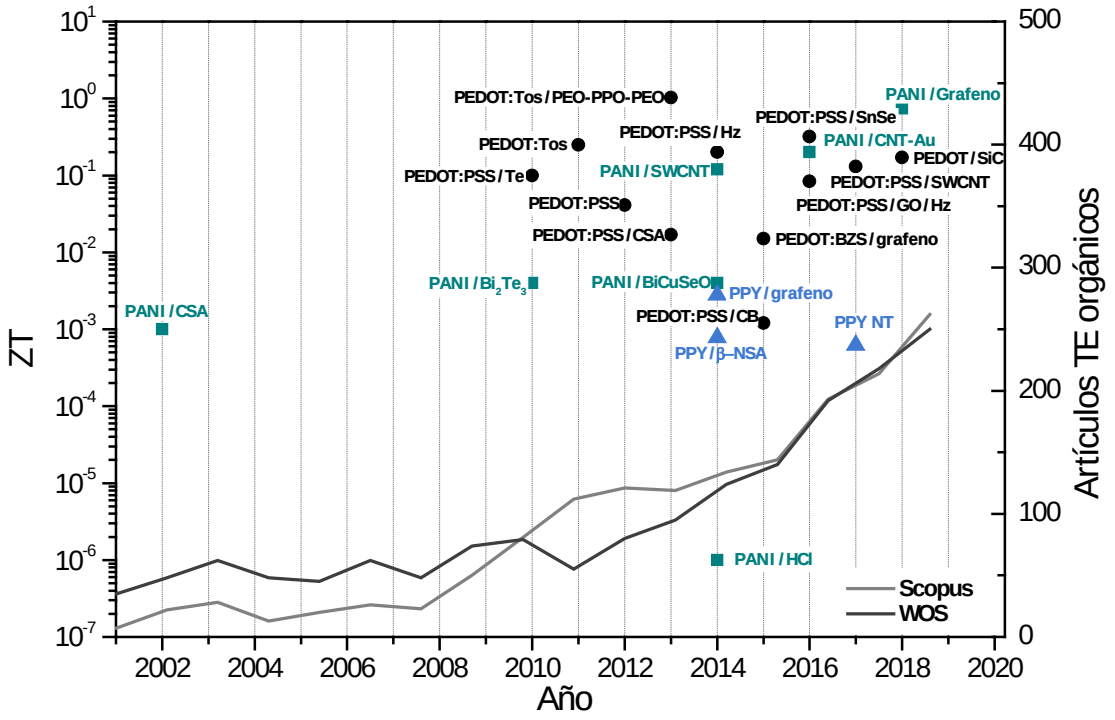

Figura 15. ZT de materiales TE orgánicos: poli(3,4–etilendioxi–tiofeno) (PEDOT) [133,134,163,165,135,136,144,145,151–153,159], polianilina (PANI) [166,168,172,174,176,183,184] y polipirrol (PPY) [187–189] (izquierda). Número de artículos publicados en TE orgánicos en los últimos 20 años según las bases de datos de Scopus y Web of Science (derecha).

3.1. El conflicto de las propiedades termoeléctricas

Mejorar la figura de mérito, ZT o eficiencia termoeléctrica, implica, conseguir una alta conductividad eléctrica, elevado coeficiente Seebeck y una baja conductividad térmica, según la Ecuación (2). Alcanzar este equilibrio es complicado porque estos parámetros de transporte están interrelacionados (en la mayoría de las ocasiones, favorecer uno de los parámetros hace que disminuya otro de ellos) y dependen de la naturaleza físico-química del material. Las principales estrategias para aumentar el ZT en materiales inorgánicos y orgánicos son diametralmente opuestas. En los materiales inorgánicos los trabajos se han centrado en una disminución de la conductividad térmica, mientras que, para los materiales orgánicos debido su baja conductividad térmica inherente a su naturaleza polimérica, las principales investigaciones se han centrado en maximizar el producto de la conductividad eléctrica (σ) y el coeficiente de Seebeck al cuadrado (α^2), conocido como factor de potencia (PF).

Profundizando un poco en los parámetros de los que depende el factor de mérito, se sabe que la conductividad eléctrica (σ) aumenta proporcionalmente con la

concentración de portadores (n) según la **Ec. (3)**, donde μ es la movilidad y q la carga de los portadores:

$$\sigma = nq\mu \quad \textbf{(3)}$$

Además, en muchos OTE el aumento de la conductividad eléctrica viene acompañado por un aumento en la conductividad térmica del material. Esto es debido que la conductividad térmica presenta dos contribuciones, **Ec. (4)**, que vienen dadas por: el transporte de portadores (κ_e) y por el movimiento fonónico a través de la red (κ_L). El término de la contribución electrónica (κ_e), inherentemente baja para materiales orgánicos en comparación con los inorgánicos, se relaciona directamente con la conductividad eléctrica a través de la ley de Wiedemann-Franz, (**Ec. (7)**)donde L es el factor de Lorenz (2,4 x 10^{-8} J^2 K^{-2} C^{-2}).

$$\kappa = \kappa_e + \kappa_L \quad \textbf{(4)}$$

$$\kappa_e = LT\sigma \quad \textbf{(5)}$$

Por otro lado, el coeficiente de Seebeck está directamente relacionado con la entropía por unidad de portador (electrones o huecos) [190]. En los materiales semiconductores con una baja concentración de portadores, el coeficiente de Seebeck (α) viene dado por la expresión de Mott [191,192]:

$$\alpha = \frac{8\pi^2 k_B^2}{3eh^2} m^* T \left(\frac{\pi}{3n}\right)^{2/3} \quad \textbf{(6)}$$

Donde k_B es la constante de Boltzmann, e es la carga de portador, h es la constante de Planck, n es la concentración de portadores y m^* es la masa efectiva del portador. Por lo que el coeficiente de Seebeck es inversamente proporcional a dicha concentración y disminuye si aumenta el número de portadores (al revés que la conductividad eléctrica).

La masa efectiva (m^*) de los portadores de carga es otro parámetro clave ya que una masa efectiva grande produce un coeficiente de Seebeck alto, pero una baja conductividad eléctrica. Los portadores pesados se moverán a velocidades más bajas, y por tanto tendrán una movilidad menor, lo que resulta en una baja conductividad eléctrica, (Ecuación (3)). La relación entre la masa efectiva y la movilidad es compleja, y depende de la estructura electrónica, mecanismos de dispersión y la anisotropía del material.

Desde un punto de vista cuántico, la conductividad eléctrica y el Seebeck están relacionados con la estructura de bandas, más específicamente, con la densidad de estados (DOS). Los portadores que participan directamente en el transporte son los cercanos por arriba o por abajo del nivel de Fermi (nivel ocupado más alto energéticamente a la temperatura de cero absoluto). Los materiales inorgánicos tienen una estructura de bandas bien definidas, entre la banda de valencia y la banda de conducción, pero en los materiales orgánicos, debido a los defectos estructurales y a su heterogeneidad, los estados electrónicos no se encuentran bien definidos, por lo que es necesario controlar la forma de la DOS, estrechándola para aumentar el número de cargas móviles cercanas al nivel de Fermi, para conseguir un aumento del coeficiente de Seebeck [193].

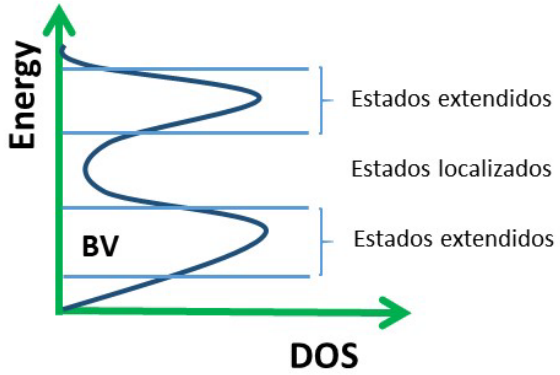

Figura 16. Densidad de estados en un polímero conductor[194] incluyendo los estados extendidos y localizados.

Comentada esta controversia, para mejorar el factor de potencia de los materiales termoeléctricos orgánicos, durante los últimos años se han utilizado una gran variedad de estrategias como cambiar la movilidad de portadores, ajustar del nivel de doping o introducir materiales orgánicos o inorgánicos para formar compuestos.

➢ Nivel de dopaje

Como ya se ha comentado en la sección de *Polímeros conductores*, la naturaleza del dopante y las condiciones de síntesis son determinantes para la morfología y propiedades termoeléctricas del polímero final resultante.

Una de las primeras estrategias que se ha utilizado para aumentar el factor de potencia de los OTEs, es aumentar la conductividad eléctrica aumentando el nivel de dopaje. Han sido publicados estudios, donde se confirma que el nivel de dopaje se controla con la

relación molar de ácido dopante utilizado en la síntesis química o con el nivel de oxidación en síntesis electroquímica [173,195,196]. En esta línea, se ha estudiado la dependencia entre la conductividad eléctrica y el coeficiente de Seebeck de la PANI con la concentración de dopante (HCl [173], CSA [185], etc.). Además, para PANI [173] y PEDOT [134] se ha comprobado que la conductividad eléctrica aumenta al aumentar el nivel de dopaje hasta cierto valor, sin embargo, como era de esperar, el coeficiente de Seebeck muestra la tendencia contraria. Por tanto, es necesario llegar a una situación de compromiso y encontrar el nivel de dopaje óptimo, donde se maximice el factor de potencia y por tanto ZT (**Figura 17**).

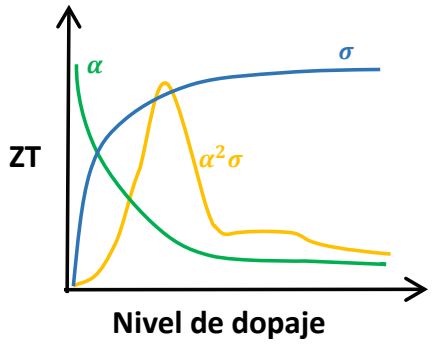

Figura 17. Optimización de ZT según el nivel dopaje [134,197].

➢ Compuestos poliméricos conductores

Otra estrategia para la obtención de OTEs con mejor eficiencia termoeléctrica, es la introducción de cargas en polímeros intrínsecamente conductores (IPC). Existen básicamente dos tipos de cargas: nanocargas de carbono como nanotubos o grafeno o partículas de semiconductores inorgánicos como Bi_2Te_3, entre otros.

El uso de nanotubos de carbono (CNT) permite crear una red nanoestructurada eléctricamente conectada y térmicamente desconectada, aumentando así la conductividad eléctrica y el coeficiente de Seebeck y manteniendo una baja conductividad térmica [198]. Choongo y col. [199] han estudiado la influencia de CNTs en la eficiencia termoeléctrica de distintas matrices poliméricas de PEDOT alcanzando un ZT=0,02. Para la PANI, también se ha demostrado que el uso de CNT mejora el coeficiente de Seebeck en comparación a la PANI pura [200]. Esta mejora del Seebeck es debida a que los CNTs crean una barrera energética que hace que sólo pasen los portadores de mayor energía, lo que provoca una mejoría en la movilidad de portadores. En este caso, los CNTs se usan como una plantilla que permite un mayor ordenamiento

de la polianilina a través de interacciones π-π [198,200]. Cuando la PANI recubre la superficie de los CNTs, aumenta la movilidad y concentración de los portadores. Esto provoca un aumento simultáneo de la conductividad eléctrica de y del coeficiente de Seebeck, por lo que el PF del compuesto es mayor [201,202].

A partir del 2013, muchos investigadores se han centrado en aumentar las propiedades termoeléctricas de los ICPs utilizando grafeno y sus derivados. La ventaja que tiene el grafeno es que, uniformemente distribuido aumenta el área interfacial de dos a tres veces con respecto a los CNTs. Esto resulta en una transferencia de portadores más fácil con una alta movilidad electrónica en el grafeno. Kim y col. [203] han medido films de PEDOT con un bajo porcentaje de grafeno y han obtenido un ZT=2,1·10^{-2}. También se ha experimentado con grafeno funcionalizado con fullereno [204], observando, de igual manera, un aumento simultáneo del coeficiente de Seebeck y conductividad eléctrica. La mejora del Seebeck debido a la inserción de fullereno es explicada de dos formas: un posible desplazamiento del nivel de Fermi por encima de la banda de valencia y a que las nanopartículas de fullereno se ensamblan a la superficie del grafeno debido a un efecto de filtro que permite el paso selectivo de los portadores de alta energía. Esto provoca un aumento significativo de la energía de los portadores, permitiendo una mejora del coeficiente de Seebeck. Además, el fullereno debido a su estructura puede causar confinamiento cuántico durante el transporte de portadores, lo que hace que aumente el coeficiente de Seebeck [204].

En 2017, autores como Wang y col. [205] estudiaron los polímeros compuestos por PPY/grafeno/PANI. Este compuesto tiene mejor conductividad eléctrica y el mejor Seebeck resultando un PF muy superior (1600 y 1400 veces más alto que PANI y PPY puros, respectivamente). Los trabajos más relevantes, que datan del 2017 y 2018, en compuestos PANI/grafeno han tenido como resultado un ZT=0,02 con grafeno 3D [169] y un ZT=0,74 para grafeno modificado con grupos diamino [168].

La introducción de partículas de semiconductores inorgánicos en una matriz polimérica, mejora las propiedades termoeléctricas debido a sus relativamente más altos valores de Seebeck en comparación con los TE orgánicos [15]. Zhan y col. [206] demostraron que el factor de potencia aumentaba sustancialmente para una matriz de PEDOT, después de adición de partículas de Bi_2Te_3. De igual forma, también se ha comprobado que

partículas de telurio (Te) dispersas en una matriz de PEDOT, no sólo mejoran la conductividad eléctrica, sino que también restringen la conductividad térmica manteniendo el bajo valor polimérico. Como resultado se han llegado a alcanzar valores de ZT ∼0,1 a temperatura ambiente [163].

➢ Factores estructurales

En general, la morfología de los materiales es una manifestación de su organización molecular, lo que ofrece otro camino para optimizar las propiedades termoeléctricas de los polímeros conjugados [207].Como ya se ha explicado en la sección de *Polímeros conductores*, los materiales orgánicos son mayoritariamente desordenados o amorfos, y en ocasiones presentan cierto grado de orden o cristalinidad (semicristalinos). El transporte en estos termoeléctricos es heterogéneo, con zonas de mayor conductividad separadas por regiones de menor conductividad. Por este motivo, hay que prestar atención tanto al transporte a lo largo de la cadena polimérica, como al acoplamiento entre las cadenas. En la Ecuación (3) se muestra la dependencia directa entre la conductividad eléctrica y la movilidad, que está fuertemente influenciada por la morfología del material.

Otro factor estructural importante es el peso molecular: los polímeros que tienen un bajo peso molecular tienen longitudes de cadena más cortas y son de naturaleza más cristalina, que los polímeros de alto peso molecular. Sin embargo, la movilidad de portadores es menor, debido a que las conexiones entre los cristales están separadas por zonas aislantes. Por contra, los polímeros de alto peso molecular presentan cadenas más largas, que aunque tienden a enredarse pueden conectar las regiones ordenadas (o cristalinas) de manera más efectiva [208].

Reducir el tamaño y la dimensionalidad de los materiales termoeléctricos ha demostrado aumentar la figura de mérito, en la nanoescala y materiales nanoestructurados, debido a los efectos de tamaño cuántico. En este contexto, el control de la morfología para obtener polímeros nanoestructurados, ha demostrado ser una estrategia exitosa para mejorar las propiedades termoeléctricas. Desde Hicks y Dresselhaus [122], la nanoestructuración de materiales inorgánicos ha conseguido mejorar sus propiedades termoeléctricas, principalmente debido a una disminución de la conductividad térmica de red (κ_L), que se puede conseguir introduciendo defectos en la

red. Para materiales orgánicos, también se ha demostrado que polímeros sintetizados con tamaños de partícula en la nanoescala y con alta relación de aspecto, presentan mayor conductividad que los sintetizadas en tamaño micrométrico [209]. El uso de nanoestructuras permite el bloqueo selectivo de fonones, permitiendo mejorar el transporte de portadores [210]. Este aumento es debido tanto a la baja conductividad térmica, como al aumento de la densidad interfacial, así como de los posibles efectos de tamaño cuántico que mejoran el coeficiente de Seebeck como resultado de un aumento de la densidad de estados (DOS) cercanos al nivel de Fermi [211].

En cuanto a dimensionalidad se refiere, trabajos como el publicado por Naoki Toshima [172] para PANI-CSA, han demostrado la superioridad en eficiencia termoeléctrica de los materiales en película delgada (2D) frente a los materiales en bulk (3D).

Una de las principales estrategias de mejora del ZT, desacoplando la tendencia típica de σ y α, es producir un cambio en la movilidad de portadores a través de cambios conformacionales de la cadena polimérica. Estos cambios conformacionales mejoran el acoplamiento entre cadenas y se pueden conseguir mediante la introducción de grupos laterales basados en cadenas alquílicas. El procedimiento más habitual consiste en la formación de una dispersión a través de partículas micelares, ya sea con un contraión polimérico soluble, p.e. poli-estireno sulfonado (PSS)[212] o utilizando un agente tensioactivo iónico que actúa como contraión, p.e. ácido canforsulfónico (CSA)[213]. También se ha visto que la presencia de disolventes con un elevado punto de ebullición favorece una mejor organización de la cadena polimérica aumentando así la movilidad de portadores y por tanto, su conductividad eléctrica en varios órdenes de magnitud [194,214]. Este efecto en la morfología (**Figura 18**) se denomina dopaje secundario, para distinguirlo del primario, que sólo está relacionado con el nivel de oxidación [215]. Este cambio conformacional ayuda a reducir las zonas aislantes, mejora la orientación de los granos de conductores, etc. [207].

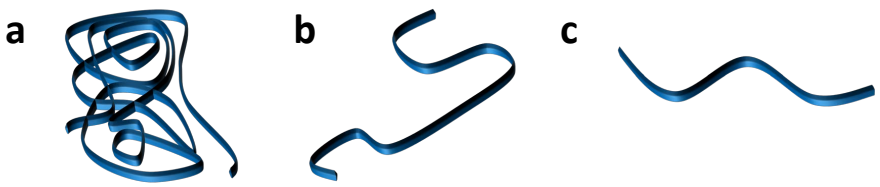

Figura 18. Efecto del dopaje secundario en la conformación del material antes de la adición del dopante (a) y después (b y c)

En esta línea, se han publicado varios artículos [216–218]que sugieren que el efecto del tratamiento con solventes en PEDOT, aumenta la conductividad eléctrica sin disminuir el coeficiente Seebeck. Se examinaron solventes como agua, etilenglicol (EG), dimetilsulfóxido (DMSO), dimetilformamida (DMF) y N-metil-2-pirrolidona (NMP). Se ha comprobado que para el PEDOT, el tratamiento con líquidos iónicos [219] produce modificaciones morfológicas que hacen aumentar el coeficiente de Seebeck y la conductividad eléctrica de manera simultánea.

También se han estudiado los efectos que produce la introducción de determinadas estructuras químicas sobre las propiedades termoeléctricas, p.e. la inclusión de un pequeño porcentaje de moléculas *open-shell* hace que los portadores de baja velocidad sean captados, y que en el transporte solo intervengan los portadores de alta movilidad, provocando un aumento del coeficiente de Seebeck [220,221].

Recientemente, Zhao y col. [222] han publicado un estudio sobre el impacto en las propiedades termoeléctricas, de diferentes post-tratamientos para el PEDOT nanoestructurado, mediante reducción ácida, consiguiendo un ordenamiento de las cadenas.

A parte de los procedimientos químicos para mejorar el orden estructural, la orientación de las cadenas poliméricas también se puede inducir con técnicas como el estiramiento mecánico [223] o el *spin coating*[224]*,* que mejoran la uniformidad y homogeneidad del polímero, dando lugar a una conductividad eléctrica más alta que la conseguida por métodos tradicionales de mezclado y film-casting [17].

Estudios más teóricos en relación a la estructura de bandas, han demostrado que un desplazamiento hacia arriba del nivel HOMO produce un aumento simultáneo del Seebeck y la conductividad eléctrica [225].

En resumen, las arriba expuestas son algunas estrategias seguidas para la mejora de las propiedades termoeléctricas y que pueden servir de directrices para trabajos futuros. Sin embargo, es evidente que se requiere una investigación mucho más extensa para optimizar el valor de ZT de los materiales termoeléctricos orgánicos. Además de tener un número suficiente de portadores con alta movilidad, conseguida a través de la

nanoestructura o cambios conformacionales, es necesario que el material tenga una distribución localizada de portadores para poder mejorar su figura de mérito [226].

3.2. Generador termoeléctrico: funcionamiento, eficiencia y diseño

Un generador termoeléctrico (TEG), también llamado generador Seebeck, es un dispositivo que convierte el flujo de calor (diferencia de temperatura) directamente en energía eléctrica a través del llamado efecto Seebeck (efecto termoeléctrico). El efecto Seebeck convierte calor directamente en electricidad a través de uniones p-n. Al aplicar un gradiente de temperaturas (generando una zona fría y una zona caliente), los electrones o huecos de la zona caliente se moverán más rápido y difundirán hacia la zona fría acumulándose en ella. Como consecuencia, la acumulación de carga de la zona fría se produce un potencial eléctrico [191] (**Figura 19A**).

El voltaje Seebeck es proporcional a la diferencia de temperaturas según la ecuación:

$$\Delta V = S \cdot \Delta T \qquad \textbf{(7)}$$

siendo S la constante denominada coeficiente de Seebeck o termopotencia. El signo del coeficiente de Seebeck determina, por regla general, el tipo de portadores de carga del semiconductor, valores negativos indican que los portadores son electrones, tratándose de un semiconductor tipo n, mientras que valores positivos muestran que los portadores son huecos y, por tanto, un semiconductor tipo p. La **Figura 19B** muestra un ejemplo de unión p-n.

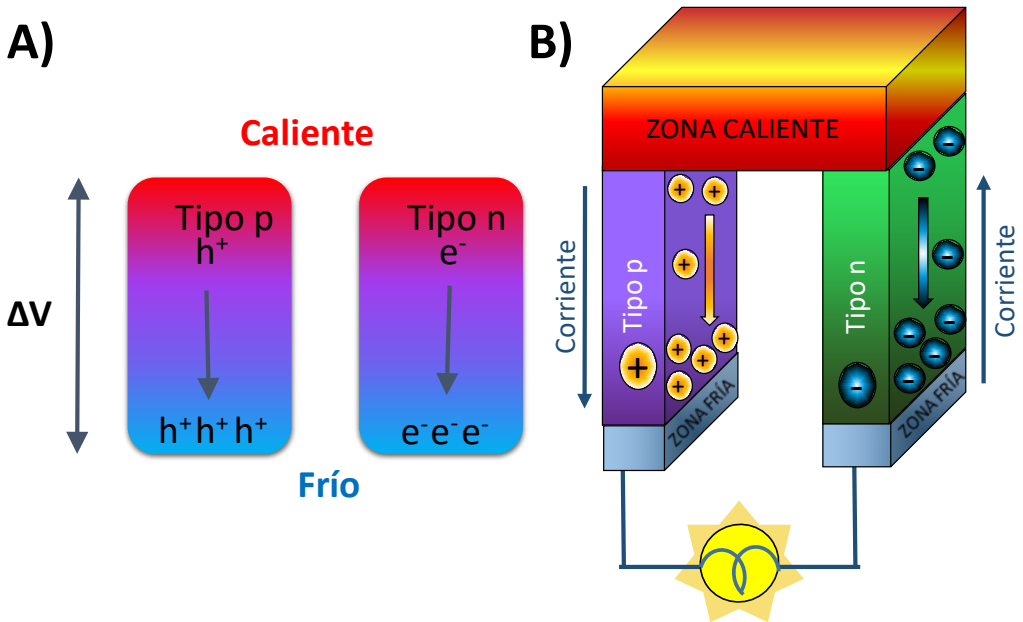

Figura 19. A) Efecto termoeléctrico y B) unión p-n.

La **Figura 20** muestra un ejemplo de TEG con un diseño estándar actualmente comercial, compuesta por un sustrato cerámico en los extremos y una lámina conductora de cobre entre las uniones p-n. En este diseño, las pérdidas de calor se reducen mediante la disposición de uniones p-n alternadas eléctricamente en serie (y térmicamente en paralelo), lo que permite maximizar la generación de energía[17]. A demás, el conjunto de uniones conectadas en paralelo es una estrategia para asegurar que el dispositivo continúa trabajando incluso si una de ellas falla [227]. Tener muchas uniones en serie permite la obtención de mayores voltajes, lo cual es útil para mejorar el rendimiento del dispositivo [17].

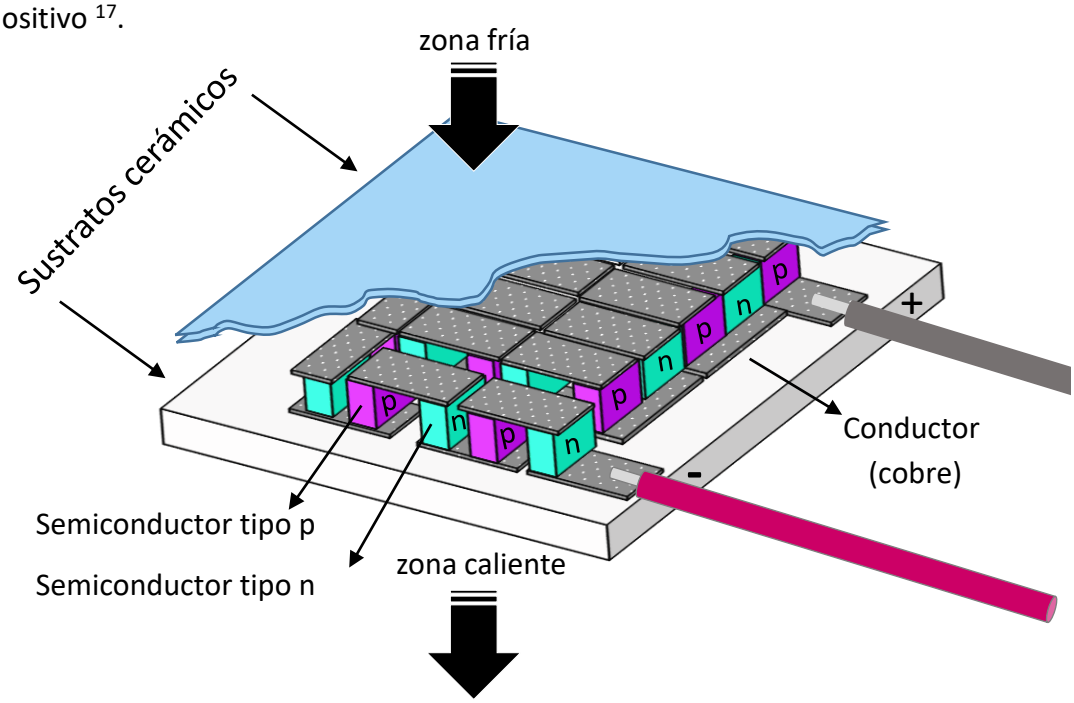

Figura 20. Generador termoeléctrico inorgánico.

El rendimiento de un TEG depende de: la eficiencia termoeléctrica del material, la eficiencia termodinámica del dispositivo y el diseño del dispositivo. Como ya ha sido mencionado anteriormente, la eficiencia del material viene dada por la figura de mérito ZT según la **Ec. (2)**. A su vez, la eficiencia termodinámica (ϕ_{max}) tiene en cuenta la eficiencia de Carnot y ZT, según la ecuación[190]:

$$\phi_{max} = \phi_C \frac{\sqrt{1 + ZT_{AV}} - 1}{\sqrt{1 + ZT_{AV}} + T_C/T_H} \qquad \textbf{(8)}$$

donde T_{AV} es la temperatura promedio entre los focos caliente (T_H) y frío (T_C), ϕ_C es la eficiencia de Carnot dada por $\phi_C = \frac{T_H - T_C}{T_H}$ y ZT_{AV} es la figura de mérito del material a la

temperatura promedio.

En cuanto al diseño del módulo TE, la flexibilidad y la ligereza inherente de los OTEs ofrece ventajas en aplicaciones a baja temperatura, que no son posibles con los materiales inorgánicos típicamente rígidos como, por ejemplo, dispositivos integrados en tejidos inteligentes (**Figura 21**). En este sentido, un campo en el que las aplicaciones de los generadores TE fabricados con materiales orgánicos tienen una alta demanda es en el desarrollo de dispositivos que trabajan sin necesidad de baterías, aprovechando la electricidad generada por una diferencia de temperaturas baja (*self-powered sensors*). En este tipo de dispositivos, que trabajan a temperaturas cercanas a la temperatura ambiente y consumen poca potencia eléctrica es donde se prevé haya mayor desarrollo tecnológico en los próximos años y donde los materiales TE orgánicos presentan una ventaja competitiva, respecto a los materiales inorgánicos. Los dispositivos portátiles que se pueden llevar puesto como un reloj [228], o incluidos en ropa interior o en una camiseta [229] presentan un gran atractivo, por ejemplo, para la transformación del calor humando en energía sin necesidad de baterías [230–232].

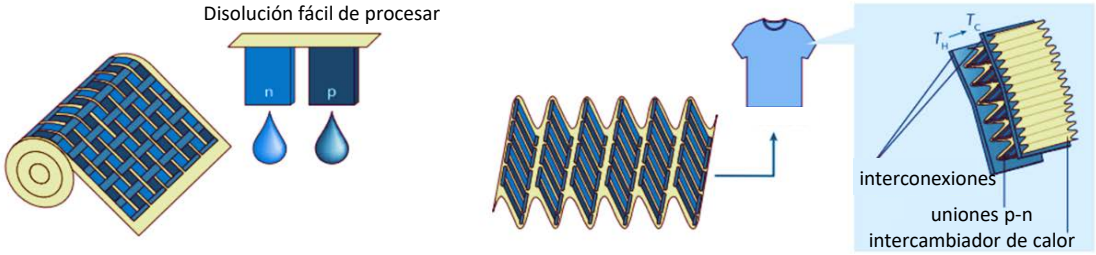

Figura 21. Materiales termoeléctricos orgánicos (OTE) compatibles con procesado 2D fácilmente personalizable en distintas conformaciones [17].

La transformación eficiente del calor en energía eléctrica no depende únicamente del material sino también, de la geometría de las uniones y de la distancia entre ellas dentro del dispositivo. Por ejemplo, aumentar la longitud de la unión o disminuir el espacio entre las uniones permite obtener gradientes de temperatura superiores, pero tiene el inconveniente de que aumenta las pérdidas por efecto Joule. Además de la geometría de las uniones, el factor de relleno (espacio que ocupan los elementos en el interior del módulo termoeléctrico) también debe ser considerado para una óptima transformación. Un factor de relleno bajo reduce el número total de uniones p-n del módulo, y permite tener un gradiente más homogéneo entre las placas, pero limita la generación de energía [17]. Es por tanto necesario conseguir un compromiso para optimizar el diseño del

material para disminuir las pérdidas de calor por conducción (efecto Joule) y aumentar el voltaje eléctrico generado.

Dicho esto, el objetivo es obtener un generador TE con máxima eficiencia y eso depende, como ya se ha dicho, no sólo de ZT sino también de la eficiencia termodinámica del módulo y de su diseño. Utilizando materiales TE orgánicos de bajo coste, más versátiles, aunque los valores de ZT sean menores, se podría obtener buen rendimiento conectando un mayor número de uniones p-n con un diseño adecuado para maximizar el voltaje generado.

4. Polímeros conductores en sensores

En general, los polímeros intrínsecamente conductores (ICP) son buenos candidatos para el desarrollo de sensores químicos o electroquímicos por dos razones [233]:

- El movimiento de los electrones, relacionado con el estado de oxidación - reducción (nivel de dopaje) de un polímero conductor, puede verse modificado por la interacción con diversos analitos originando cambios en las características del material como resistencia eléctrica o potencial electroquímico [234]. Teniendo en cuenta la capacidad del ICP para actuar como un transductor electrónico, la magnitud de la señal eléctrica generada se puede correlacionar con la intensidad de la interacción físico-química. Por ejemplo, cuando un compuesto conductor se expone a un vapor, penetra en el polímero y hace que se expanda. Esta expansión reduce la cantidad de caminos conductores para los portadores de carga y como resultado, aumenta la resistencia eléctrica del compuesto.
- Mantienen las propiedades de procesado de los polímeros, lo que reduce los costes de fabricación de películas delgadas, polvos o fibras.

En este contexto, dentro de los ICPs, la polianilina se ha utilizado frecuentemente como sensor químico [235,236], en la **Tabla 2** se muestran algunos ejemplos. Además de la utilización de los polímeros conductores como sensores químicos, la capacidad para desconectar los caminos conductores bajo la acción de estímulos externos, como cambios de temperatura o deformación mecánica, hace que los polímeros conductores puedan utilizarse también como sensores de temperatura y piezoresistivos [3,237–241]. Para

este tipo de sensores, presentan un gran potencial las redes segregadas de compuestos poliméricos conductores (S-CPCs) debido a su baja concentración umbral[242–244].

Tabla 2. Principales materiales usados como sensores químicos basados en PANI [38,245,246].

Material sensitivo	Analitos detectados	Ref.
PANI	H_2O_2	247
PANI SWCNT	NH_3, NO_2,H_2S	248
PANI/Au/Al_2O_3	Acetona	249
PANI/TiO_2	NH_3	250
PANI/SnO_2	Humedad	251
PANI/$ZnMoO_4$	Gas licuado del petróleo	252
Pd/PANI	Metanol	253
Ag/PANI	Etanol	254
Cu/PANI	Cloroformo	255
PANI/FeAl	CO	256

Una de las propiedades que determina si un material puede ser utilizado como sensor electromecánico es la piezoresistividad, capacidad con la que un conductor o semiconductor varía su resistencia eléctrica cuando es sometido a un esfuerzo mecánico. La eficiencia de un material piezoresistivo se mide a través de su *Gauge Factor* (GF) o factor de deformación:

$$GF = \frac{\Delta R/R_0}{\Delta l/l_0} = \frac{d\rho/\rho_0}{\varepsilon} + 1 + 2\nu \qquad \textbf{(9)}$$

donde R es la resistencia eléctrica del material, ΔR es el cambio de resistencia causado por un cambio de longitud (Δl), ρ es la resistividad y ν es el coeficiente de Poisson. El término $\frac{d\rho/\rho_0}{\varepsilon}$ define el efecto intrínseco de piezoresistividad. El factor geométrico (1+2 ν) depende de las propiedades del material. El valor máximo para elastómeros es *GF* ≈ 2 donde el coeficiente de Poisson es de 0,5 [257].

Los elastómeros son los mejores candidatos como matriz de CPC para su utilización en sensores piezoresistivos, debido a su gran capacidad de deformación. De esta forma, se han diseñado compuestos con elastómeros termoplásticos [258–262] como matriz, y cargas

conductoras como nanopartículas de carbono (CNP) [263,264] o nanotubos multipared (MWNT) [265,266] para aplicaciones como sensores de deformación. Los sensores de CNP presentan una buena sensibilidad a deformaciones altas, pero requieren 10 veces más cantidad de relleno que utilizando MWNT.

Dicho esto, la polianilina entre otros ICPs, también se ha utilizado como cargas conductoras para sensores de deformación [74,105,267–271]. En esta línea, Levin y col. [105] han diseñado un sensor de deformación basado en una red segregada de PANI en una matriz de PVAc látex consiguiendo un GF entre 6 y 8 para concentraciones superiores al 5% en masa de PANI. Del Castillo-Castro y col. [74] utilizando como matriz polibutilmetacrilato, consiguieron variar el GF entre 0,8 y 31,2 dependiendo del contenido en PANI. Recientemente, Teixeira y col. [267] también analizaron el comportamiento piezoresistivo de un material compuesto por PANI con estireno-butadieno-estireno (SBS) obteniendo un GF≈1 con una variación lineal de la resistencia con la deformación aplicada.

A la vista de estos resultados, parece claro la potencialidad de la PANI en el desarrollo de nuevos sensores.

Referencias

1. Horie, K. *et al. Pure and Applied Chemistry* 76**,** (2004), 889.

2. MacDiarmid, a. G. *Angewandte Chemie International Edition* 40**,** (2001), 2581.

3. Pang, H., Xu, L., Yan, D. X. & Li, Z. M. *Progress in Polymer Science* 39**,** (2014), 1908.

4. Hess, M. *et al. Pure and Applied Chemistry* 78**,** (2006), 2067.

5. Heeger, A. J. *Angewandte Chemie International Edition* 40**,** (2001), 2591.

6. Shirakawa, H. *Angewandte Chemie (International ed. in English)* 40**,** (2001), 2574.

7. Skotheim, T. A. *Handbook of conducting polymers*. (1997), (CRC press, 1997).

8. KANATZIDIS, M. G. *Chemical & Engineering News* 68**,** (1990), 36.

9. Chiang, J.-C. & MacDiarmid, A. G. *Synthetic Metals* 13**,** (1986), 193.

10. Bhadra, S., Khastgir, D., Singha, N. K. & Lee, J. H. *Progress in Polymer Science (Oxford)* 34**,** (2009), 783.

11. Schoch, K. F. *IEEE Electrical Insulation Magazine* 10**,** (1994), 29.

12. Joo, J., Long, S. M., Pouget, J. P., Oh, E. J., MacDiarmid, A. G. & Epstein, A. J. *Physical Review B* 57**,** (1998), 9567.

13. Long, Y.-Z., Li, M.-M., Gu, C., Wan, M., Duvail, J.-L., Liu, Z. & Fan, Z. *Progress in Polymer Science* 36**,** (2011), 1415.

14. Hui, Y., Bian, C., Xia, S., Tong, J. & Wang, J. *Analytica Chimica Acta* 1022**,** (2018), 1.

15. Bharti, M., Singh, A., Samanta, S. & Aswal, D. K. *Progress in Materials Science* 93**,** (2018), 270.

16. Palaniappan, S. & John, A. *Progress in Polymer Science (Oxford)* 33**,** (2008), 732.

17. Russ, B., Glaudell, A., Urban, J. J., Chabinyc, M. L. & Segalman, R. A. *Nature Reviews Materials* 1**,** (2016), 16050.

18. Cao, Y., Andreatta, A., Heeger, A. J. & Smith, P. *Polymer* 30**,** (1989), 2305.

19. Horta-Romarís, L., Abad, M.-J., González-Rodríguez, M. V., Lasagabáster, A., Costa, P. & Lanceros-Méndez, S. *Materials & Design* 114**,** (2017), 288.

20. Beau, B., Travers, J. P. & Banka, E. *Synthetic Metals* 101**,** (1999), 772.

21. Abdiryim, T., Xiao-Gang, Z. & Jamal, R. *Materials Chemistry and Physics* 90**,** (2005), 367.

22. Zhang, Z., Wei, Z. & Wan, M. *Macromolecules* 35**,** (2002), 5937.

23. Dopico-García, M. S., Ares, A., Lasagabáster-Latorre, A., García, X., Arboleda, L. & Abad, M. J. *Synthetic Metals* 189**,** (2014), 193.

24. Saini, P., Jalan, R. & Dhawan, S. K. *Journal of Applied Polymer Science* 108**,** (2008), 1437.

25. Long, Y., Chen, Z., Wang, N., Li, J. & Wan, M. *Physica B: Condensed Matter* 344**,** (2004), 82.

26. Österholm, J.-E., Cao, Y., Klavetter, F. & Smith, P. *Polymer* 35**,** (1994), 2902.

27. Araújo, O. A. & De Paoli, M.-A. *Synthetic Metals* 159**,** (2009), 1968.

28. Hino, T., Namiki, T. & Kuramoto, N. *Synthetic Metals* 156**,** (2006), 1327.

29. Shim, G. H., Han, M. G., Sharp-Norton, J. C., Creager, S. E. & Foulger, S. H. *Journal of Materials Chemistry* 18**,** (2008), 594.

30. Hosoda, M., Hino, T. & Kuramoto, N. *Polymer International* 56**,** (2007), 1448.

31. Juvin, P., Hasik, M., Fraysse, J., Planès, J., Pron, A. & Kulszewicz-Bajer, I. *Journal of Applied Polymer Science* 74**,** (1999), 471.

32. Oh, K. W., Hong, K. H. & Kim, S. H. *Journal of Applied Polymer Science* 74**,** (1999), 2094.

33. Chen, B., Cui, T., Liu, Y. & Varahramyan, K. *Solid-State Electronics* 47**,** (2003), 841.

34. Matveeva, E. S., Diaz Calleja, R. & Parkhutik, V. *Journal of Non-Crystalline Solids* 235**–**237**,** (1998), 772.

35. Yin, J. & Zhao, X. in *Fundamentals of Conjugated Polymer Blends, Copolymers and Composites* (2015), 731. (John Wiley & Sons, Inc., 2015).

36. Dong, Y., Han, W. & Choi, H. *Polymers* 10**,** (2018), 299.

37. Quadrat, O. & Stejskal, J. *Journal of Industrial and Engineering Chemistry* 12**,** (2006), 352.

38. Fratoddi, I., Venditti, I., Cametti, C. & Russo, M. V. *Sensors and Actuators B: Chemical* 220**,** (2015), 534.

39. Tishchenko, G. A., Dybal, J., Stejskal, J., Kůdela, V., Bleha, M., Rosova, E. Y. & Elyashevich, G. K. *Journal of Membrane Science* 196**,** (2002), 279.

40. Pile, D. L. & Hillier, A. C. *Journal of Membrane Science* 208**,** (2002), 119.

41. Smela, E., Lu, W. & Mattes, B. R. *Synthetic Metals* 151**,** (2005), 25.

42. Lu, J., Moon, K.-S., Kim, B.-K. & Wong, C. P. *Polymer* 48**,** (2007), 1510.

43. Sung, J.-H., Kim, S.-J. & Lee, K.-H. *Journal of Power Sources* 126**,** (2004), 258.

44. Joseph, N., Varghese, J. & Sebastian, M. T. *RSC Advances* 5**,** (2015), 20459.

45. Wang, L., Sun, S., He, Y., He, N., Zhang, F., Yao, Y., Zhang, B., Zhuang, X. & Chen, Y. *European Polymer Journal* 98**,** (2018), 125.

46. Tseng, R. J., Huang, J., Ouyang, J., Kaner, R. B. & Yang, Y. doi:10.1021/nl050587l

47. Kaneto, K., Kaneko, M., Min, Y. & MacDiarmid, A. G. *Synthetic Metals* 71**,** (1995), 2211.

48. Jiménez, P., Levillain, E., Alévêque, O., Guyomard, D., Lestriez, B. & Gaubicher, J. *Angewandte Chemie* 129**,** (2017), 1575.

49. Simotwo, S. K. & Kalra, V. *Current Opinion in Chemical Engineering* 13**,** (2016), 150.

50. Jelle, B. P. & Hagen, G. *Solar Energy Materials and Solar Cells* 58**,** (1999), 277.

51. Mohsennia, M., Bidgoli, M. M., Boroumand, F. A. & Nia, A. M. *Materials Science and Engineering: B* 197**,** (2015), 25.

52. Chen, S.-A., Chuang, K.-R., Chao, C.-I. & Lee, H.-T. *Synthetic Metals* 82**,** (1996), 207.

53. Sun, X., Sun, H., Li, H. & Peng, H. *Advanced Materials* 25**,** (2013), 5153.

54. Shim, B. S., Zhu, J., Jan, E., Critchley, K., Ho, S., Podsiadlo, P., Sun, K. & Kotov, N. A. *ACS Nano* 3**,** (2009), 1711.

55. Oh, Y., Chun, K.-Y., Lee, E., Kim, Y.-J. & Baik, S. *Journal of Materials Chemistry* 20**,** (2010), 3579.

56. Ćirić-Marjanović, G. *Synthetic Metals* 170**,** (2013), 31.

57. Gunawidjaja, R., Jiang, C., Peleshanko, S., Ornatska, M., Singamaneni, S. & Tsukruk, V. V. *Advanced Functional Materials* 16**,** (2006), 2024.

58. Jiang, H., Moon, K., Li, Y. & Wong, C. P. *Chemistry of Materials* 18**,** (2006), 2969.

59. Kharlampieva, E., Zimnitsky, D., Gupta, M., Bergman, K. N., Kaplan, D. L., Naik, R. R. & Tsukruk, V. V. *Chemistry of Materials* 21**,** (2009), 2696.

60. Raveendran, P., Fu, J. & Wallen, S. L. *J. AM. CHEM. SOC* 125**,** (2003), 13940.

61. Pandey, G. & Thostenson, E. T. *Polymer Reviews* 52**,** (2012), 355.

62. Kumar, a M., Gasem, Z. M., Madhan Kumar, A. & Gasem, Z. M. *Progress in Organic Coatings* 78**,** (2015), 387.

63. Li, X., Zhong, Q., Zhang, X., Li, T. & Huang, J. *Thin Solid Films* 584**,** (2015), 348.

64. Baniasadi, H., Ramazani S.A, A., Mashayekhan, S. & Ghaderinezhad, F. *Synthetic Metals* 196**,** (2014), 199.

65. Luong, N. D., Korhonen, J. T., Soininen, A. J., Ruokolainen, J., Johansson, L.-S. & Seppälä, J. *European Polymer Journal* 49**,** (2013), 335.

66. Kinyanjui, J. M., Wijeratne, N. R., Hanks, J. & Hatchett, D. W. *Electrochimica Acta* 51**,** (2006), 2825.

67. Aphesteguy, J. C. & Jacobo, S. E. *Physica B: Condensed Matter* 354**,** (2004), 224.

68. Li, X., Wang, G. & Li, X. *Surface and Coatings Technology* 197**,** (2005), 56.

69. Sofiane, B., Didier, H. & Laurent, L. P. *Electrochimica Acta* 52**,** (2006), 62.

70. Pud, A., Ogurtsov, N., Korzhenko, A. & Shapoval, G. *Progress in Polymer Science (Oxford)* 28**,** (2003), 1701.

71. Elyashevich, G. K., Sidorovich, A. V., Smirnov, M. A., Kuryndin, I. S., Bobrova, N. V., Trchová, M. & Stejskal, J. *Polymer Degradation and Stability* 91**,** (2006), 2786.

72. Bhadra, J., Al-Thani, N. J., Madi, N. K. & Al-Maadeed, M. A. *Arabian Journal of Chemistry* 10**,** (2017), 664.

73. Bhadra, J., Madi, N. K., Al-Thani, N. J. & Al-Maadeed, M. A. *Synthetic Metals* 191**,** (2014), 126.

74. Del Castillo-Castro, T., Castillo-Ortega, M. M. & Herrera-Franco, P. J. *Composites Part A: Applied Science and Manufacturing* 40**,** (2009), 1573.

75. Kaiser, A. B., Subramaniam, C. K., Gilberd, P. W. & Wessling, B. *Synthetic Metals* 69**,** (1995), 197.

76. Jeevananda, T., Siddaramaiah, V., Annadurai, V. & Somashekar, R. *Journal of Applied Polymer Science* 82**,** (2001), 383.

77. Gomes de Souza, F., Almeida, M., Soares, B. G. & Carlos Pinto, J. *Polymer Testing* 26**,** (2007), 692.

78. Faez, R. & De Paoli, M.-A. *European Polymer Journal* 37**,** (2001), 1139.

79. Soto-Oviedo, M. A., Araújo, O. A., Faez, R., Rezende, M. C. & De Paoli, M.-A. *Synthetic Metals* 156**,** (2006), 1249.

80. Pan, W., Yang, S., Li, G. & Jiang, J. *International Journal of Polymeric Materials and Polymeric Biomaterials* 54**,** (2005), 21.

81. Barra, G. M. ., Jacques, L. B., Oréfice, R. L. & Carneiro, J. R. . *European Polymer Journal* 40**,** (2004), 2017.

82. Deng, H., Lin, L., Ji, M., Zhang, S., Yang, M. & Fu, Q. *Progress in Polymer Science* 39**,** (2014), 627.

83. Pang, H., Chen, C., Bao, Y., Chen, J., Ji, X., Lei, J. & Li, Z.-M. *Materials Letters* 79**,** (2012), 96.

84. Grunlan, J. C., Gerberich, W. W. & Francis, L. F. *Journal of Applied Polymer Science* 80**,** (2001), 692.

85. Grunlan, J. C., Gerberich, W. W. & Francis, L. F. *Polymer Engineering & Science* 41**,** (2001), 1947.

86. Tkalya, E. E., Ghislandi, M., de With, G. & Koning, C. E. *Current Opinion in Colloid and Interface Science* 17**,** (2012), 225.

87. Guo, B., Tang, Z. & Zhang, L. *Progress in Polymer Science* 61**,** (2016), 29.

88. Miriyala, S. M., Kim, Y. S., Liu, L. & Grunlan, J. C. *Macromolecular Chemistry and Physics* 209**,** (2008), 2399.

89. Grossiord, N., Wouters, M. E. L., Miltner, H. E., Lu, K., Loos, J., Mele, B. Van & Koning, C. E. *European Polymer Journal* 46**,** (2010), 1833.

90. Tkalya, E., Ghislandi, M., Alekseev, A., Koning, C. & Loos, J. *Journal of Materials Chemistry* 20**,** (2010), 3035.

91. Jurewicz, I., Worajittiphon, P., King, A. A. K., Sellin, P. J., Keddie, J. L. & Dalton, A. B. *The Journal of Physical Chemistry B* 115**,** (2011), 6395.

92. Mirmohseni, A. & Solhjo, R. *European Polymer Journal* 39**,** (2003), 219.

93. Beadle, P., Armes, S. P., Gottesfeld, S., Mombourquette, C., Houlton, R., Andrews, W. D. & Agnew, S. F. *Macromolecules* 25**,** (1992), 2526.

94. Xie, H.-Q., Ma, Y.-M. & Guo, J.-S. *Polymer* 40**,** (1999), 261.

95. Ruckenstein, E. & Yang, S. *Synthetic Metals* 53**,** (1993), 283.

96. Terlemezyan, L., Mihailov, M. & Ivanova, B. *Polymer Bulletin* 29**,** (1992), 283.

97. Gospodinova, N., Mokreva, P., Tsanov, T. & Terlemezyan, L. *Polymer* 38**,** (1997), 743.

98. Haba, Y., Segal, E., Narkis, M., Titelman, G. I. & Siegmann, A. *Synthetic Metals* 110**,** (2000), 189.

99. Haba, Y., Segal, E., Narkis, M., Titelman, G. . & Siegmann, A. *Synthetic Metals* 106**,** (1999), 59.

100. Goh, S. H., Chan, H. S. O. & Ong, C. H. *Polymer* 37**,** (1996), 2675.

101. Kanhegaokar, S. A. *e-Polymers* 7**,** (2007),

102. Segal, E., Haba, Y., Narkis, M. & Siegmann, A. *Journal of Applied Polymer Science* 79**,** (2001), 760.

103. Hosseini, S. H. & Entezami, A. A. *Iranian Polymer Journal* 14**,** (2005), 201.

104. Kumar, M. N. S. & Siddaramaiah. *Journal of Reinforced Plastics and Composites* 28**,** (2009), 2287.

105. Levin, Z. S., Robert, C., Feller, J. F., Castro, M. & Grunlan, J. C. *Smart Materials and Structures* 22**,** (2013), 15008.

106. Xi, H., Luo, L. & Fraisse, G. *Renewable and Sustainable Energy Reviews* 11**,** (2007), 923.

107. Omer, A. M. *Renewable and Sustainable Energy Reviews* 12**,** (2008), 2331.

108. Afshar, O., Saidur, R., Hasanuzzaman, M. & Jameel, M. *Renewable and Sustainable Energy Reviews* 16**,** (2012), 5639.

109. Kalkan, N., Young, E. A. & Celiktas, A. *Renewable and Sustainable Energy Reviews* 16**,** (2012), 6352.

110. Hamid Elsheikh, M., Abdulameer Shnawah, D., Mohd Sabri, M. F., Mohd Said, S. B., Haji Hassan, M., Ali Bashir, M. B. & Mohamad, M. *Renewable and Sustainable Energy Reviews* 30**,** (2014), 337.

111. Shu, G., Liang, Y., Wei, H., Tian, H., Zhao, J. & Liu, L. *Renewable and Sustainable Energy Reviews* 19**,** (2013), 385.

112. Martín-González, M., Caballero-Calero, O. & Díaz-Chao, P. *Renewable and Sustainable Energy Reviews* 24**,** (2013), 288.

113. Vélez, F., Segovia, J. J., Martín, M. C., Antolín, G., Chejne, F. & Quijano, A. *Renewable and*

Sustainable Energy Reviews 16**,** (2012), 4175.

114. Wang, T., Zhang, Y., Peng, Z. & Shu, G. *Renewable and Sustainable Energy Reviews* 15**,** (2011), 2862.

115. Liu, D., Zhao, F.-Y. & Tang, G.-F. *Renewable and Sustainable Energy Reviews* 14**,** (2010), 2736.

116. Fthenakis, V. & Kim, H. C. *Renewable and Sustainable Energy Reviews* 14**,** (2010), 2039.

117. Tie, S. F. & Tan, C. W. *Renewable and Sustainable Energy Reviews* 20**,** (2013), 82.

118. Ullah, K. R., Saidur, R., Ping, H. W., Akikur, R. K. & Shuvo, N. H. *Renewable and Sustainable Energy Reviews* 24**,** (2013), 499.

119. Bell, L. E. *Science* 321**,** (2008), 1457.

120. Gao, X., Uehara, K., Klug, D. D. & Tse, J. S. *Computational Materials Science* 36**,** (2006), 49.

121. Ioffe, A. F. *Semiconductor thermoelements and thermoelectric cooling*. (1957), (Infosearch, 1957).

122. Hicks, L. D. & Dresselhaus, M. S. *Physical Review B* 47**,** (1993), 16631.

123. Nolas, G. S., Morelli, D. T. & Tritt, T. M. *Annual Review of Materials Science* 29**,** (1999), 89.

124. Guo, J. Q., Geng, H. Y., Ochi, T., Suzuki, S., Kikuchi, M., Yamaguchi, Y. & Ito, S. *Journal of Electronic Materials* 41**,** (2012), 1036.

125. Venkatasubramanian, R., Siivola, E., Colpitts, T. & O'Quinn, B. *Nature* 413**,** (2001), 597.

126. Harman, T. C., Taylor, P. J., Walsh, M. P. & LaForge, B. E. *Science (New York, N.Y.)* 297**,** (2002), 2229.

127. Zheng, J. *Frontiers of Physics in China* 3**,** (2008), 269.

128. Qi, Y., Wang, Z., Zhang, M., Yang, F. & Wang, X. *Journal of Materials Chemistry A* 1**,** (2013), 6110.

129. Goldsmid, H. J. *Proceedings of the Physical Society* 71**,** (1958), 633.

130. Wang, B. *Next Big Future* (2014), Available at: https://www.nextbigfuture.com/2014/12/thermoelectrics-trying-to-hit-multi.html.

131. Du, Y., Shen, S. Z., Cai, K. & Casey, P. S. *Progress in Polymer Science* 37**,** (2012), 820.

132. Liang, L., Gao, C., Chen, G. & Guo, C.-Y. *Journal of Materials Chemistry C* 4**,** (2016), 526.

133. Shariki, S. *et al. Journal of Solid State Electrochemistry* 15**,** (2011), 2675.

134. Bubnova, O., Khan, Z. U., Malti, A., Braun, S., Fahlman, M., Berggren, M. & Crispin, X. *Nature Materials* 10**,** (2011), 429.

135. Park, T., Park, C., Kim, B., Shin, H. & Kim, E. *Energy & Environmental Science* 6**,** (2013), 788.

136. Wang, X., Meng, F., Wang, T., Li, C., Tang, H., Gao, Z., Li, S., Jiang, F. & Xu, J. *Journal of Alloys and Compounds* 734**,** (2018), 121.

137. Zhang, L., Harima, Y. & Imae, I. *Organic Electronics* 51**,** (2017), 304.

138. Wang, X., Meng, F., Tang, H., Gao, Z., Li, S., Jiang, F. & Xu, J. *Journal of Materials Science* 52**,** (2017), 9806.

139. Li, J., Du, Y., Jia, R., Xu, J. & Shen, S. *Materials* 10**,** (2017), 780.

140. Luo, S.-J., Zhang, P., Mei, Y.-A., Chang, J.-B., Ichikawa, S., Oshima, K., Toshima, N. & Yan, H. *Current Nanoscience* 13**,** (2017), 130.

141. Zhang, T., Li, K., Li, C., Ma, S., Hng, H. H. & Wei, L. *Advanced Electronic Materials* 3**,** (2017), 1600554.

142. Zhang, L., Goto, T., Imae, I., Sakurai, Y. & Harima, Y. *Journal of Polymer Science Part B: Polymer Physics* 55**,** (2017), 524.

143. Sun, X., Wei, Y., Li, J., Zhao, J., Zhao, L. & Li, Q. *Science China Materials* 60**,** (2017), 159.

144. Sarabia-Riquelme, R., Ramos-Fernández, G., Martin-Gullon, I. & Weisenberger, M. C. *Synthetic Metals* 222**,** (2016), 330.

145. Ju, H. & Kim, J. *ACS Nano* 10**,** (2016), 5730.

146. Son, W., Lee, S. H., Park, H., Choi, H. H. & Kim, J. H. *Journal of Electronic Materials* 45**,** (2016), 2935.

147. Dey, A., Maity, A., Shafeeuulla Khan, M. A., Sikder, A. K. & Chattopadhyay, S. *RSC Advances* 6**,** (2016), 22453.

148. Zhu, Z., Liu, C., Jiang, Q., Shi, H., Jiang, F., Xu, J., Xiong, J. & Liu, E. *Journal of Materials Science: Materials in Electronics* 26**,** (2015), 8515.

149. Xiong, J., Jiang, F., Shi, H., Xu, J., Liu, C., Zhou, W., Jiang, Q., Zhu, Z. & Hu, Y. *ACS Applied Materials & Interfaces* 7**,** (2015), 14917.

150. Zhu, Z., Liu, C., Shi, H., Jiang, Q., Xu, J., Jiang, F., Xiong, J. & Liu, E. *Journal of Polymer Science Part B: Polymer Physics* 53**,** (2015), 885.

151. Ju, H., Kim, M. & Kim, J. *Microelectronic Engineering* 136**,** (2015), 8.

152. Ju, H., Kim, M. & Kim, J. *Journal of Materials Science: Materials in Electronics* 26**,** (2015), 2544.

153. Lee, S. H., Park, H., Son, W., Choi, H. H. & Kim, J. H. *Journal of Materials Chemistry A* 2**,** (2014), 13380.

154. Culebras, M., Gómez, C. M. & Cantarero, A. *Journal of Materials Chemistry A* 2**,** (2014), 10109.

155. Lee, S. H., Park, H., Kim, S., Son, W., Cheong, I. W. & Kim, J. H. *Journal of Materials Chemistry A* 2**,** (2014), 7288.

156. Shi, H., Liu, C., Xu, J., Song, H., Jiang, Q., Lu, B., Zhou, W. & Jiang, F. *International Journal of Electrochemical Science* 9**,** (2014), 7629.

157. Wang, Y., Cai, K., Chen, S., Shen, S. & Yao, X. *Journal of Nanoparticle Research* 16**,** (2014), 2531.

158. Wang, J., Cai, K. & Shen, S. *Organic Electronics* 15**,** (2014), 3087.

159. Song, H., Kong, F., Liu, C., Xu, J., Jiang, Q. & Shi, H. *Journal of Polymer Research* 20**,** (2013), 316.

160. Kato, K., Hagino, H. & Miyazaki, K. *Journal of Electronic Materials* 42**,** (2013), 1313.

161. Kong, F., Liu, C., Xu, J., Huang, Y., Wang, J. & Sun, Z. *Journal of Electronic Materials* 41**,** (2012), 2431.

162. Liu, C. *et al. Synthetic Metals* 160**,** (2010), 2481.

163. See, K. C., Feser, J. P., Chen, C. E., Majumdar, A., Urban, J. J. & Segalman, R. A. *Nano letters* 10**,** (2010), 4664.

164. Scholdt, M., Do, H., Lang, J., Gall, A., Colsmann, A., Lemmer, U., Koenig, J. D., Winkler, M. & Boettner, H. *Journal of Electronic Materials* 39**,** (2010), 1589.

165. Kim, D., Kim, Y., Choi, K., Grunlan, J. C. & Yu, C. *ACS Nano* 4**,** (2010), 513.

166. Limelette, P., Schmaltz, B., Brault, D., Gouineau, M., Autret-Lambert, C., Roger, S., Grimal, V. & Tran Van, F. *Journal of Applied Physics* 115**,** (2014), 033712.

167. Wu, J., Sun, Y., Xu, W. & Zhang, Q. *Synthetic Metals* 189**,** (2014), 177.

168. Lin, Y.-H., Lee, T.-C., Hsiao, Y.-S., Lin, W.-K., Whang, W.-T. & Chen, C.-H. *ACS Applied Materials &*

Interfaces 10**,** (2018), 4946.

169. Wang, L., Bi, H., Yao, Q., Ren, D., Qu, S., Huang, F. & Chen, L. *Composites Science and Technology* 150**,** (2017), 135.

170. Yao, Q., Chen, L., Zhang, W., Liufu, S. & Chen, X. *ACS Nano* 4**,** (2010), 2445.

171. Wang, L., Wang, D., Zhu, G., Li, J. & Pan, F. *Materials Letters* 65**,** (2011), 1086.

172. Toshima, N. *Macromolecular Symposia* 186**,** (2002), 81.

173. Li, J., Tang, X., Li, H., Yan, Y. & Zhang, Q. *Synthetic Metals* 160**,** (2010), 1153.

174. Toshima, N., Imai, M. & Ichikawa, S. *Journal of Electronic Materials* 40**,** (2011), 898.

175. Wang, W., Sun, S., Gu, S., Shen, H., Zhang, Q., Zhu, J., Wang, L. & Jiang, W. *RSC Advances* 4**,** (2014), 26810.

176. An, C. J., Kang, Y. H., Lee, A.-Y., Jang, K.-S., Jeong, Y. & Cho, S. Y. *ACS Applied Materials & Interfaces* 8**,** (2016), 22142.

177. Chatterjee, M. J., Banerjee, D. & Chatterjee, K. *Materials Research Express* 3**,** (2016), 085009.

178. Wang, Y., Zhang, S. M. & Deng, Y. *Journal of Materials Chemistry A* 4**,** (2016), 3554.

179. Mitra, M., Kulsi, C., Chatterjee, K., Kargupta, K., Ganguly, S., Banerjee, D. & Goswami, S. *RSC Advances* 5**,** (2015), 31039.

180. Roussel, F., Chen Yu King, R., Kuriakose, M., Depriester, M., Hadj-Sahraoui, A., Gors, C., Addad, A. & Brun, J.-F. *Synthetic Metals* 199**,** (2015), 196.

181. Wang, W., Zhang, Q., Li, J., Liu, X., Wang, L., Zhu, J., Luo, W. & Jiang, W. 5**,** (2015), 8988.

182. Harima, Y., Fukumoto, S., Zhang, L., Jiang, X., Yano, J., Inumaru, K. & Imae, I. *RSC Advances* 5**,** (2015), 86855.

183. Yao, Q., Wang, Q., Wang, L. & Chen, L. *Energy & Environmental Science* 7**,** (2014), 3801.

184. Zheng, B., Liu, Y., Zhan, B., Lin, Y., Lan, J. & Yang, X. *Journal of Electronic Materials* 43**,** (2014), 3695.

185. Anno, H., Hokazono, M., Akagi, F., Hojo, M. & Toshima, N. *Journal of Electronic Materials* 42**,** (2013), 1346.

186. Zhang, K., Davis, M., Qiu, J., Hope-Weeks, L. & Wang, S. *Nanotechnology* 23**,** (2012), 385701.

187. Wu, J., Sun, Y., Pei, W.-B., Huang, L., Xu, W. & Zhang, Q. *Synthetic Metals* 196**,** (2014), 173.

188. Tang, X., Liu, T., Li, H., Yang, D., Chen, L. & Tang, X. *RSC Advances* 7**,** (2017), 20192.

189. Wang, L., Liu, F., Jin, C., Zhang, T. & Yin, Q. *RSC Advances* 4**,** (2014), 46187.

190. Goupil, C., Seifert, W., Zabrocki, K., Müller, E. & Snyder, G. J. *Entropy* 13**,** (2011), 1481.

191. Snyder, G. J. & Toberer, E. S. *Nature Materials* 7**,** (2008), 105.

192. Mott, N. F. & Jones, H. *The theory of the properties of metals and alloys*. (1958), (Courier Corporation, 1958).

193. Khan, Z. U., Edberg, J., Hamedi, M. M., Gabrielsson, R., Granberg, H., Wågberg, L., Engquist, I., Berggren, M. & Crispin, X. *Advanced Materials* 28**,** (2016), 4556.

194. Bubnova, O. & Crispin, X. *Energy & Environmental Science* 5**,** (2012), 9345.

195. Jin, J., Wang, Q. & Haque, M. A. *Journal of Physics D: Applied Physics* 43**,** (2010), 205302.

196. Oh Yoon, C., Hyun Kim, J., Kyung Sung, H. & Lee, H. *Synthetic Metals* 84**,** (1997), 789.

197. Rowe, D. M. & Min, G. *Journal of Materials Science Letters* 14**,** (1995), 617.

198. Dey, A., Bajpai, O. P., Sikder, A. K., Chattopadhyay, S. & Shafeeuulla Khan, M. A. *Renewable and Sustainable Energy Reviews* 53**,** (2016), 653.

199. Yu, C., Kim, Y. S., Kim, D. & Grunlan, J. C. *Nano Letters* 9**,** (2009), 1283.

200. Meng, C., Liu, C. & Fan, S. *Advanced Materials* 22**,** (2010), 535.

201. Yan, H. & Kou, K. *Journal of Materials Science* 49**,** (2014), 1222.

202. Kim, G. & Pipe, K. P. *Physical Review B* 86**,** (2012), 085208.

203. Kim, G. H., Hwang, D. H. & Woo, S. I. *Physical Chemistry Chemical Physics* 14**,** (2012), 3530.

204. Zhang, K., Zhang, Y. & Wang, S. *Scientific Reports* 3**,** (2013), 3448.

205. Wang, Y., Yang, J., Wang, L., Du, K., Yin, Q. & Yin, Q. *ACS Applied Materials & Interfaces* 9**,** (2017), 20124.

206. Zhang, B., Sun, J., Katz, H. E., Fang, F. & Opila, R. L. *ACS Applied Materials & Interfaces* 2**,** (2010), 3170.

207. Zhang, Q., Sun, Y., Xu, W. & Zhu, D. *Advanced Materials* 26**,** (2014), 6829.

208. Levy, O. & Stroud, D. *Journal of Physics: Condensed Matter* 9**,** (1997), L599.

209. Park, H. W., Kim, T., Huh, J., Kang, M., Lee, J. E. & Yoon, H. *ACS Nano* 6**,** (2012), 7624.

210. Culebras, M., Gómez, C. & Cantarero, A. *Materials* 7**,** (2014), 6701.

211. Szczech, J. R., Higgins, J. M. & Jin, S. *J. Mater. Chem.* 21**,** (2011), 4037.

212. Groenendaal, L., Jonas, F., Freitag, D., Pielartzik, H. & Reynolds, J. R. *Advanced Materials* 12**,** (2000), 481.

213. Lee, K., Cho, S., Park, S. H., Heeger, A. J., Lee, C.-W. & Lee, S.-H. *Nature* 441**,** (2006), 65.

214. Cao, Y., Qiu, J. & Smith, P. *Synthetic Metals* 69**,** (1995), 187.

215. MacDiarmid, A. G. & Epstein, A. J. *Synthetic Metals* 65**,** (1994), 103.

216. Jönsson, S. K. ., Birgerson, J., Crispin, X., Greczynski, G., Osikowicz, W., Denier van der Gon, A. ., Salaneck, W. . & Fahlman, M. *Synthetic Metals* 139**,** (2003), 1.

217. Döbbelin, M., Marcilla, R., Salsamendi, M., Pozo-Gonzalo, C., Carrasco, P. M., Pomposo, J. A. & Mecerreyes, D. *Chemistry of Materials* 19**,** (2007), 2147.

218. Kim, J. Y., Jung, J. H., Lee, D. E. & Joo, J. *Synthetic Metals* 126**,** (2002), 311.

219. Luo, J. *et al. Journal of Materials Chemistry A* 1**,** (2013), 7576.

220. Tomlinson, E. P., Hay, M. E. & Boudouris, B. W. *Macromolecules* 47**,** (2014), 6145.

221. Tomlinson, E. P., Willmore, M. J., Zhu, X., Hilsmier, S. W. A. & Boudouris, B. W. *ACS Applied Materials & Interfaces* 7**,** (2015), 18195.

222. Zhao, J., Tan, D. & Chen, G. *Journal of Materials Chemistry C* 5**,** (2017), 47.

223. Hiroshige, Y., Ookawa, M. & Toshima, N. *Synthetic Metals* 157**,** (2007), 467.

224. Scholes, D. T., Hawks, S. A., Yee, P. Y., Wu, H., Lindemuth, J. R., Tolbert, S. H. & Schwartz, B. J. *The Journal of Physical Chemistry Letters* 6**,** (2015), 4786.

225. Sun, J., Yeh, M.-L., Jung, B. J., Zhang, B., Feser, J., Majumdar, A. & Katz, H. E. *Macromolecules* 43**,** (2010), 2897.

226. Zhang, Q., Sun, Y., Xu, W. & Zhu, D. *Macromolecules* 47**,** (2014), 609.

227. Søndergaard, R. R., Hösel, M., Espinosa, N., Jørgensen, M. & Krebs, F. C. *Energy Science & Engineering* 1**,** (2013), 81.

228. Leonov, V., Torfs, T., Fiorini, P. & Van Hoof, C. *IEEE Sensors Journal* 7**,** (2007), 650.

229. Hyland, M., Hunter, H., Liu, J., Veety, E. & Vashaee, D. *Applied Energy* 182**,** (2016), 518.

230. Arias, A. C., MacKenzie, J. D., McCulloch, I., Rivnay, J. & Salleo, A. *Chemical Reviews* 110**,** (2010), 3.

231. Rogers, J. A., Someya, T. & Huang, Y. *Science (New York, N.Y.)* 327**,** (2010), 1603.

232. Schwartz, G., Tee, B. C.-K., Mei, J., Appleton, A. L., Kim, D. H., Wang, H. & Bao, Z. *Nature Communications* 4**,** (2013), 1859.

233. Hatchett, D. W. & Josowicz, M. *Chemical Reviews* 108**,** (2008), 746.

234. Persaud, K. C. *Materials Today* 8**,** (2005), 38.

235. Huang, J., Virji, S., Weiller, B. H. & Kaner, R. B. *Chemistry – A European Journal* 10**,** (2004), 1314.

236. Roh, J. G., Hwang, H. R., Yu, J. B., Lim, J. O. & Huh, J. S. *Journal of Macromolecular Science, Part A* 39**,** (2002), 1095.

237. Adhikari, B. & Majumdar, S. *Progress in Polymer Science* 29**,** (2004), 699.

238. Su, C., Wang, G., Huang, F. & Sun, Y. *Farong Huang & Yanhua Sun Journal of Macromolecular Science, Part B* 47**,** (2007), 65.

239. Ferrreira, A., Rocha, J. G., Ansón-Casaos, A., Martínez, M. T., Vaz, F. & Lanceros-Mendez, S. *Sensors and Actuators, A: Physical* 178**,** (2012), 10.

240. Falletta, E., Costa, P., Della Pina, C. & Lanceros-Mendez, S. *Sensors and Actuators A: Physical* 220**,** (2014), 13.

241. Kanoun, O., Müller, C., Benchirouf, A., Sanli, A., Dinh, T., Al-Hamry, A., Bu, L., Gerlach, C. & Bouhamed, A. *Sensors* 14**,** (2014), 10042.

242. Lu, J., Feller, J. F., Kumar, B., Castro, M., Kim, Y. S., Park, Y. T. & Grunlan, J. C. *Sensors and Actuators B: Chemical* 155**,** (2011), 28.

243. Li, B., Zhang, Y.-C., Li, Z.-M., Li, S.-N. & Zhang, X.-N. *The Journal of Physical Chemistry B* 114**,** (2010), 689.

244. Droval, G., Feller, J. F., Salagnac, P. & Glouannec, P. *Smart Materials and Structures* 17**,** (2008), 025011.

245. Shukla, S. K. & Kushwaha, C. S. *Materials Today: Proceedings* 4**,** (2017), 5672.

246. Le, T.-H., Kim, Y. & Yoon, H. *Polymers* 9**,** (2017), 150.

247. Li, G., Martinez, C. & Semancik, S. *Journal of the American Chemical Society* 127**,** (2005), 4903.

248. Lim, J.-H., Phiboolsirichit, N., Mubeen, S., Deshusses, M. A., Mulchandani, A. & Myung, N. V. *Nanotechnology* 21**,** (2010), 075502.

249. Do, J.-S. & Wang, S.-H. *Sensors and Actuators B: Chemical* 185**,** (2013), 39.

250. Tai, H., Jiang, Y., Xie, G., Yu, J. & Chen, X. *Sensors and Actuators B: Chemical* 125**,** (2007), 644.

251. Shukla, S. K., Shukla, S. K., Govender, P. P. & Agorku, E. S. *Microchimica Acta* 183**,** (2016), 573.

252. Bhanvase, B. A., Darda, N. S., Veerkar, N. C., Shende, A. S., Satpute, S. R. & Sonawane, S. H. *Ultrasonics Sonochemistry* 24**,** (2015), 87.

253. Athawale, A. A., Bhagwat, S. V. & Katre, P. P. *Sensors and Actuators B: Chemical* 114**,** (2006), 263.

254. Choudhury, A. *Sensors and Actuators B: Chemical* 138**,** (2009), 318.

255. Sharma, S., Nirkhe, C., Pethkar, S. & Athawale, A. A. *Sensors and Actuators B: Chemical* 85**,** (2002), 131.

256. Dixit, V., Misra, S. C. K. & Sharma, B. S. *Sensors and Actuators B: Chemical* 104**,** (2005), 90.

257. Gonçalves, B. F., Oliveira, J., Costa, P., Correia, V., Martins, P., Botelho, G. & Lanceros-Mendez, S. *Composites Part B: Engineering* 112**,** (2017), 344.

258. Cochrane, C., Koncar, V., Lewandowski, M. & Dufour, C. *Sensors* 7**,** (2007), 473.

259. Mattmann, C., Clemens, F. & Tröster, G. *Sensors* 8**,** (2008), 3719.

260. Zhang, R., Baxendale, M. & Peijs, T. *Physical Review B - Condensed Matter and Materials Physics* 76**,** (2007), 195433.

261. Flandin, L., Chang, A., Nazarenko, S., Hiltner, A. & Baer, E. *Journal of Applied Polymer Science* 76**,** (2000), 894.

262. Martinez, F., Obieta, G., Uribe, I., Sikora, T. & Ochoteco, E. *Journal of Sensors* 2010**,** (2010), 1.

263. Knite, M., Ozols, K., Sakale, G. & Teteris, V. *Sensors and Actuators B: Chemical* 126**,** (2007), 209.

264. Knite, M., Hill, A. J., Pas, S. J., Teteris, V. & Zavickis, J. *Materials Science and Engineering: C* 26**,** (2006), 771.

265. Knite, M., Tupureina, V., Fuith, A., Zavickis, J. & Teteris, V. *Materials Science and Engineering: C* 27**,** (2007), 1125.

266. Bilotti, E., Zhang, R., Deng, H., Baxendale, M. & Peijs, T. *Journal of Materials Chemistry* 20**,** (2010), 9449.

267. Teixeira, J., Horta-Romarís, L., Abad, M. J., Costa, P. & Lanceros-Méndez, S. *Materials and Design* 141**,** (2018), 1.

268. Costa, C. M., Rodrigues, L. C., Sencadas, V., Silva, M. M., Rocha, J. G. & Lanceros-Méndez, S. *Journal of Membrane Science* 407**–**408**,** (2012), 193.

269. Radhakrishnan, S. & Kar, S. B. *Sensors and Actuators A: Physical* 120**,** (2005), 474.

270. Kollosche, M., Stoyanov, H., Laflamme, S. & Kofod, G. *Journal of Materials Chemistry* 21**,** (2011), 8292.

271. Brady, S., Diamond, D. & Lau, K.-T. *Sensors and Actuators A: Physical* 119**,** (2005), 398.

CAPÍTULO 2:

Objetivos y estructura de la tesis

OBJETIVOS

El objetivo general de este trabajo de tesis fue el diseño y caracterización de nuevos polímeros intrínsecamente conductores, basados en polianilinas, enfocados a aplicaciones generales en electrónica, desarrollo de nuevos sensores y también para utilizar en la fabricación de nuevos generadores termoeléctricos.

Para ello se estudió con profundidad, la incidencia del uso de distintos dopantes y rutas de síntesis para la obtención de la polianilina (PANI), en sus propiedades termoeléctricas, termorresistivas y piezoeléctricas. Además, con el fin de mejorar las propiedades mecánicas del polímero sintetizado y abaratar su coste, se formularon nuevos materiales compuestos utilizando una matriz polimérica de bajo coste como es el acetato de polivinilo. Las prestaciones de los nuevos compuestos fueron evaluadas con el objetivo de obtener la mejor ratio entre coste y propiedades.

A continuación, se detallan los objetivos específicos del trabajo que serán desarrollados a lo largo de la memoria de la tesis.

1. Seleccionar la mejor ruta de síntesis (directa o indirecta) y dopante (orgánico o inorgánico) para la obtención de polianilinas con buenas propiedades eléctricas y alta estabilidad térmica. Relacionar sus propiedades físico-químicas con la morfología de las polianilinas obtenidas.
2. Evaluar el comportamiento de las polianilinas sintetizadas como sensores térmicos a través ciclos de enfriamiento y calentamiento.
3. Evaluar la eficiencia termoeléctrica de las polianilinas dopadas con ácidos orgánicos (como el DBSA y NaSIPA) mediante la medida de la conductividad eléctrica, conductividad térmica y coeficiente de Seebeck a distintas temperaturas.
4. Estudiar los mecanismos de conducción de las polianilinas dopadas con ácidos orgánicos (como el DBSA y NaSIPA) para comprender su comportamiento termoeléctrico.
5. Diseñar compuestos conductores flexibles utilizando acetato de polivinilo (PVAc) como matriz y polianilina como carga conductora. Evaluar la relación entre el porcentaje de polianilina y la conductividad eléctrica y coeficiente de Seebeck de los compuestos.

6. Analizar la viabilidad de los filmes PVAc/PANI, como sensores piezoresistivos, evaluando su eficiencia a través del cálculo del Gauge Factor y su sensibilidad, en función de la composición del compuesto.

1. Relevancia de los objetivos propuestos

Dada la crisis energética en la que vivimos, con una excesiva dependencia de los combustibles fósiles y el impacto medioambiental que supone su uso, el desarrollo de tecnologías limpias para generar energía eléctrica es un tema de máximo interés a todos los niveles. Los sistemas de generación de energía actuales, tienen una eficiencia mejorable, pues desperdician una parte importante del calor que necesitan para la producción de electricidad (por ejemplo, centrales termoeléctricas, celdas fotoeléctricas, etc). El uso de generadores termoeléctricos que aprovechen este calor residual para producir electricidad, mejora la eficiencia de todos estos sistemas.

A pesar de que la termoelectricidad no es un concepto nuevo, se ha puesto de "moda" en los últimos años como una alternativa que ofrece energía limpia y sostenible. Sin embargo, la baja eficiencia termodinámica de los generadores actuales, así como el coste y el impacto medioambiental de la producción de materiales termoeléctricos inorgánicos (los más usados en las aplicaciones actuales) frenan la aplicación masiva de estos dispositivos. Los polímeros intrínsecamente conductores (ICPs), suponen una alternativa asequible y más amigable con el medio ambiente que los termoeléctricos inorgánicos. Y aunque, en general su eficiencia termoeléctrica es más baja a temperaturas de trabajo elevadas, a temperaturas en torno a la temperatura ambiente, los valores son comparables. A mayores los materiales termoeléctricos orgánicos ofrecen otras posibilidades, como la fabricación de dispositivos de bajo peso o en forma de film. Por otra parte, el diseño de sensores tanto piezoresistivos, como de temperatura de alta sensibilidad también es un campo donde los ICPs tienen prometedoras posibilidades, por su versatilidad y por su fácil integración con los otros componentes. Esta vía de investigación también es de gran interés a nivel industrial, puesto que los paradigmas de la Industria 4.0 se basan en un incremento sustancial en la monitorización de todos los pasos y elementos del proceso de producción y para ello, el desarrollo de nuevos sensores es imprescindible.

En este contexto, todos los expertos coinciden en que aún no se ha alcanzado el techo en cuanto a las aplicaciones de los ICPs y por ello, la investigación y desarrollo en este tipo de polímeros está sobradamente justificada.

Las polianilinas, a pesar de no tener tan buenas propiedades eléctricas y termoeléctricas como otros ICPs (por ejemplo el PEDOT:PSS) presentan sin embargo, una versatilidad envidiable, desde el punto de vista de las modificaciones químicas y morfológicas que unido a su procesabilidad sencilla y económica permiten que sea fácilmente escalable a producción industrial.

De todo lo expuesto anteriormente, se puede concluir que los objetivos que se proponen alcanzar en el desarrollo del trabajo de esta tesis son de gran interés, no solo desde el punto de vista científico-académico sino también, desde el ámbito tecnológico e industrial.

2. Estructura de la memoria de la tesis

A continuación, se expone un resumen de los contenidos de cada uno de los capítulos de la memoria del trabajo de tesis:

Capítulo 1: Introducción

Capítulo 2: Objetivos y estructura de la tesis

Capítulo 3: Cyclic temperature dependence of electrical conductivity in polyanilines as a function of the dopant and synthesis method

Capítulo 4: Thermoelectric properties and intrinsic conduction processes in DBSA and NaSIPA doped polyanilines

Capítulo 5: Multifunctional electromechanical and thermoelectric polyaniline-poly(vinyl acetate) latex composites for wearable devices

Capítulo 6: Conclusiones

Anexos: Financiación recibida, contribuciones a congresos y portada de artículos

CAPÍTULO 3:

Cyclic temperature dependence of electrical conductivity in polyanilines as a function of the dopant and synthesis method

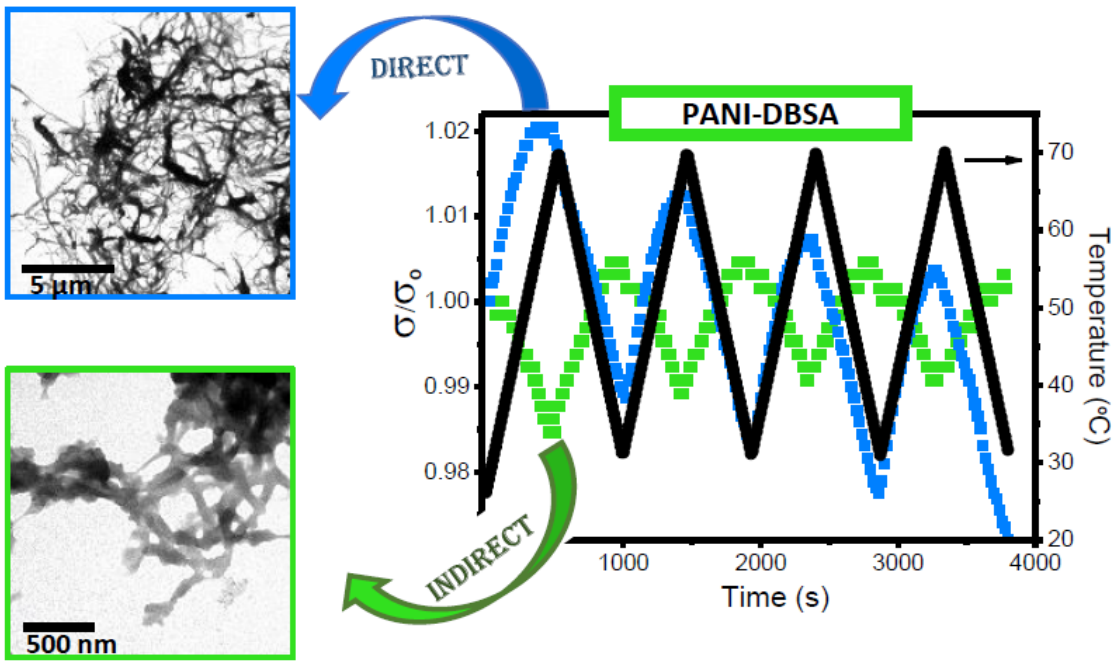

Basado en el artículo:

Horta-Romarís, L., Abad, M.-J., González-Rodríguez, M. V., Lasagabáster, A., Costa, P. & Lanceros-Méndez, S. *Materials & Design* 114**,** (2017), 288.

1. Introduction

In recent years, there has been increasing interest in the synthesis and application of conducting polymers [1]. Specifically, polyanilines (PANIs) are the subject of considerable attention owing to their unique electrical behavior, good environmental stability in doped and neutral states and simple synthesis [2].

PANI has a broad application range covering rechargeable batteries [3], data storage [4], corrosion protections [5], solar cell devices [6] and sensors [7-10], among others. Polyaniline is an excellent candidate for fabricating sensor devices due their intrinsic electrical properties. It possesses valuable characteristics such as reversible acid/base doping/dedoping chemistry, enabling control over properties (free volume, conformational changes, solubility, electrical conductivity and optical activity) which result in sensitive and rapid responses to specific analytes and/or environmental factors [9].

In order to develop thermal sensors, it is essential to understand the temperature dependence of the electrical conductivity. Thus, from a theoretical point of view, it is common practice to study the variation of conductivity with temperature in the range of ~50- 300 K to comprehend the mechanism of conductivity [11,12]. Notwithstanding, in practice these devices are often applied at room temperate and above. As a result, the thermal stability of conductivity in the latter temperature range is critical. A greater number of factors should be considered as in these conditions different changes are taking place in the system like doping, dedoping (extrinsic), oxidation, chain scission, cross-linking and changes in crystal structure (intrinsic) [13]. In addition, the study of the thermal stability of polyaniline is essential to understand the effect of heat treatment on physical properties. Despite the number of studies focusing on the improvement of the electrical properties of PANI, those analyzing the influence of thermal aging on these properties are relatively scarce [13-17].

In this context, the main objective of this work is to develop reliable, eco-friendly and scalable synthetic routes for large-scale production of polyaniline intended for the manufacture of sensors, including thermal sensors. As the chemical oxidation of aniline is more suitable than electrochemical polymerization for bulk production [18-20], the first alternative has been investigated. Concerning the synthetic methods, the properties of

polyaniline can be tailored through doping with a wide scope of dopants and using direct and indirect approaches.

Regarding direct synthesis, HCl has been chosen as inorganic dopant due to the ease of synthesis and high electrical conductivity [21]. Dodecylbenzene sulfonic acid (DBSA) has been selected among organic dopants owing to the well-known enhancement of processability, as DBSA acts both as dopant (DBSA bonded to PANI backbone) and plasticizer (DBSA in excess or free DBSA) [20].

Another option is to obtain a synergistic combination between the high conductivity of the inorganic dopant and the improvement in processability and thermal stability achieved with the organic dopant by an indirect synthetic route, known as *dedoping-redoping* [11]. In this option, polyaniline doped with HCl (PANI-HCl) is completely dedoped in aqueous NH_4OH solution and, subsequently, redoped with a second organic dopant. As second organic dopants, the bulky counterions DBSA and sodio-5-sulfoisophtalic acid (NaSIPA) have been used [11].

The polymers thus synthesized were characterized using transmission electron microscopy (TEM), Fourier transform infrared spectroscopy (FTIR), Elemental Analysis, X-ray photoelectron spectroscopy (XPS), X-ray diffraction (XRD) and Thermogravimetric analysis (TGA). Their room temperature electrical conductivity has been compared by the four probe technique and the effects of various dopants and synthetic routes on DC conductivity are discussed. Finally, thermal stability of the DC electrical conductivity was monitored at different heating conditions and through heating-cooling cycles to analyze the potential of PANIs as thermal sensors.

2. Experimental

2.1. Materials synthesis

Aniline and potassium peroxodisulfate (APS) were purchased from Fluka (Steinheim, Germany). Dodecylbenzensulfonic acid (DBSA) 70 wt.% solution in 2-propanol and 5-sulfoisophtalic acid sodium salt (NaSIPA) 95 wt.% were obtained from Sigma–Aldrich (Steinheim, Germany), acetone was obtained from Scharlau (Sentmenat, Spain), chloroform and methanol were supplied from Merck (Darmstadt, Germany). All the solvents and reagents except DBSA were at least of 99% purity. Water was purified on a Milli-QUltrapure 109 system (Millipore, Molsheim, France).

Table 1 summarizes the main synthesis conditions and the sample nomenclature. The preparation of PANI-HCl (P1) was adapted from the method described by Park et al [22]. Aniline and APS were dissolved separately in 0.5M aqueous HCl. The polymerization reaction was initiated by the drop wise addition of the oxidant during approximately 20 minutes. Afterwards, the reaction was allowed to proceed for 2 h under mechanic stirring (350 rpm) at room temperature. The precipitate was filtered under vacuum and washed with a mixture of 1:1 water:acetone. The PANI-HCl was obtained as a dark green powder after drying at 40 °C in vacuum until constant weight.

The polymerization of polyaniline doped with DBSA (PANI-DBSA direct synthesis) (P2) was prepared according to the method described by Dopico et al [23].

For the indirect synthesis, PANI-HCl prepared as described in the preceding paragraph, was dedoped with 1M NH_3 for 2 h in ultrasonic bath, filtered under vacuum and washed with water until neutral pH. The resultant product was redoped with 1M DBSA in acetone and 0.5 M aqueous NaSIPA during 2h in ultrasonic bath leading to PANI-DBSA indirect synthesis (P3) and PANI-NaSIPA (P4), respectively. This indirect procedure has the advantage of avoiding chloroform (less environmentally-friendly) which is used in the direct polymerization of PANI-DBSA. The samples were washed with large volumes of acetone to remove excess free acids. Finally, the products were filtered under vacuum and dried in vacuum at 40 °C for 2 days [11].

After polymerization, the polyanilines thus prepared were stored inside an opaque container in a desiccator, to protect them from light and moisture until tests execution.

Table 1. Experimental procedure for the synthesis conditions of doped PANI.

	Sample	Dopant	$M:D_1:O:D_2$	T (°C)	Addition dropwise speed	Stirring speed (rpm)
PANI direct synthesis	**P1**	HCl	1 : 5.6 : 1.25	RT	>1 drop/sec	350
	P2	DBSA	1:3:1	0-5	<1 drop/sec	150
PANI indirect synthesis	**P3**	HCl-DBSA	1 : 5.6 : 1.25 : 5.6	RT	>1 drop/sec	350
	P4	HCl-NaSIPA	1 : 5.6 :1.25 : 2.8	RT	>1 drop/sec	350

2.2. Characterization

The transmission electron microscope (TEM, Jeol JEM 1010, 80 KV) was used to investigate the morphology of the powder samples dispersed in isopropanol.

Fourier transformed infrared (FTIR) spectra of the polymers in KBr pellets were recorded on a Bruker Vector 22 spectrometer. The spectra were collected from 4000 to 400 cm^{-1} with a 4 cm^{-1} resolution over 100 scans.

The elemental analysis of C, H, N, S was conducted using ThermoFinnigan FlashEA1112 elemental analyzer.

The XPS spectra were performed with a Thermo Scientific K-Alpha ESCA instrument with Al-Kα monochromatized radiation at 1486.6 eV X-ray source, operated in a constant analyser energy mode (CAE) with 100 eV and 20 eV pass energy for survey and high resolution spectra, respectively. All core-level spectra were referenced to the C1s neutral carbon peak at 285 eV. The atomic concentrations were determined from the XPS peak areas using the Shirley background subtraction technique and the Scofield sensitivity factors. The N(1s), S(2p) and Cl(2p) peaks were deconvoluted into Gaussian\Lorentzian component peaks by the manufacturer (Thermofisher) software (Avantage version 5.47).

X-ray patterns of polyaniline powders were recorded in step-scan mode from 2° to 50° with a 2θ step of 0.05° using a D5000 diffractometer (XRD, Siemens- Bruker) with CuKα line irradiation (λ= 1.541 $x10^{-10}$m). 40-point smoothing protocol using a Savitzky-Golay filter has been applied to the diffractograms, which were normalized to area 1 (Origin 8.0 graphical software). A split Gaussian function was used to subtract the background and amorphous contributions using the open-source software Fityk. The difference patterns were deconvoluted into the crystalline constituents using Gaussian function peak shape approximation [24]. The degree of crystallinity (X_c) was estimated from the percentage of crystalline peak area to total scattered area, the d-spacing was calculated using the Bragg equation, the crystallite domain size (L) was evaluated using the Scherrer formula [25]. The interchain separation lengths (R) of the highest intense crystalline peaks were determined from the relation given by Klug and Alexander [26].

Thermogravimetric analysis (TGA) was performed with a Perkin-Elmer TGA-7 over a temperature range of 25–700 °C, at a heat rate of 10 °C/min under oxygen atmosphere. Electrical resistivity was measured with a LORESTA-GP electrical analyzer

(Mitsubishi Chemical, MCP-T610) on specimens prepared by compression molding (2.5x2.5 cm x 0.5 mm). The measuring range of this equipment lies between 10^{-2} - 10^{7} Ω. Measurements were conducted at room temperature using a 4-point test fixture (gold contact wires with and inter-pin distance of 5 mm). The electrical conductivities reported (the inverse of electrical resistivity) for each polymer are the mean values of at least 24 readings determined on different probes.

The temperature dependence of the electrical resistance was measured under oxygen atmosphere with the digital multimeter Agilent 34401A (DC) in synchronization with the temperature control Linkam THMSE 600. The data were recorded every second for the different samples and temperatures ranges. Three different tests were performed: all samples were subjected to a heating ramp until 200 °C at 2 °C/min; besides, only P2 and P3 were subjected to a heating ramp until 350 °C at 10 °C/min and to heating-cooling cycles between 30 - 70 °C (5 °C/min).

In order to mimic the real working conditions of the material in sensor applications all the thermal tests were carried out under oxygen atmosphere.

3. Results and discussion

3.1. Morphological properties

The most noteworthy properties of polyanilines, in particular electrical properties, become dependent on their morphology, size and shape, when dimensions are decreased to the nanoscale. The TEM micrographs of the four PANI salts are presented in **Figure 1**. There are differences in the shape and size of the particles depending on the chemical nature of the dopant and the synthetic parameters. The particles of PANI-HCl (P1 in **Figure 1A**) and the polyanilines obtained by indirect synthesis (**Figure 1C** and **1D**) are nanorod shaped. These nanostructures are fully appreciated on a larger scale in the insets of **Figure 1A**, **C** and **D**. By contrast, the P2 fibrils of **Figure 1B**, show micrometric dimensions.

Regarding P1, the rate of the aqueous polymerization at room temperature, with higher monomer:acid and monomer:oxidant ratios, is necessarily faster than the emulsion polymerization kinetic of P2 at 0-5 °C; thus, nucleation processes are favored over the polymer growth and explains the nanoscale morphology. Notwithstanding, the concentration of monomer and oxidant are low enough to produce nanorods in

the presence of inorganic acids at extremely low pH values (pH≈0), instead of the typical granular morphology, usually produced by the precipitation polymerization in strongly acidic media [27].

On the other hand, P2 has been prepared by aqueous/organic interfacial polymerization in the presence of DBSA with lower aniline: acid and aniline: APS ratios and at lower temperature than the PANI-HCl. Several factors contribute to the microfibrillar morphology obtained by this procedure. First of all, the reactants and oligomeric intermediates are distributed between the aqueous and organic phases, creating the typical conditions of a dilution technique [28]. Secondly, the interface is expected to be crucial for the adsorption of nucleates and their organization rate [29]. In the third place, the low temperature further favors slow polymerization kinetics. Last, but not least, the pH profile is also relevant: weak organic acids bring the initial pH to the desired low-acidity level and further act as buffers, that resist the pH decrease caused by the produced sulfuric acid when APS is the oxidant [27].

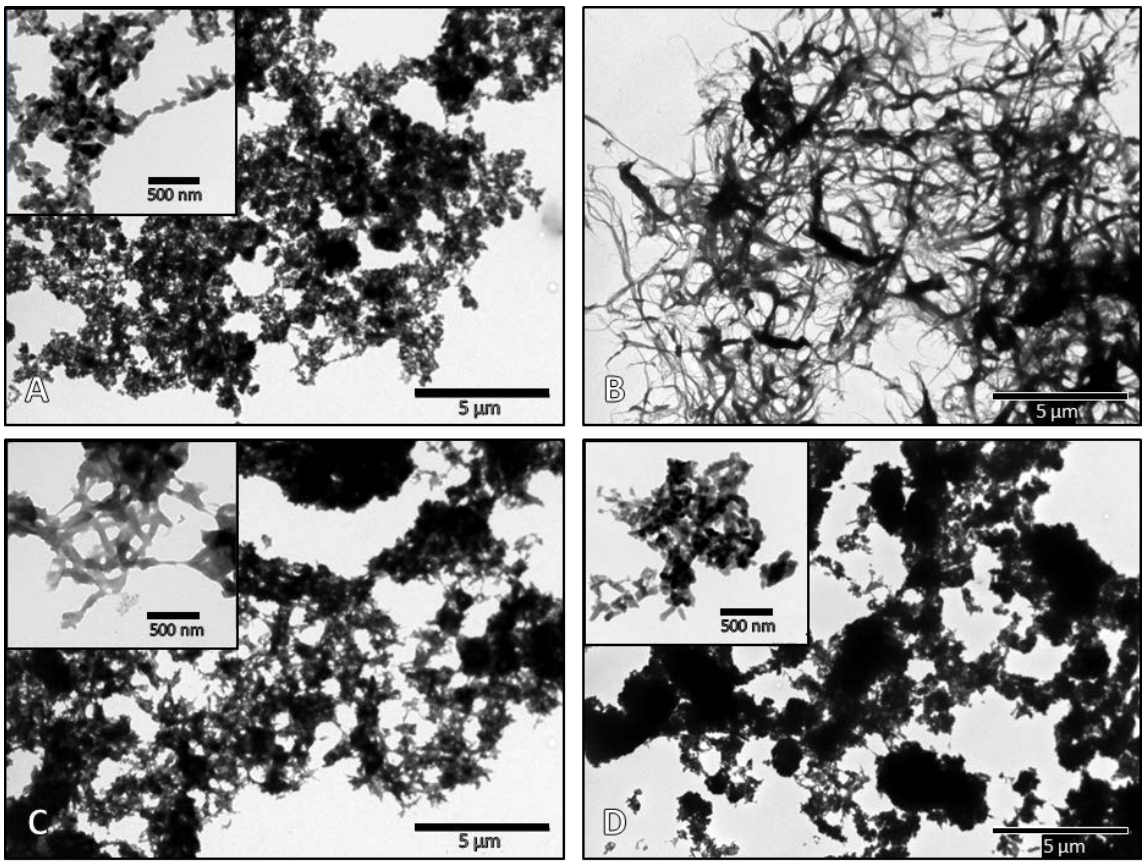

Figure 1. TEM images of the PANI samples showing their morphology: A) PANI-HCl (P1), B) PANI-DBSA direct synthesis (P2), C) PANI- DBSA indirect synthesis (P3) and D) PANI-NaSIPA (P4). The magnification is 6000x and the scale bar in the Figures is 5µm. The insets magnification is 50000x and the corresponding scale bar is 500 nm.

In summary, all these experimental conditions promote that the aniline nucleates become organized to form one-dimensional stacks stabilized by π-π interactions between phenazine-containing oligomers. Subsequently, polyaniline chains grow from the self-assembled nucleates leading to microfibrils. The growth of the microfibril is preferred over the start of new fibers [27].

In relation with redoped samples, both dedoping and redoping processes are influenced by the morphology of the pristine PANI-HCl. Not surprisingly, the morphology of P1 nanorods is hardly unaffected by the dedoping and redoping process in P4 (PANI-NaSIPA). By contrast, P3 (PANI-DBSA) shows intermediate morphology between P1 and P2 with longer, wider and more interconnected nanorods (**Figure 1C Inset**). The surfactant nature of DBSA explains the observed differences. PANI aggregates are covered by a DBSA rich surface layer, which consists on fully doped PANI-DBSA and free DBSA (core/shell structure). The excess DBSA acts as a plasticizer and covers the conductive outer layer [30].

3.2. Chemical composition by FTIR, elemental analysis and XPS

The alternative arrangement of quinoid and benzenoid rings in PANI (half oxidized/half reduced emeraldine base (EB)) plays a significant role towards the achievement of high conductivity, creating chance for polaron formation in the presence of protonic acid, which is responsible for the conduction (**Figure 2A**) [31]. Besides the oxidation state there are other factors which influence the conductivity of polyaniline such as the doping level and type of dopant, molecular weight, crystallinity and molecular arrangement [1].

3.2.1. FTIR

FTIR spectra of doped polyanilines and corresponding bases are depicted in **Figure 2B** in the range of 1800-500 cm^{-1} for the sake of clarity. The bands assigned to the quinoid (Q, $\nu_{C=N,\ C=C}$) and benzenoid (B, $\nu_{C=C}$) moieties are located at Q/B= 1561/1478 and 1564/1475 cm^{-1}, for P1 and P2, respectively. For both samples, the shoulder at ~1610 cm^{-1} is alloted to NH^+ deformations [32]. When PANI salts are treated with alkali, the Q and B modes upshift to 1591/1499 cm^{-1} for P1 base and to 1580/1493 cm^{-1} for P2 base while the shoulder at ~1610 cm^{-1} disappears. The new band at 1382 cm^{-1} for P1 base

and 1375 cm^{-1} for P2 base, is typical of a standard PANI base (ν_{C-N} in the proximity of a quinoid ring) [33,34].

The Q and B bands shift to 1559/1470 and 1561/1488 cm^{-1} upon redoping with DBSA (P3) and NaSIPA (P4), respectively. This implies that P3 is more protonated than P1 and P2 and that P4 is the least protonated sample [33].The intensity ratio of the Q/B absorption bands (I_Q/I_B) is indicative of the oxidation state of the polymer. A value of 1.0 defines the emeraldine type structure [21].The I_Q/I_B ratios are close to unity, indicating that PANI samples somewhat display an emeraldine form: 0.85 (P1), 0.78 (P2), 0.82 (P3) and 0.90 (P4). The oxidant concentration and the pH of the reaction medium are the key factors that influence oxidation [21]. The lower APS concentration used in the preparation of P2 compared to P1 may have favored the reduction state of polyaniline, whereas the different nature and/or concentration of the acids used for redoping explains the difference between P3 and P4.

The bands characteristics of the conducting protonated salt are observed at 1245 cm^{-1} (ν_{C-N+} in the polaron structure) and at 1145-52 cm^{-1} (combination of δ_{C-H}, $\delta_{Q=N^+-B/\ B-NH^+.-B}$). The latter is considered a measure of the degree of electron delocalization and is characteristic of PANI conductivity. It is shifted to 1166 cm^{-1} in the P1 base ($\delta_{C-H/N=Q=N}$) but no shift is detected in the P2 base [33]. The relative intensity of this peak compared to the ~1300 cm^{-1} band (ν_{C-N-C} of secondary aromatic amine) is considerably increased in the doped samples with respect to the emeraldine base.

The branching of PANI chains is an issue rarely mentioned that could negatively affect conductivity. The broad band at 825-830 cm^{-1} is related to aromatic C-H out-of-plane bending vibration (γ_{C-H}) on a 1,4-disubstituted aromatic rings. For branched PANI additional bands should be present at ~860 ($\gamma_{C-H1,2,4}$) and 760 ($\gamma_{C-H1,2}$) cm^{-1}. Since these bands have not been observed, dominating p-coupling is confirmed. Thus, it is assumed that the PANIs are mainly linear. From another point of view, the spectrum of P2 contains a band at 1404 cm^{-1}, which has been related to the ring stretching of the phenazine unit, formed by oxidative intramolecular cyclation of o-couple aniline units or oxidative insertion of the aniline molecule in to p-linked aniline [33,34].

Regarding the dopants, the characteristic absorptions of DBSA are observed for P2 and P3: the 2958, 2824 cm^{-1} and 2854 cm^{-1} bands ($\nu_{CH2asym,}$ $\nu_{CH2sym,}$) and the peaks 1042 and

1010 cm^{-1} ($\nu_{symO=S=O}$) [35,36]. For P4, the bands of NaSIPA are located at 1710 cm^{-1} ($\nu_{C=O}$), 1042 cm^{-1} ($\nu_{O=S=O}$), 760 cm^{-1} (1, 3, 5- trisubstituted benzene ring of the dopant) and 624 cm^{-1} (δ_{SO3}) [11].

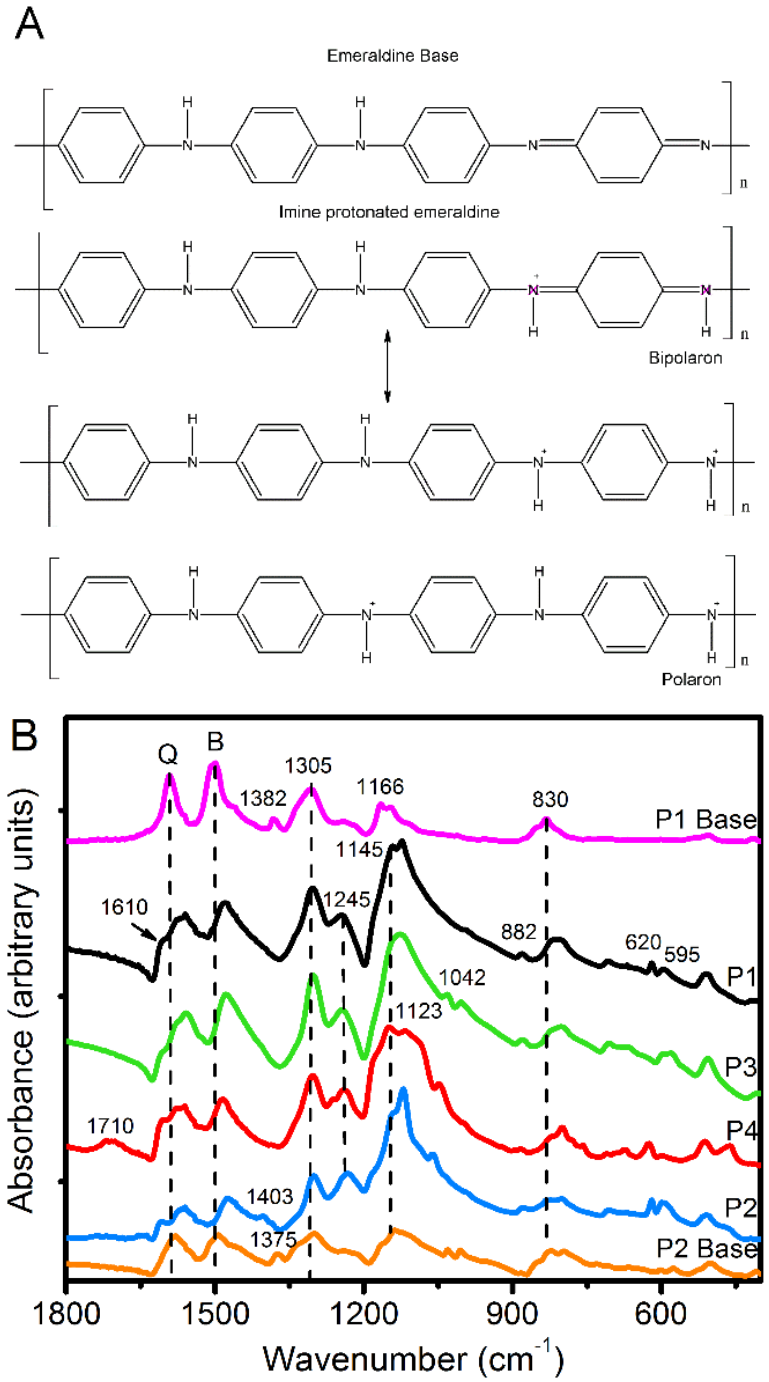

Figure 2. A) PANI emeraldine base (EB) and its different protonated forms. B) FTIR spectra of PANI bases and PANI salts: PANI-HCl (P1), PANI-DBSA direct synthesis (P2), PANI-DBSA indirect synthesis (P3) and PANI-NaSIPA (P4).

As a final point, the spectra of the four doped polyanilines show bands at 882, ~620 and 595 cm^{-1} which have been assigned to S-OH or S-O-C stretching and S-O bending

modes. The presence of HSO_4^-/HSO_3^- or SO_4^{-2} counterions in P1 is associated with the use of APS as oxidant and they can act as additional dopants [27,34].These counterions are completely removed by deprotonation of P1 with ammonium hydroxide (P1 Base).

3.2.2. Elemental Analysis and XPS

The chemical composition analyses of polyaniline samples are determined utilizing both elemental analysis (**Table S1**) and XPS analysis (**Table 2**).

The best way to calculate the protonation degree is to quantify the various nitrogen species from the curve fitted XPS N1s core level spectrum [37]. PANI samples have been deconvoluted to four and five peaks depending on the sample. The peaks at 398.5 eV and 399.7 eV are related to undoped imine and amine groups, respectively. The peaks with binding energies >400 eV are attributed to the positively charged nitrogens (N^+). The positively charged nitrogen contribution to the total nitrogen content ($-N^+/N$) is the doping level or protonation degree [38].

The doping level values are 0.57, 0.49, 0.60 and 0.38 for P1, P2, P3 and P4, respectively **Table 2**). These results are coherent with the Q and B band shifts observed in the FTIR. Besides, within experimental error, the $–N^+/N$ values are equivalent to the S/N bulk ratios for the three samples doped with organic sulfonic acids: 0.46, 0.62 and 0.30 for P2, P3 and P4, respectively (**Table S1**). Hence, the elemental analysis can be used to estimate the extent of doping when organic sulfonic acids are used as dopant [39].

Nevertheless, the S/N surface ratios (**Table 2**) for DBSA doped samples, P2 and P3, are higher than the corresponding bulk ratios. These facts imply that considerable amounts of free DBSA molecules are concentrated at the surface. The difference between the bulk and surface values in P3 is nearly twice the difference found for P2, due to both the synthesis and washing procedures. Regarding the synthesis, the amount of DBSA in relation with aniline employed in the synthesis of P3 is higher than in P2 (**Table 1**); concerning the washing step, water: acetone 1:1 is used in P2 whereas acetone is employed in P3. It has been proved that water is able to remove DBSA from the sample surface to a greater extent than acetone [37]. In relation with P4, the level of protonation and the sulphonation degrees obtained by elemental analysis and XPS are identical within experimental error, suggesting that all NaSIPA molecules act as counterions and that there is not free NaSIPA. These results confirm the formation of a

DBSA rich surface layer in P3 and explain the differences in morphology depicted in section 3.1 between P3 (interconnected nanorods) and P4 (nanorods).

From another point of view, the presence of sulfur in P1 supports the interpretation of the FTIR data which confirmed that P1 contains non-negligible amounts of HSO_4^-/HSO_3^- or SO_4^{-2} counterions due to the APS oxidant (S/N~0.17 on molar base at the bulk, **Table S1**, and 0.21 at the surface, **Table 2**). In agreement with the FTIR spectra, sulfur containing species are completely eliminated by neutralization with ammonium hydroxide (P1 base, **Table S1**).

Furthermore, the fraction of positively charged nitrogens in P1 is superior to the sum of the Cl/N and S/N contents. In order to find out the real contribution of the different dopants, the peaks due to chlorine Cl 2p (196.95 eV) and sulfur S 2p (167.46 eV) have been deconvoluted. The Cl 2p core level spectrum shows the presence of two doublets at 198.0 and 200.5 eV attributed to the chloride anion and covalent chlorine, respectively [40]. Likewise, the S 2p spectrum has been fit using two doublets at 168.8 and 170.25 eV. The doublet with lower binding energy is assigned to the sulfur of the sulfonate or sulfate group, which acts as a counter ion, and the doublet with the higher binding energy is from the sulfur in neutral sulfonic or sulfate acid [41]. Based on the precedent assignments, it is found that ~74.16% of Cl and ~67.23% of S present protonate the PANI. The remaining ~25.84% Cl and ~32.77% S are in neutral form. Combining with the total Cl and S the doping percentages convert to molar ratios, [Cl^-/N] and [HSO_4^-, HSO_3^- or SO_4^{-2}/N] (**Table 2**). The sum of the latter, equal to 0.28, is considerably less than the degree of protonation (-N^+/N= 0.57), implying that water plays an essential role in protonation. This observation is coherent with the weight loss at low temperature calculated by TGA in section 3.5. More to the point, the XPS Cl/N ratio of 0.19 is surprisingly low. The extremely low Cl/N ratio was already observed by other groups for PANI and attributed to the surface oxidation or to the purification method [42].

Similarly, the S2p spectra of P2 and P3 were fit using two doublets. The doublet with lower binding energy is assigned to the sulfur of the sulfonic group (SO_3^-, 168.0 eV) (Area% = 51 and 34.46, for P2 and P3, respectively) and the doublet at 168.85 eV allotted to the neutral –HSO_3 form (Area% = 49 and 65.55, for P2 and P3, respectively). Combining with the total sulfonation levels of **Table 2** convert to [SO_3^-/N] molar ratios,

0.36 and 0.37 for P2 and P3, respectively. In both cases, the $-N^+/N$ ratio exceeds the $[SO_3^-/N]$ ratio. This fact implies that water may also play a role in protonation. This outcome is consistent with the water loss at low temperature calculated for P2 by TGA analysis in section 3.5 but not with the water content of P3. Nevertheless, it must be born in mind that the XPS technique is sensitive to the very surface (~5 nm depths) and sometimes the results may not be reliable to obtain information of the bulk sample [42].

Table 2. XPS surface compositions (atomic percentage), doping levels and electrical conductivity of PANI salts.

Sample	N1s Core level spectrum			XPS Stoichiometric totals					σ (S/cm)
	=N-/N	NH/N	$-N^+/N$	S/N	Cl/N	C/N	SO_3^{-2}/N	Cl^-N	
P1	0.05	0.38	0.57	0.21	0.19	6.58	0.14	0.14	14.7±1.8
P2	0.06	0.45	0.49	0.71	-	16.15	0.36	-	7.7±1.1
P3	0	0.40	0.60	1.07	-	21.13	0.37	-	9.9±0.6
P4	0.07	0.55	0.38	0.33	-	8.32	-	-	3.9±0.3

3.3. X-ray diffraction studies

The crystallinity and orientation of conducting polymers have been of much interest because highly ordered systems can display metal-like conductive states [25]. The powder XRD patterns of the four polyaniline salts together with the emeraldine base (P1 base) are shown in **Figure S1**. The *d*-spacings, interchain separation, normalized intensity and crystallite size for the main peaks together with the degree of crystallinity are displayed in **Table 3.**

The two samples obtained by direct synthesis exhibit partial crystallinity although P2 has a higher degree of crystallinity than P1. Both samples show main reflection peaks at about 2θ ≈ 15, 20, and 25.5 and small peaks at 9.4, 27.6, and 29.7°. The peaks at ~20° and 25.5° belong to periodicity parallel and perpendicular to polymer chain, respectively [43,44]. As previously reported, these crystalline features can be indexed in a pseudo-orthorhombic cell and are indicative of partially crystalline emeraldine salt of ES-I form [25]. Dedoping of ES-I leads to the amorphous emeraldine base, EB-I, with a broad band at a 2θ value of ~ 19-20° [43].

Table 3. The *d*-spacing, relative intensity, interchain separation, crystallite size and degree of crystallinity (X_c) of the four PANI salts.

Sample	2θ (°)	I	d (x10^{-10}m)	R(x10^{-10}m)	L (x10^{-10}m)	X_c (%)
P1	9.38	0.005	9.42	11.80	-	29
	15.10	0.010	5.86	3.63	-	
	20.55	0.011	4.32	5.40	-	
	25.65	0.046	3.47	4.34	44	
P2	9.68	0.004	9.13	11.41	-	48
	14.97	0.026	5.91	2.36	-	
	19.95	0.032	4.45	5.56	-	
	25.30	0.069	3.52	4.40	86	
P3	2.70	0.028	32.30	40.4	54	14
	19.15	0.017	4.63	5.79	-	
	25.33	0.009	3.51	4.39	-	
P4	15.02	0.011	5.90	1.76	-	16
	19.95	0.014	4.45	5.57	-	
	25.15	0.025	3.54	4.43	49	

The amorphous base becomes slightly crystalline when redoped with DBSA (P3) and NaSIPA (P4). P3 exhibits a sharp peak at 2θ= 2.7° together with amorphous scattering centered at 2θ=19.2° and some weak features at ~25°. The wide angle peak at ~19.2° may be the superposition of the amorphous scattering and disordering of the polyaniline chains, whereas the peak at the low angle is a characteristic feature of an interlayer repeat [44]. P4 is isomorphous with respect to P1 and P2, with three broad Bragg peaks visible centered at 2θ ~ 15, 20 and 25.2 x10^{-10}m.

Except for P3, the highest relative intensity corresponds to the peak at 2θ~ 25.5 x10^{-10}m, increasing with the degree of crystallinity. The ranges of the interchain distances and crystalline domain sizes shown in **Table 3** are in agreement with values previously reported [23]. The *d*-spacings and interchain distances of P1 are smaller than the values calculated for P2, despite the greater crystallinity degree and crystallite size of the latter, probably due to the size of the dopant. The compact structure of P1, with the smallest π-π stacking distance, may favor the interchain hopping in the polyaniline and

consequently the charge carrier mobility [45,46]. P3 and P4 interchain distances are closer to P2 or slightly higher.

As stated before, contrary to P2, P3 forms a lamellar type structure consisting of PANI chains with irregular conformations and elongated alkyl tails of the DBSA, which function as spacers with some degree of interdigitation between parallel planes or sheets stacked by polymer backbones. This layered structure has been extensively described for DBSA-doped samples, especially for polymers prepared by indirect synthesis [44,47]. The layer to layer distance, which can be determined from the smaller diffraction angle at 2.7 $x10^{-10}$m (d= 32.3 $x10^{-10}$m), is proportional to the size of the spacers and influenced by the doping level. The domain size of the layered structure regions, estimated from the width of the small angle peak, is 54 $x10^{-10}$m. The anisotropic orientation of the dopant alkyl chains can not only promote interchain diffusion of carriers but also optimize transportation within individual layer [44].

3.4. Thermal behavior

Figure 3 displays the thermal behavior of doped PANIs evaluated by Thermogravimetric analysis (TGA). The four PANI salts show weight losses at low temperature, due to solvent evaporation and release of volatile components. Directly doped polyanilines samples, P1 and P2, exhibit water contents around 10%, whereas redoped PANIs have lower water contents, 2.6 and 5% for P3 and P4, respectively. The electrical conductivity of polyaniline with water content between 10-20% may be affected by the moisture removal on heating [48].

Concerning P1 degradation, there are three steps in the thermogram of **Figure 3** while the P1 base has only two steps (not shown). The second step, which is related to the loss of HCl acting as dopant and probably to HSO_4^- / HSO_3^- or SO_4^{-2} counterions produced from APS (minimum of the second weight loss in the first derivative thermogram ~245°C), is absent in the degradation curve of the emeraldine base [49]. The third step, identified above 320 °C, is attributed to the actual decomposition of polyaniline. The first derivative plot of P1 shows a shoulder around 410 °C. It has been ascribed to the loss of bound HCl from deep inside the bulk of the polymer clusters, followed by degradation of the polymer chains at higher temperatures, as it is missing in the corresponding first derivate plot of the P1 base [31].

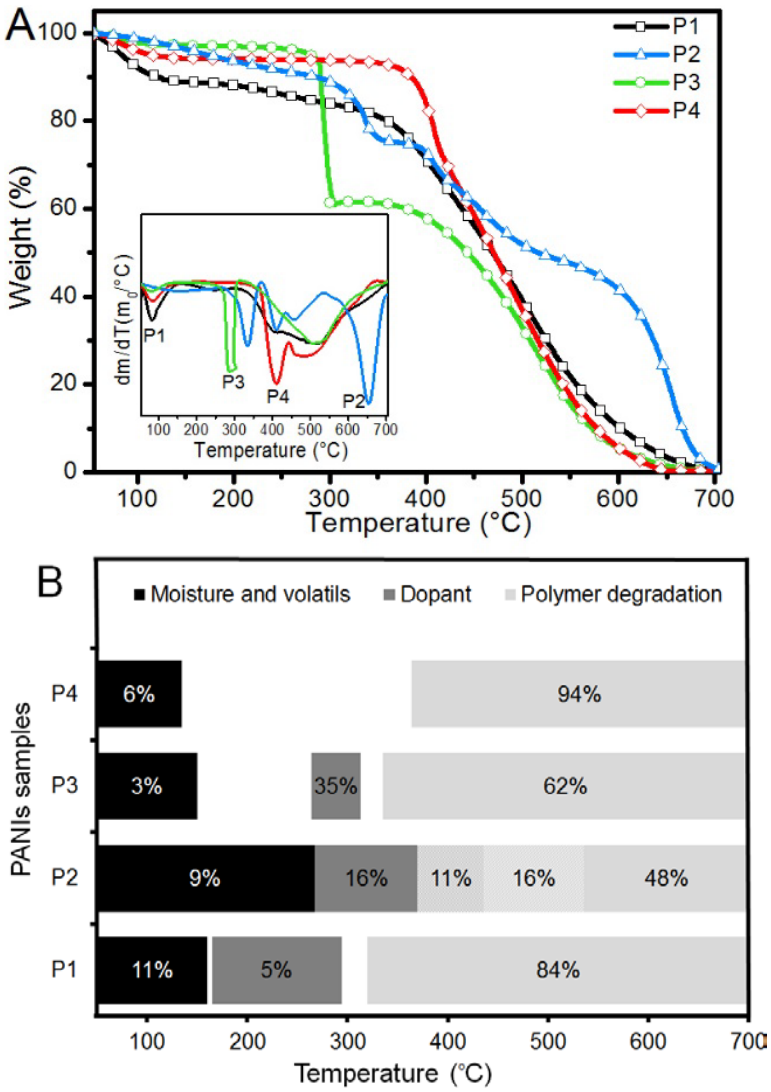

Figure 3. TGA and DTG curves (A) and temperature intervals with corresponding weight losses for the different degradation events (B) of PANI-HCl (P1), PANI-DBSA direct synthesis (P2), PANI-DBSA indirect synthesis (P3) and PANI-NaSIPA(P4) samples from 35 to 700 °C at 10 °C/ min under oxygen atmosphere.

Likewise, the thermogram and derivative curve of P2 have been compared with the corresponding base (not shown). After the usual loss of solvent and volatiles, the dopant degradation occurs (second step). A 6% weight loss is also detected in this range for the P2 base, confirming the presence of a small amount of DBSA, previously observed by FTIR. Within the third step, two stages are observed in both P2 and P2 base. The one spanning from 370 to 536 °C shows two unresolved peaks in the first derivate plot. They have been tentatively related with oxidation reactions, as they have not been observed under nitrogen atmosphere [34], and/or possible oligomers degradation, owing to the presence of phenazine-containing aniline oligomers

detected by FTIR spectroscopy. Finally, the heavy weight loss over 537°C is ascribed to the breaking down of the polymer backbone.

In relation to P3, the significant weight loss in the second step is attributed to the evaporation and degradation of the dopant. Above 400°C, the polymer degradation occurs. The minimum of the second weight loss in the first derivative thermogram is significantly shifted to lower temperature with respect to P2 (335 and 287 °C for P2 and P3, respectively, **Fig. 3A inset**) and the weight loss is increased (**Fig. 3B**). The lower degree of crystallinity of P3 explains the decreased thermal stability in the second temperature range. It would need more energy for the dopant to be removed if the PANI chains are well arranged in a crystalline structure like in P2 [50].

Regarding P4, the first weight loss is due to bound and free water, whereas the weight loss over 371 °C involves the degradation of both NaSIPA dopant and the polymer (the derivative weight curve shows two unresolved minima at 410 and 490 °C, respectively). P4 has higher thermal stability than the two PANI-DBSA despite the lower degree of crystallinity compared with P2, owing to the superior thermal stability of the dopant [9]. DBSA decomposes about 250 °C [48] whereas the degradation of NaSIPA starts around 440 °C [9].

3.5. Thermal stability of DC conductivity

The room temperature conductivity of the four doped-PANI samples has been measured by the four-point probe technique (**Table 2**). As expected, the largest electrical conductivity at room temperature corresponds to P1 (σ = 14.7 S/cm) whereas P2 exhibits approximately half this value (σ = 7.7 S/cm). In addition to the inorganic nature of the dopant, the greater oxidation state, higher doping level and inferior π-π stacking distance between polyaniline chains, account for the superior conductivity of P1 with respect to P2 despite the lower degree of crystallinity of the former. Moreover, the presence of phenazine containing oligomers in P2 negatively affects the electrical conductivity, as they do not contain any extended conjugated system of double bonds, although they may simultaneously favor the chain alignment.

In relation with P3, the dedoping-redoping approach together with a molar aniline: DBSA ratio (1: 5.6) higher than P2 (1: 3), gives a polyaniline with intermediate properties between P1 and P2. The electrical conductivity of P3 (σ = 9.9 S/cm) is improved with respect to P2 due to the superior oxidation state and doping level,

absence of oligomers and to the formation of a layered structure. It has been stated that the improvement of electric properties are assisted by the formation of the layered structures [44].

On the other hand, P4 shows the lowest conductivity of the four samples (σ = 3.9 S/cm). This value, lies between the conductivities obtained by Saini et al. [9] for directly and indirectly NaSIPA-doped PANIs. Despite the fact that P4 has the same nanorod morphology than P1 and the oxidation state of the emeraldine structure, the low conductivity is mainly ascribed to the small doping level and the low crystallinity without layered structure.

Furthermore, for the three samples doped with organic sulfonic acids the doping levels ($-N^+/N$) values are equivalent to the S/N bulk ratios and the conductivities at room temperature are proportional to the doping levels (R^2= 0.95).

From another point of view, the thermal stability of the electrical conductivity strongly depends on moisture content, the chemical nature of the dopants and the crystal structure. **Figure 4A** shows that P2 relative conductivity remains practically constant upon heating from 25 to 200 °C at 2 °C/min, whereas P1 conductivity sharply decreases after 50 °C, followed by P4 and the gradual loss of P3.

Many studies have reported that organic acid doped polyanilines exhibit better conductivity retention compared to inorganic acid doped ones. For dopants with low molecular weight, such as HCl, the conductivity is lost even at temperatures as low as 50°C due to loss of moisture and dopant. Chlorine counterions and water can be easily extracted and evaporated from the polymer and dedoping destroys the crystal structure, leading to the amorphous non-conductive emeraldine base [48,51,52]. The crucial role of water in the protonation of P1 has been proved by XPS and TGA analysis.

In contrast, large size organic dopants such as DBSA or NASIPA are not easily removed from the polymer matrix below 250 °C, as described in the TGA analysis. Therefore, the dopant evaporation and degradation is not the main cause of the large reduction of the electrical conductivity of the P3 and P4 samples below 200 °C at 2 °C/min (**Figure 4A**). Besides, the moisture contents of these samples are lower than that of P2. To check the chemical changes of P3 and P4 due to the heating process, the FTIR spectra before and after heat treatment up to 230 °C have been compared (not shown). The

DBSA, NaSIPA and PANI characteristics bands remain unchanged. The only differences detected are a small decrease in the Q/B peak intensity ratio and the shift of the Q and B ring stretching bands to higher wavenumbers. These facts suggest that cross-linking reactions may have taken place and some of the acids have been transformed back to the undoped forms, respectively [34,46,51].

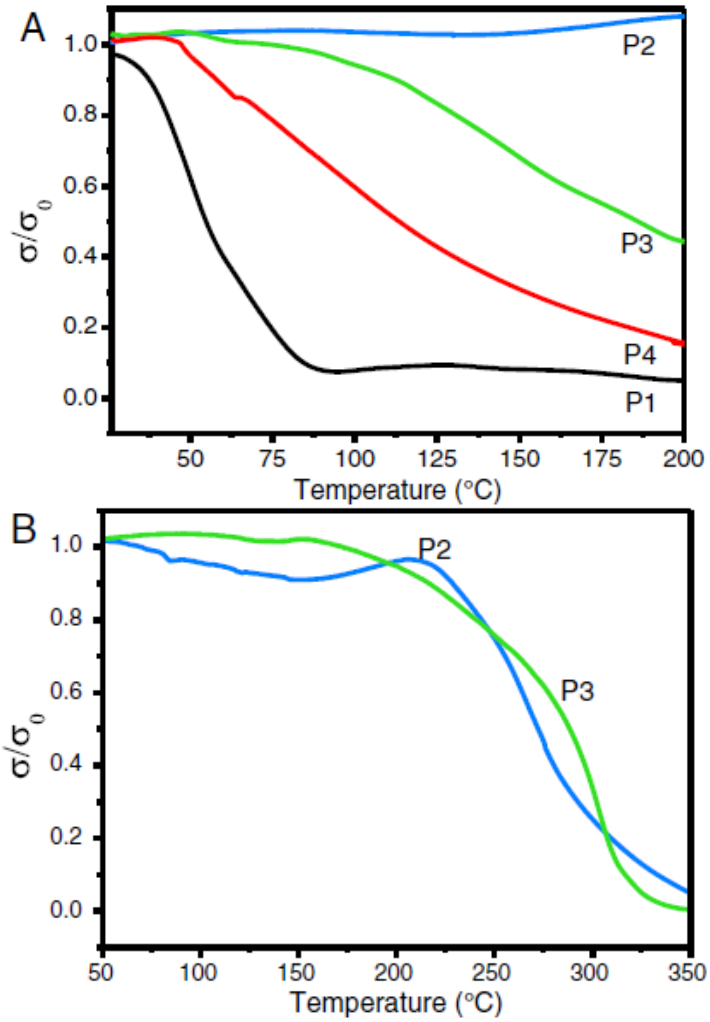

Figure 4. DC conductivity behavior as a function of temperature: A) from 25 to 200 °C at 2°C/min for PANI-HCl (P1), PANI-DBSA direct synthesis (P2), PANI-DBSA indirect synthesis (P3) and PANI-NaSIPA (P4) samples. B) from 50 to 350 °C at 10°C/min for P2 and P3 samples.

A noteworthy point is the difference in the thermal stability of conductivity between the two DBSA doped polyanilines, P2 and P3, which is probably due to structural differences, reflected by dissimilar morphologies, X-ray diffraction patterns and TGA profiles. The experimental conditions of direct emulsion polymerization promotes crystallinity and microfibrillar morphology [53]. The higher degree of crystallinity of P2 compared to P3 favors thermal stability as the aging process first affects the most disordered regions between the crystallites [12]. By contrast, the indirect approach

achieves doping by introducing the DBSA (solved in acetone) into the solid, non-conducting amorphous emeraldine base, leading to low PANI crystallinity with a layered structure. It should be kept in mind that the real structure of this doped PANI is rather distorted and should better be considered in terms of a liquid –like short range order [54].

Moreover, the thermal stability of P3 conductivity significantly improves up to 150 °C at a heating rate of 10 °C/min. This behavior has not been observed for P4 (not shown), which also has low crystallinity but no layered structure nor a surface shell of free dopant. From another point of view, in these conditions, P3 conductivity is less affected by moisture removal than P2 conductivity in agreement with the TGA results (**Figure 3B**).

Anyway, direct and indirect synthesis using DBSA lead to samples with large thermal stability of the electrical conductivity. Due to the poor conductivity retention with temperature observed for P1 and P4, these samples cannot be considered for thermal sensor applications.

Cyclic ageing studies have been further performed with P2 and P3. The results of four heating/cooling cycles from 30 to 70°C at 5 °C/minute are depicted in **Figure 5**. The amplitude of the electrical response of P2 is twice the value of P3 ($(\Delta\sigma/\sigma_0)/\Delta T$ are ~0.02 and ~0.01 for P2 and P3, respectively). Both materials exhibit good repeatability although a small loss in the relative conductivity of P2 is observed at the end of the fourth cycle of 2.79%, the sharpest drop occurring in the first two cyles. This trend may be explained by the release of moisture or volatile components [14]. Regarding P3, there is a negligible increase in the relative conductivity of 0.31% at the end of the experiment.

More to the point, P2 and P3 exhibit reverse behavior in each cycle. P2 increases the electrical conductivity with temperature (and vice-versa), while P3 shows a decrease in electrical conductivity with increasing temperature. The conductivity variation of P2 may be explained by the thermal doping concept (**Figure 5A**). Owing to the presence of free DBSA molecules entangled at the surface, with the increase in temperature more DBSA can be doped into polyaniline by thermally enhanced mobility [12,47,48].

The thermoreversibility of P3 (**Figure 5B**) is believed to be due to the lamellar type structure under the doped condition. Upon heating until 70°, the ionic bonds between the PANI iminic nitrogens and DBSA sulfonic groups break down which together with the disruption of the extended tails of the dopant mesomorphic structure leads to reduction of electrical conductivity; on cooling, the ionic bonds and the layered structure can be formed again and eventually the original conductivity is restored [55].

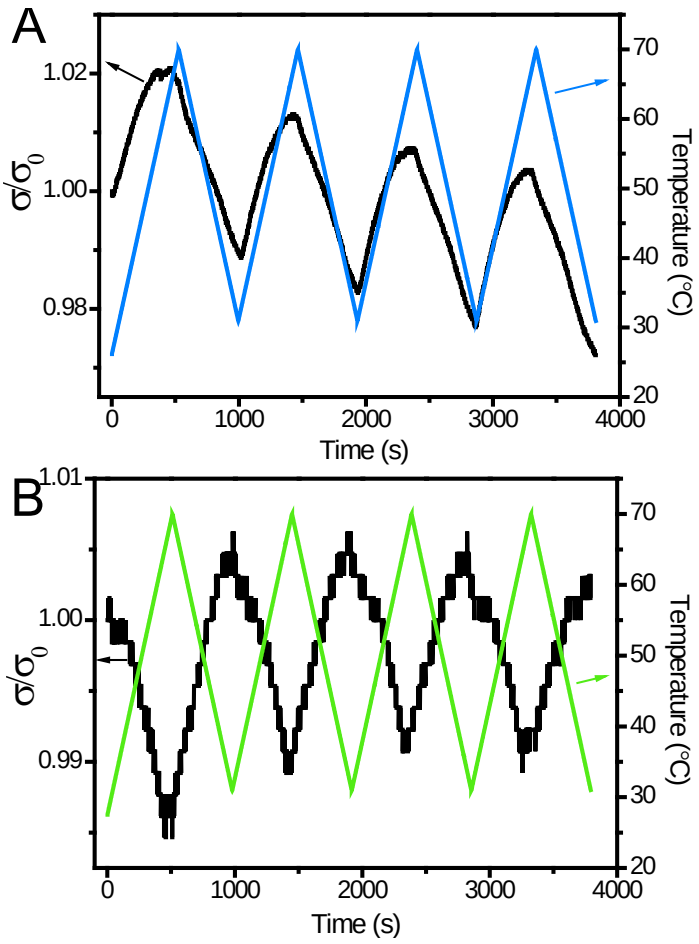

Figure 5. Cyclic temperature dependence of the DC electrical conductivity between 30 to 70 °C for A) PANI-DBSA direct synthesis (P2) and B) PANI-DBSA indirect synthesis (P3).

4. Conclusions

In the current study, simple, low-cost synthesis methods, scalable to industrial volumes, are presented in order to obtain PANIs suitable for use in electronic applications. Initially four doped polyanilines samples have been prepared by chemical oxidative polymerization using two different routes including direct doping with HCl and DBSA and a dedoping-redoping approach with DBSA and NaSIPA.

The different routes of synthesis and experimental conditions lead to dissimilar morphology, structural order, oxidation state, doping level and thermal degradation profiles, which help to explain the conductivity values and the thermal stability of conductivity.

PANI-DBSA obtained by direct synthesis exhibits microfibrillar morphology and the highest crystalline level, although, the presence of phenazine oligomers may be responsible for the electrical conductivity value, which is lower than expected. All other polyanilines are nanorod shaped and have poor structural order.

As expected, PANI-HCl shows the highest electrical conductivity at room temperature but the worst conductivity retention in thermal assays. PANI-NaSIPA displays the smallest doping level plus low crystallinity, hence, the lowest conductivity of all. On the contrary, despite the low crystallinity level of PANI-DBSA obtained by the indirect method, the layered structured, observed in X-ray difractograms, together with its high doping level explain its high electrical conductivity. Besides, the indirect route of synthesis has the advantage of avoiding the use of chloroform (less eco-friendly).

Owing to superior conductivity retention with temperature, the two PANI-DBSA doped samples have been chosen for cyclic ageing studies. They both exhibit excellent electrical linearity and reversibility after 4 heating-cooling cycles up to 70 °C. Regarding thermal sensitivity, the amplitude of the electrical response of PANI-DBSA prepared by direct synthesis is twice the value of PANI-DBSA obtained by the indirect route. In relation with repeatability, the former exhibits a small drop in relative conductivity (2.79%) at the end of the fourth cycle, assigned to its greater moisture content, whereas the latter displays a slight increase of 0.31%.

In summary, both kinds of DBSA doped polyanilines, which can be prepared by feasible routes for large-scale production, show potential for temperature sensor applications.

Supplementary material

Table S1. Chemical compositions of PANI salts and base powders obtained by Elemental Analysis. S/N and C/N ratios are given on molar base.

Sample	% N	% C	% H	% S	S/N	C/N
P1Base	14.1±0.3	73.8±1.3	4.8±0.2	< 0.1	-	6.1±0.04
P1	10.1±0.6	52.7±3.8	4.7±0.3	4.8±0.7	0.17±0.04	6.1±0.1
P2 Base	9.6± 0.2	65.8±1.5	6.3±0.2	4.2±0.3	0.19±0.02	8.0±0.3
P2	7.0±0.9	58.7±6	6.2±0.6	7.4±0.54	0.46±0.03	10.0±2.0
P3	4.8±0.1	63.9±0.4	7.1±0.1	6.9±0.5	0.62±0.03	15.4±0.4
P4	7.5±0.9	55.1±2.5	3.9±0.1	5.0±0.7	0.30±0.08	8.7±0.7

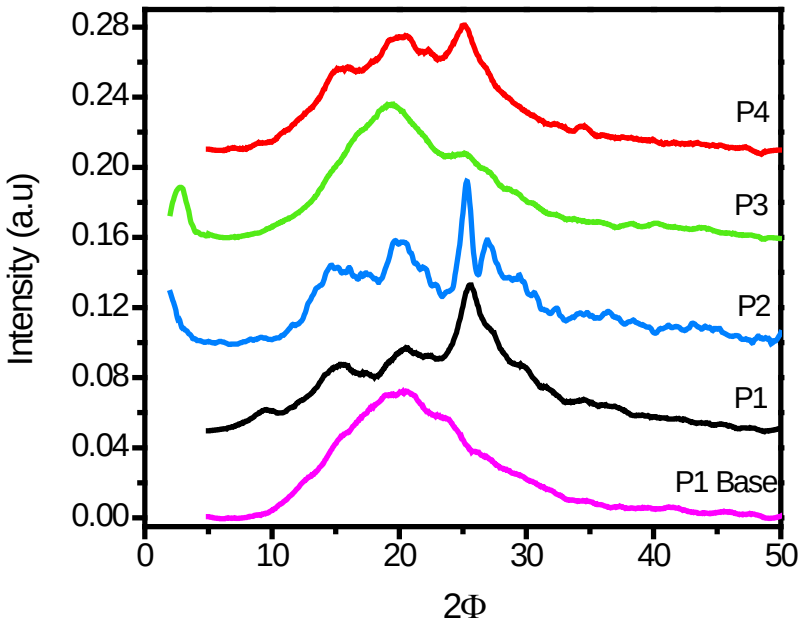

Figure S1. Normalized X-ray diffraction patterns for the polyaniline emeraldine base (P1 Base) and its different protonated forms: PANI-HCl (P1), PANI-DBSA direct synthesis (P2), PANI-DBSA indirect synthesis (P3) and PANI-NaSIPA (P4).

References

1. Bhadra, S., Khastgir, D., Singha, N. K. & Lee, J. H. *Progress in Polymer Science*, 34, (2009), 783.

2. Su, N. *Nanoscale Research Letters*, 10, (2015), 1.

3. Cheng, F., Tang, W., Li, C., Chen, J., Liu, H., Shen, P. & Dou, S. *Chemistry – A European Journal*, 12, (2006), 3082.

4. Huang, J. & Kaner, R. B. *Nat Mater*, 3, (2004), 783.

5. Yao, B., Wang, G., Ye, J. & Li, X. *Materials Letters*, 62, (2008), 1775.

6. Chang, M.-Y., Wu, C.-S., Chen, Y.-F., Hsieh, B.-Z., Huang, W.-Y., Ho, K.-S., Hsieh, T.-H. & Han, Y.-K. *Organic Electronics*, 9, (2008), 1136.

7. Fratoddi, I., Venditti, I., Cametti, C. & Russo, M. V. *Sensors and Actuators B: Chemical*, 220, (2015), 534.

8. Chartuprayoon, N., Zhang, M., Bosze, W., Choa, Y.-H. & Myung, N. V. *Biosensors and Bioelectronics*, 63, (2015), 432.

9. Huang, J., Virji, S., Weiller, B. H. & Kaner, R. B. *Chemistry – A European Journal*, 10, (2004), 1314.

10. Falletta, E., Costa, P., Della Pina, C. & Lanceros-Mendez, S. *Sensors and Actuators A: Physical*, 220, (2014), 13.

11. Saini, P., Jalan, R. & Dhawan, S. K. *Journal of Applied Polymer Science*, 108, (2008), 1437.

12. Golsanamlou, Z., Tagani, M. B. & Soleimani, H. R. *Physical Chemistry Chemical Physics*, 17, (2015), 13466.

13. Bhadra, S. & Khastgir, D. *Polymer Degradation and Stability*, 93, (2008), 1094.

14. Chen, T., Dong, C., Li, X. & Gao, J. *Polymer Degradation and Stability*, 94, (2009), 1788.

15. ALOthman, Z. A., Alam, M. M., Naushad, M. & Bushra, R. *Int. J. Electrochem. Sci*, 10, (2015), 2663.

16. Anwer, T., Ansari, M. O. & Mohammad, F. *Journal of Industrial and Engineering Chemistry*, 19, (2013), 1653.

17. Duran, N. G., Karakışla, M., Aksu, L. & Saçak, M. *Materials Chemistry and Physics*, 118, (2009), 93.

18. Jaymand, M. *Progress in Polymer Science*, 38, (2013), 1287.

19. Li, X., Wang, Y., Yang, X., Chen, J., Fu, H., Cheng, T. & Wang, Y. *TrAC Trends in Analytical Chemistry*, 39, (2012), 163.

20. Araújo, O. A. & De Paoli, M.-A. *Synthetic Metals*, 159, (2009), 1968.

21. Abdiryim, T., Xiao-Gang, Z. & Jamal, R. *Materials Chemistry and Physics*, 90, (2005), 367.

22. Park, H.-W., Kim, T., Huh, J., Kang, M., Lee, J. E. & Yoon, H. *ACS Nano*, 6, (2012), 7624.

23. Dopico-García, M. S., Ares, A., Lasagabáster-Latorre, A., García, X., Arboleda, L. & Abad, M. J. *Synthetic Metals*, 189, (2014), 193.

24. Wojdyr, M. *Journal of Applied Crystallography*, 43, (2010), 1126.

25. Pouget, J. P., Jozefowicz, M. E., Epstein, A. J., Tang, X. & MacDiarmid, A. G. *Macromolecules*, 24, (1991), 779.

26. Du, X., Xu, Y., Xiong, L., Bai, Y., Zhu, J. & Mao, S. *Journal of Applied Polymer Science*, 131, (2014).

27. Stejskal, J., Sapurina, I. & Trchová, M. *Progress in Polymer Science*, 35, (2010), 1420.

28. Chiou, N. R. & Epstein, A. J. *Advanced Materials*, 17, (2005), 1679.

29. Palaniappan, S. & John, A. *Progress in Polymer Science*, 33, (2008), 732.

30. Titelman, G. I., Siegmann, A., Narkis, M. & Wei, Y. *Journal of Applied Polymer Science*, 69, (1998), 2205.

31. MacDiarmid, A. G. *Angewandte Chemie International Edition*, 40, (2001), 2581.

32. Nand, A. V., Ray, S., Gizdavic-Nikolaidis, M., Travas-Sejdic, J. & Kilmartin, P. A. *Polymer Degradation and Stability*, 96, (2011), 2159.

33. Trchová, M., Šeděnková, I., Tobolková, E. & Stejskal, J. *Polymer Degradation and Stability*, 86, (2004), 179.

34. Trchová, M. & Stejskal, J. *Pure and Applied Chemistry*, 83, (2011), 1803.

35. Lu, X., Ng, H. Y., Xu, J. & He, C. *Synthetic Metals*, 128, (2002), 167.

36. Costa, L. C., Rubinger, C. P. L. & Martins, C. R. *Synthetic Metals*, 157, (2007), 945.

37. Barra, G. M., Leyva, M. E., Gorelova, M. M., Soares, B. G. & Sens, M. *Journal of applied polymer science*, 80, (2001), 556.

38. Neoh, K., Kang, E. & Tan, K. *The Journal of Physical Chemistry*, 96, (1992), 6777.

39. Jayamurgan, P., Ponnuswamy, V., Ashokan, S. & Mahalingam, T. *Iranian Polymer Journal*, 22, (2013), 219.

40. Tan, K., Tan, B., Kang, E. & Neoh, K. *Physical Review B*, 39, (1989), 8070.

41. Wei, X.-L., Fahlman, M. & Epstein, A. *Macromolecules*, 32, (1999), 3114.

42. Kohut-Svelko, N., Reynaud, S. & François, J. *Synthetic Metals*, 150, (2005), 107.

43. Hopkins, A. R., Lipeles, R. A. & Hwang, S.-J. *Synthetic Metals*, 158, (2008), 594.

44. Bandgar, D., Khuspe, G., Pawar, R., Lee, C. & Patil, V. *Applied Nanoscience*, 4, (2014), 27.

45. Zheng, W.-Y., Levon, K., Taka, T., Laakso, J. & Osterholm, J. *Polymer journal*, 28, (1996), 412.

46. Hwang, S., Potscavage, W. J., Nakamichi, R. & Adachi, C. *Organic Electronics*, 31, (2016), 31.

47. Bhadra, S., Singha, N. K. & Khastgir, D. *Polymer International*, 56, (2007), 919.

48. Levon, K., Ho, K. H., Zheng, W. Y., Laakso, J., Kärnä, T., Taka, T. & Österholm, J. E. *Polymer*, 36, (1995), 2733.

49. Kim, S., Ko, J. M. & Chung, I. J. *Polymers for Advanced Technologies*, 7, (1996), 599.

50. Wei, X. L., Wang, Y. Z., Long, S. M., Bobeczko, C. & Epstein, A. J. *Journal of the American Chemical Society*, 118, (1996), 2545.

51. Zhang, X., Zhu, J., Haldolaarachchige, N., Ryu, J., Young, D. P., Wei, S. & Guo, Z. *Polymer*, 53, (2012), 2109.

52. Sobha, A. & Narayanankutty, S. K. *International Journal of Nanoparticles*, 7, (2014), 112.

53. Ren, G., Qiu, H., Wu, Q., Li, H., Fan, H. & Fang, C. *Materials Chemistry and Physics*, 120, (2010), 127.

54. Yang, C. Y., Smith, P., Heeger, A. J., Cao, Y. & Osterholm, J. E. *Polymer*, 35, (1994), 1142.

55. Wernet, W., Monkenbusch, M. & Wegner, G. *Die Makromolekulare Chemie, Rapid Communications*, 5, (1984), 157.

56. Jana, T. & Nandi, A. K. *Langmuir*, 16, (2000), 3141.

CAPÍTULO 4:

Thermoelectric properties and intrinsic conduction processes in DBSA and NaSIPA doped polyanilines

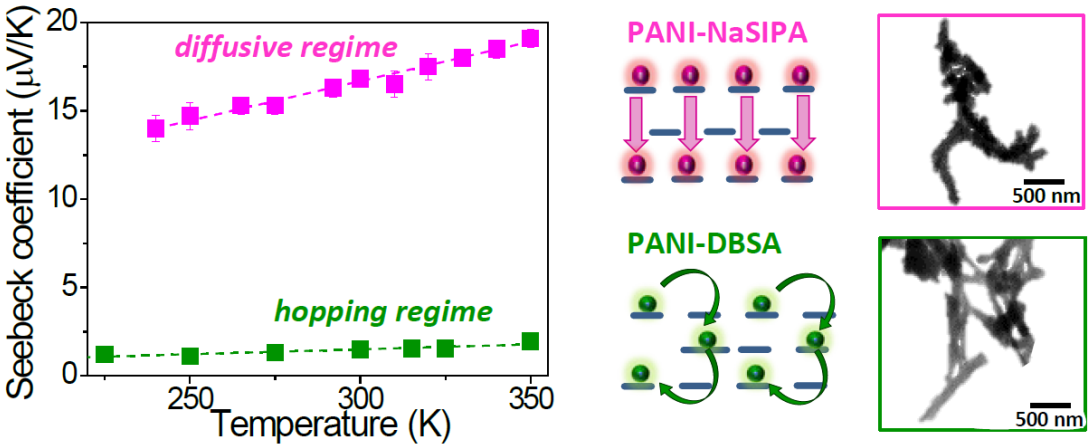

Basado en el artículo:

Horta-Romarís, L., González-Rodríguez, M. V., Lasagabáster, A., Rivadulla, F. & Abad, M.-J. *Synthetic Metals* 243**,** (2018), 44.

1. Introduction

The organic thermoelectric (TE) materials, as intrinsically conducting polymers (ICPs), are interesting candidates for green thermoelectric energy conversion applications, given their low cost and environmental safety [1-3]. The energy–conversion efficiency of a TE device is a function of the material's figure-of merit (ZT), average working temperature of the device and temperature difference between the hot and cold ends [4]. ZT is directly proportional to the electrical conductivity (σ) and the Seebeck coefficient (α) and inversely proportional to the thermal conductivity (κ) [1,2,4-6].

$$ZT = \frac{\sigma\alpha^2}{\kappa}T \qquad \textbf{(1)}$$

Thus, a good thermoelectrical material should have high σ and α, but poor κ. The three thermoelectrical parameters are interdependent in bulk materials and decoupling these parameters is definitely non-trivial [7].

Polyaniline (PANI) as one of the important ICPs has caused a lot of scientists' interests due to high stability, facile synthesis and tunable electronic properties [8]. Electrical conductivity of PANI increases with doping, which may be achieved by an acid-base reaction. As a result of the protonation of the nitrogen sites in the emeraldine base (EB), the cation radical of one nitrogen acts as a polaronic hole and these holes are charge carriers (p-type doped PANI) [9] (**Figure 1**). Electrical conductivity occurs via inter-polaron hopping along and across polymer chains [10,11]. Therefore, the carrier density depends on the degree of protonation or doping level [4,12]. Furthermore, in most cases PANIs appear to be amorphous, sometimes with some degree of crystallinity, thus heterogeneous conduction is set up involving "islands" of higher conductivity regions separated by lower conductivity regions. The polaron structures are responsible for electrical conduction through the hopping mechanism in the crystalline region [9], while intergrain resonance tunnelling occurs through the strongly localized states in the amorphous media [13]. These systems are featured with low charge carrier mobility and low electrical conductivities, even at high carrier densities [14,15]. This mixture of metallic and non-metallic behaviour is a key characteristic of all ICPs, including PANI [16].

By contrast, the Seebeck coefficient is more complex and difficult to predict. The reduction of the total number of charge carriers increase the Seebeck coefficient while lowering the electrical conductivity, but because the power factor (PF) scales with α^2, a net increase in the PF can be achieved for certain doping ranges. The identification of conditions conducive to decouple σ and α, remains challenging [7].

In this context, the control of morphology to obtain nanostructured polymers has proved to be a successful strategy to improve the TE properties of ICPs. Previous works have shown that polyanilines synthesized with nanorod or nanofiber morphology have lower electrical resistance than those synthesized with micrometric size [17-19]. This nanostructuring strategy can increase the Seebeck coefficient, due to improved charge carrier mobility, and also reduce the thermal conductivity [8,17], resulting in an enhanced ZT.

Specifically, in a preliminary study, we have introduced an ecofriendly and scalable indirect synthetic route (dedoping-redoping) [18], leading to organic doped PANIs with nanostructured morphology using either dodecylbenzensulfonic acid (DBSA) or 5-sulfoisophtalic acid sodium salt (NaSIPA) as dopants. Both bulky organosulfonic acids maintained a reasonable balance between conductivity, thermal stability and processability which are essential properties for widening industrial applications. In addition, the different chemical structures between the two dopants (rigid NaSIPA in contrast with the long alkyl flexible chains of DBSA, which in addition acts as a plasticizer) led to PANI salts with morphological and structural differences that are considered a good starting point to ascertain structure-properties relations. Since tuning the degree of doping and morphology are crucial for the optimization of thermoelectric performance of ICPs [7], the present work systematically studies the influence of the doping agent and molar acid concentration on the structure, physicochemical and TE properties of PANI-DBSA and PANI-NaSIPA, and seek to shed light on the conduction mechanisms. To the best of our knowledge, there are few studies concerning the TE performance of PANI DBSA [2] and none of PANI NaSIPA. To the best of our knowledge, no research on the TE properties of the latter has been previously reported. The different nature and doping ability of the two organosulfonic acids lead to dissimilar ZT trends with molar acid concentration and different conduction mechanisms.

2. Experimental

2.1. Materials synthesis

Aniline and dodecylbenzensulfonic acid (DBSA) 70 wt.% solution in 2-propanol were purchased from Sigma-Aldrich. The 5-sulfoisophtalic acid sodium salt (NaSIPA) 95 wt% was obtained from Alfa Aesar. The potassium peroxodisulfate (APS) and acetone was obtained from Scharlau.

Two PANI samples were synthesized by indirect route involving "dedoping-redoping" steps with two organic sulfonic dopants, DBSA and NaSIPA (**Figure 1**) [20]. PANI-HCl, prepared as described by Park et al. [21], was dedoped with 1M NH_3 for 2 h in ultrasonic bath, filtered under vacuum and washed with water until neutral pH. The resultant PANI-base was redoped with increasing molar concentrations of DBSA in acetone or NaSIPA aqueous solutions during 2h in ultrasonic bath. The samples were washed with large volumes of acetone to remove excess free acids [20]. Finally, the products were filtered under vacuum and freeze-dried.

The molecular weight of PANI base is determined from its intrinsic viscosity [η], according to the Mark-Houwink-Sakurada equation:

$$[\eta] = K.M_{\eta}^{\alpha} \quad \textbf{(2)}$$

where K and α are constants for a particular polymer–solvent pair at a particular temperature. Poly(p-phenylene terephthalamide) has a rigid chain with conjugated double bonds similar to PANI. Therefore, in a first approximation the values of K = 1.95×10^{-6} and α= 1.36, characteristic of this polymer in H_2SO_4 medium, were used for PANI [22]. The estimated molecular weight of the PANI base is 6,300 Da (R^2 = 0.97).

2.2. Characterization

The elemental analysis of C, H, N, and S was conducted using ThermoFinnigan FlashEA1112 elemental analyzer.

Fourier transformed infrared (FTIR) spectra of the polymers in KBr pellets were recorded on a Jasco 4700 spectrometer. The spectra were collected from 4000 to 400 cm^{-1}, with a 4 cm^{-1} resolution over 100 scans.

X-ray patterns of PANI powders were recorded in step-scan mode from 2º to 50º with a 2θ step of 0.05º using a D5000 diffractometer (XRD, Siemens- Bruker) with CuKα line irradiation (λ= 1.541Å). 40-point smoothing protocol using a Savitzky-Golay filter has

been applied to the diffractograms, which were normalized to area 1 (Origin 8.0 graphical software). A split Gaussian function was used to subtract the background and amorphous contributions using the open-source software Fityk. The difference patterns were deconvoluted into the crystalline constituents using Gaussian function peak shape approximation [23] The degree of crystallinity (X_c) was estimated from the percentage of crystalline peak area to total scattered area, the d-spacing was calculated using the Bragg equation, the crystallite domain size (L) was evaluated using the Debye-Scherrer formula from the full width at half-maximum (FWHM)[24].

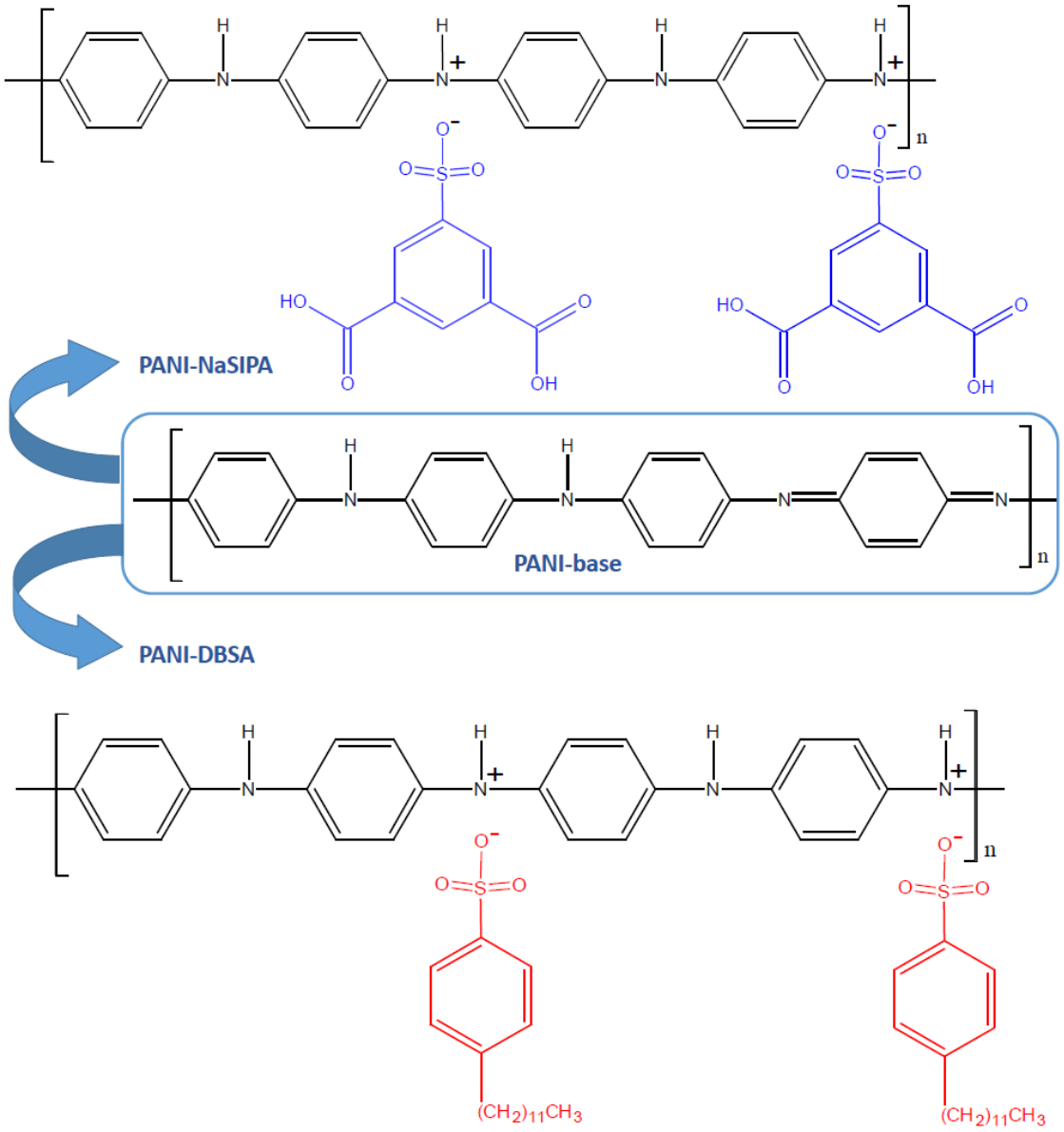

Figure 1. Chemical structure of PANI-base and doped polyanilines, PANI-NaSIPA and PANI-DBSA.

The morphology of the polymer samples dispersed in isopropanol was evaluated by transmission electron microscopy (TEM, Jeol JEM 1010 (80 KV)).

The three parameters constituting ZT (σ, α and κ) were measured on specimens prepared by compression molding (2.5 x 2.5 cm x 0.5 mm) at 90°C, applying a pressure of 100 bar for 2 minutes. Electrical resistivity at room temperature was calculated by the four-point method (LORESTA-GP, Mitsubishi Chemical, MCP-T610). The electrical conductivities (σ) reported for each polymer are the mean values of at least 24 readings determined on different samples.

The Seebeck coefficient (α) was measured using a home-made device (a broad description of the device, experimental parameters and its reproducibility are reported in supplementary material, **Figure S1**). The sample was mounted between two copper blocks (4x4 mm^2), while a heat pulse was applied to one end of the sample to create a thermal gradient. The total temperature difference was maintained below 2 K, and the linear ΔV/ΔT variation was recorded at each base temperature (**Figure S2**). The measurements were performed under vacuum between 200 and 325 K.

Thermal diffusivities were measured by the flash diffusivity technique with the thermal analyzer (LFA 447 Nanoflash, Germany) on square samples of 8 mm length and 0.5 mm thickness at 300, 325 and 350 K. Test samples were sprayed with a coating of graphite on both sides before testing (for uniform thermal adsorption). The illumination source was a Xenon flash lamp with a spectral output characterized by a broadband in the visible wavelength and a complex line spectrum in the near IR. Pulse corrected Cape Leman model was used to analyze the data in analysis software. The thermal conductivities were derived from the following equation:

$$\kappa = a\ \rho\ c_p \qquad \textbf{(3)}$$

Where κ is the thermal conductivity, a is the thermal diffusivity, ρ is the density of samples and c_p is the specific heat capacity. Due to the hygroscopic nature of some PANIs the density was estimated from the weight and dimensions of the samples. The specific heat capacity c_p of test sample was obtained by Differential Scanning Calorimetry (DSC TA Instruments 2010) using sapphire as standard. Both thermal diffusivity and specific heat capacity are the average value of three replicas for each sample.

3. Results and discussion

When optimizing PANI for thermoelectric applications, the first strategy consists on tuning the doping level, which is controlled by the molar acid concentration in the redoping step.

3.1. Electrical conductivity

Figure 2 shows the changes in electrical conductivity of PANI salts at room temperature, as a function of DBSA and NaSIPA molar concentrations. The two organic acids lead to dissimilar results; firstly, the room temperature electrical conductivity of PANI-DBSA is always 4 to 70 times higher than that of PANI-NaSIPA. Furthermore, the electrical conductivity of PANI-DBSA increases continuously with the concentration of DBSA up to ≈1.25 M, reaching relatively large values of ≈30 S/cm, and declines at 1.5 M. Regarding PANI-NaSIPA, the electrical conductivity also increases with the concentration of the dopant, although it reaches much smaller values; the maximum value of ≈0.5 S/cm is achieved at NaSIPA 0.75 M.

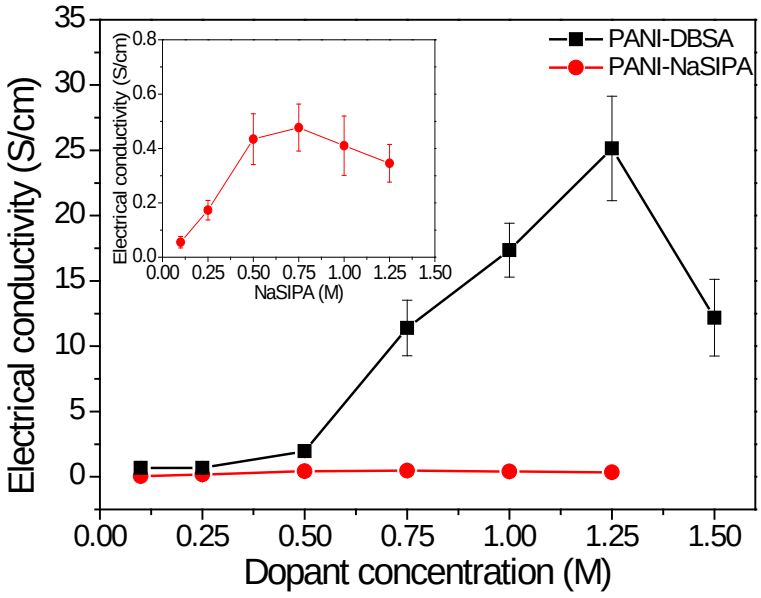

Figure 2. Electrical conductivities of PANI-DBSA and PANI-NaSIPA at various molar acid concentrations at room temperature.

In order to understand the effect of the nature of the organic dopant and its molar concentration on the electrical conductivity of doped-PANIs, the chemical, structural and morphological characterization was addressed by elemental analysis, FTIR, XRD, and TEM.

The S/N ratio calculated by elemental analysis on molar basis has been used to estimate the extent of doping when organic sulfonic acids are used as dopants[18,25]. For PANI-DBSA, the S/N ratio gradually rises up to 0.75 for 1.25 M and then declines (Figure 3). This decrease is explained by the surfactant nature of DBSA and the competition effect or molecular attraction between the adjacent DBSA molecules in concentrated 1.5 M solutions, which make it difficult to perform PANI protonation [26]. Moreover, a positive linear correlation between electrical conductivity and doping level has been found (Figure S3).

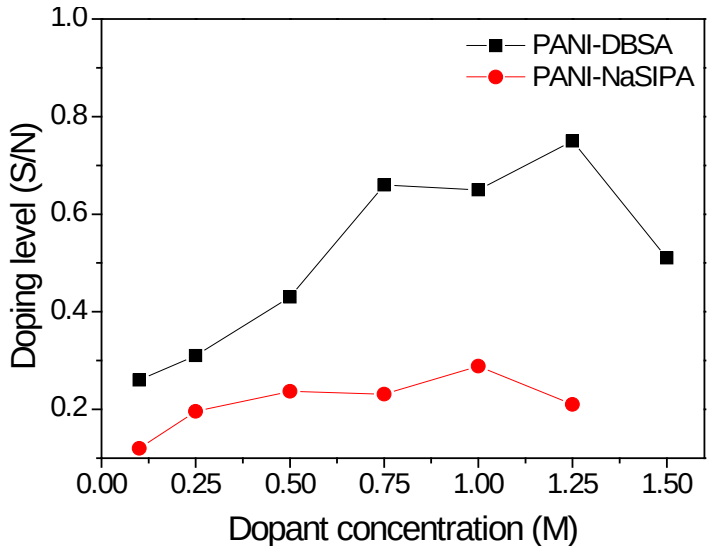

Figure 3. S/N ratio calculated by elemental analysis as a function of the molar acid concentration.

By contrast, the effectiveness of NaSIPA to dope PANI is much smaller and approaches a plateau at acid concentrations ~0.5M (**Figure 3**). The tendency of NaSIPA to form dimers, trimers or tetramers in aqueous solutions account for the low protonation degree (S/N = 0.24 ±0.03) [27].

Doping levels are further confirmed by the shift of the benzenoid (B) band in the FTIR spectra (Figure S4, **S5** and **S6**). Furthermore, the relative intensity between the quinoid (Q) and benzenoid (B) bands ($I_{Q/B}$) provides information on the oxidation level of the polymer. The ratio is closest to the emeraldine form ($I_{Q/B}$ = 1) in PANI-DBSA 0.1 M ($I_{Q/B}$ = 0.93). Minor decreases in the intrinsic oxidation state occurred with rising DBSA concentration, although there are no significant differences between 0.25 M and 1.5 M samples, except for PANI-DBSA 1.25 M, which shows a noteworthy reduction down to $I_{Q/B}$ = 0.75. These values are coherent with the common knowledge that the quinoid

imines are preferentially protonated in the protonic acid doping [28]. Quite the opposite, no variations are observed in the oxidation level of PANI-NaSIPA samples within experimental error ($I_{Q/B}$= 0.91±0.01), which are also close to the emeraldine base.

In parallel with these modifications, shifts and increasing intensity of the bands at 1240 cm^{-1} ($\nu_{C\text{-}N\cdot+}$ in the polaron lattice/$\nu_{C\text{-}N}$ in BBB unit) and ~1129 cm^{-1} (Q=NH^+-B or B-NH^+-B/$\delta_{C\text{-}H}$) are observed in the spectra of all PANI salts (Figure S4 and **S5**). The intensities of the latter two bands, which reflect the concentration of polaron, bipolaron and electron delocalization [29] gradually increase with doping level, although relative variations are smaller in PANI-NaSIPA than in PANI-DBSA samples. Finally, a sharp raise in both bands is observed in the PANI-DBSA 1.25 M spectrum, which is consistent with the maximum doping level and electrical conductivity, due to formation of the most delocalized structure.

Together with the higher doping level, the enhanced electrical conductivity of PANI-DBSA with respect to PANI-NaSIPA is supported by structural differences observed by XRD diffraction and TEM.

Both PANIs have very low crystallinity degree (Tables S1 and S2), but the PANI-DBSA diffraction patterns show an additional peak at small angle (2θ = 2.88º to 3.19º) (Figure S7) indicative of a layered mesomorphic structure, in which the alkyl tails of the counterions function as spacers with some degree of interdigitation between parallel planes of the polymer backbones. For a given dopant, both the intensity of the low angle reflection and the interlayer d-spacing are influenced by the doping level [30], as depicted in **Figure S8A** and **B**. Moreover, reductions in the interlayer spacing are followed by a shrinking in the π-π interchain stacking distance between the PANI phenyl rings and viceversa. Accordingly, the maximum peak intensity and the shortest intralayer d-spacing (better π-π overlap) correspond to PANI-DBSA 1.25 M (S/N= 0.75) (Table S1).

Contrary to previous authors, the electrical conductivity of PANI-DBSA still increases for protonation levels >50% despite the formation of bipolarons, which have restricted carrier mobility compared to polarons [31]. In our case, the improvement of electric properties at high doping level is assisted by the formation of the layered structure as opposed to a three-dimensional close packing unit-cell. Larger intensity of the lower angle peaks reflects an increase in the overall hydrocarbon order within the long alkyl

side DBSA chains arranged between the layers, perpendicular to the PANI main chain. Simultaneously, the rigidity of the PANI chains is increased due to electronic repulsion between the hydrophobic alkyl DBSA chains and the polar nature of cationic PANI. This leads to a more planar chain conformation, with reduced torsion angles between the phenyl rings and the plane of the backbone, which favors π-π stacking (interchain diffusion) and the effective conjugation length (intrachain transfer) [30,32-34]. Therefore, both the interchain diffusion of carriers and the intrachain transportation are promoted (**Figure 4**). These data are consistent with improved carrier transport and a longer mean free path [12].

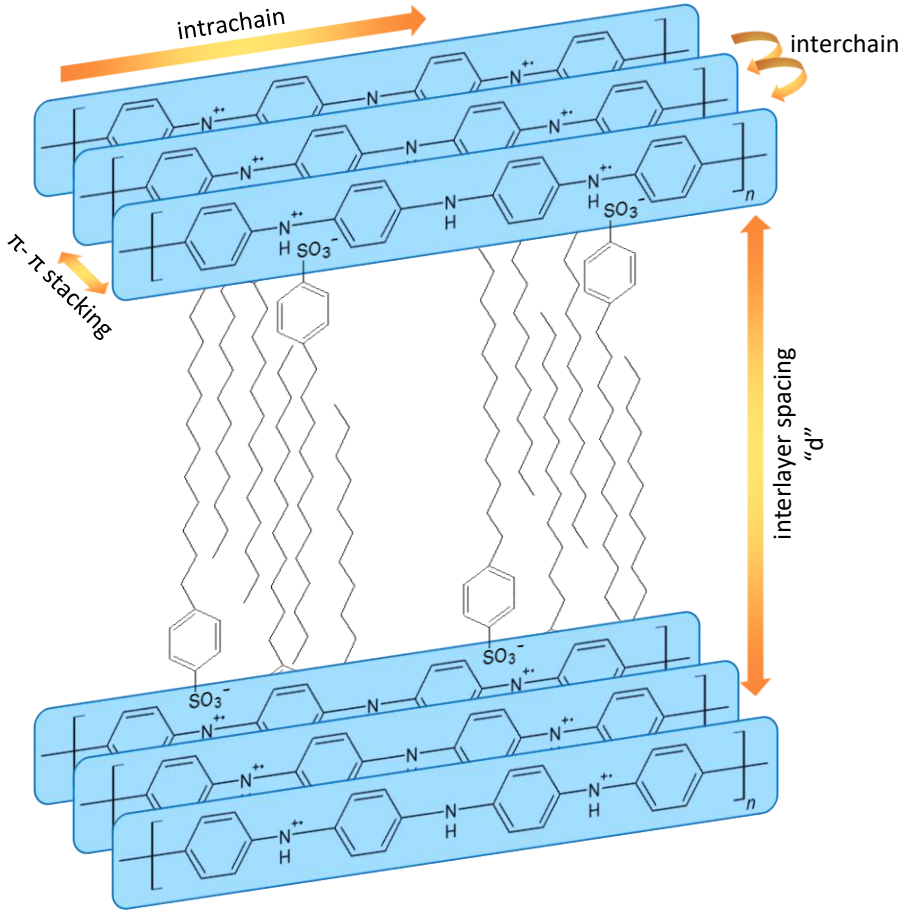

Figure 4. Schematic drawing proposed for the layered structure of PANI-DBSA.

The aforementioned structural differences between the two series of doped PANIs are also reflected in the morphology observed by TEM (**Figure 5**).

Nanorod structures, partially or totally covered by the agglomeration and adsorption of granules and flakes on their surface, are observed for low DBSA doping levels and all PANI-NaSIPA samples. For high DBSA molar concentrations, and due to its surfactant

nature, these agglomerates evolve to a smooth enveloping layer, with no identifiable particle structures. This layer of chemically bound and free DBSA, forms a continuous network in compression-molded samples and may be a determining factor in the formation of conductive pathway structures [35,36].

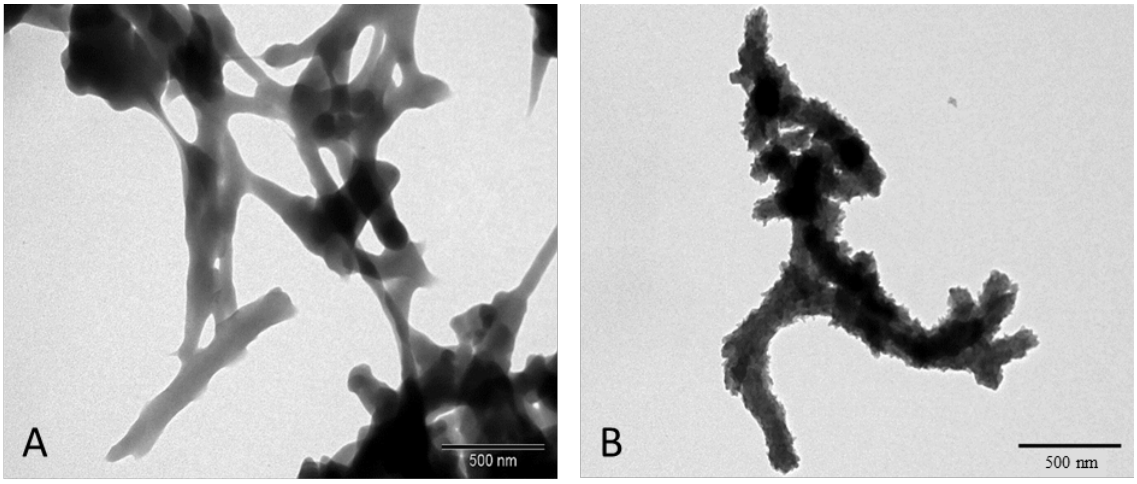

Figure 5. TEM images of A) PANI-DBSA 1.25M_50Kx and B) PANI-NaSIPA 1.25M_50Kx.

In summary, the higher electrical conductivity values of PANI-DBSA, in comparison with those of PANI-NaSIPA, are due to both the higher doping levels and the layer structure of PANI-DBSA.

3.2. Seebeck coefficient

Figure 6 shows the variation of the Seebeck coefficient for the two PANI salts at room temperature as a function of the dopant molar concentration. Consistent with its high doping level, the Seebeck coefficient of PANI-DBSA is very small and fairly constant of the order of 1 μV/K, within experimental error. Quite the opposite, the Seebeck coefficient of PANI – NaSIPA is between 4 and 34 times greater than that of PANI-DBSA and shows a clear decrease upon raising the acid molar concentration up to NaSIPA ≈0.8 M. The last behaviour has been described previously by several authors [1,37]. Accordingly, the lightly doped PANI-NaSIPA samples have lower electrical conductivities and larger Seebeck coefficients compared to those of heavily doped PANI-DBSA[4].

For both types of PANIs, Power Factors ($PF=\alpha^2.\sigma$) are of the order of 10^{-3} μWm^{-1} K^{-2}. PANI-DBSA 1 M and PANI-NaSIPA 0.5 M present an optimal compromise between the two properties involved; hence, these two samples, which have the same PF (~4 x 10^{-3}

μWm^{-1} K^{-2}), have been chosen to study the temperature dependence of the TE properties.

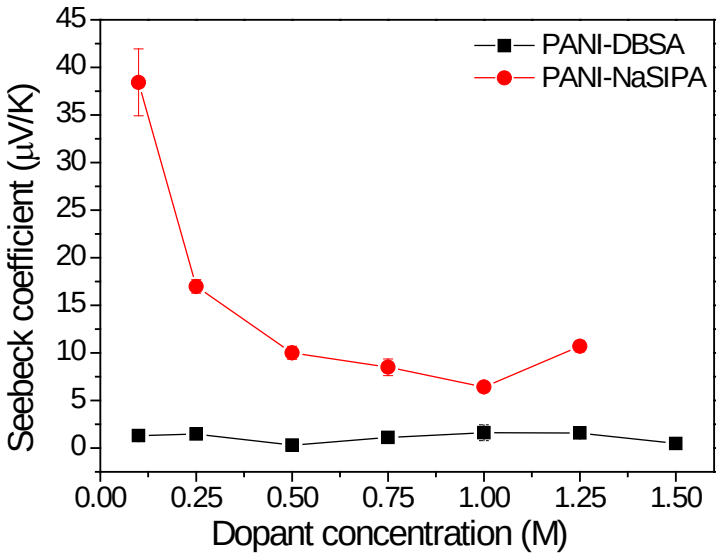

Figure 6. Seebeck coefficients of PANI-DBSA and PANI-NaSIPA at various molar concentrations at room temperature.

The Seebeck coefficient is a very useful property to identify the intrinsic conduction processes in conducting polymers. As no current flows through the sample, it is not as dependent on material imperfections as electrical conductivity [38]. The temperature dependence of the Seebeck coefficient for samples of PANI-DBSA and PANI-NaSIPA is shown in **Figure 7**.

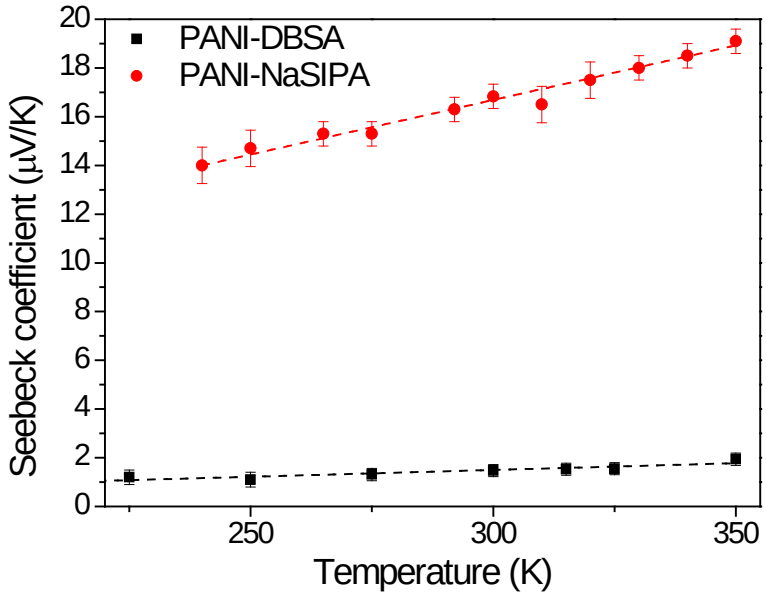

Figure 7. Temperature dependence of the Seebeck coefficient of PANI-DBSA 1M and PANI-NaSIPA 0.5M.

The Seebeck coefficient of PANI-DBSA 1 M is very small and nearly independent of temperature. This is characteristic of polaronic hopping, where α can be described from the Heike´s formula:

$$\alpha = \frac{k}{q}\, ln\left(\frac{c}{1-c}\right) \quad \textbf{(4)}$$

Here *c* is the carrier concentration or doping level (carriers per site) and *q* is the electron charge [4]. Fitting of the experimental data gives c≈0.49 (hole type), which is a little bit lower than the doping level estimated by the S/N ratio (0.65).

Concerning PANI-NaSIPA, although the conductivity is small and we could therefore expect an activated temperature dependence of the thermopower, it increases linearly with temperature in a wide temperature range, which is characteristic of diffusive (metallic-like) conduction. This apparent discrepancy probably reflects the inhomogeneous nature of the samples, with different transport mechanisms. Kaiser analysed the temperature dependence of the thermopower in heterogeneous conducting polymers (conducting fibrillar paths of polymer connected by regions with lower conductivity) with different dopant concentrations [39]. In this case, thermopower is dominated by the highly conducting regions, with a contribution $\propto T^{1/2}$ from variable range hopping:

$$\alpha = aT + bT^{1/2} \quad \textbf{(5)}$$

For highly conducting samples the first term of this equation can be equated to the Mott's formula for thermopower [40].

If we assume a single parabolic band in the more conduction regions, the first term of equation (5) can be approximated by:

$$\alpha = \frac{8\pi^2}{3e}\left(\frac{k_B}{h}\right)^2 m^* \left(\frac{\pi}{3n}\right)^{2/3} T \quad \textbf{(6)}$$

Lee et al. measured an effective mass, $m^* \approx 2m_e$ for highly conducting PANI [12]. Using this value in equation 6, the estimated charge carrier density *n* is $\approx 3\times10^{21}$ e/cm^3 for PANI-NaSIPA. This result is consistent with that obtained from previous authors for this class of materials.

The observed behaviors for PANI-DBSA and PANI-NaSIPA differ from conclusions extracted from previous research works for homogeneous systems, where the Seebeck

coefficient of lightly doped organic semiconductors is for the most part independent of temperature. Certainly, this is a complex issue and apart from the doping level, other factors, such as the degree of heterogeneity and order in the microstructure, must be taken into account and deserve further systematic exploration.

3.3. Thermal conductivity

Regarding thermal conductivity, **Figure 8** shows the variation of this parameter with the molar acid concentration for the two organic dopants at 300, 325 and 350 K [3,41].

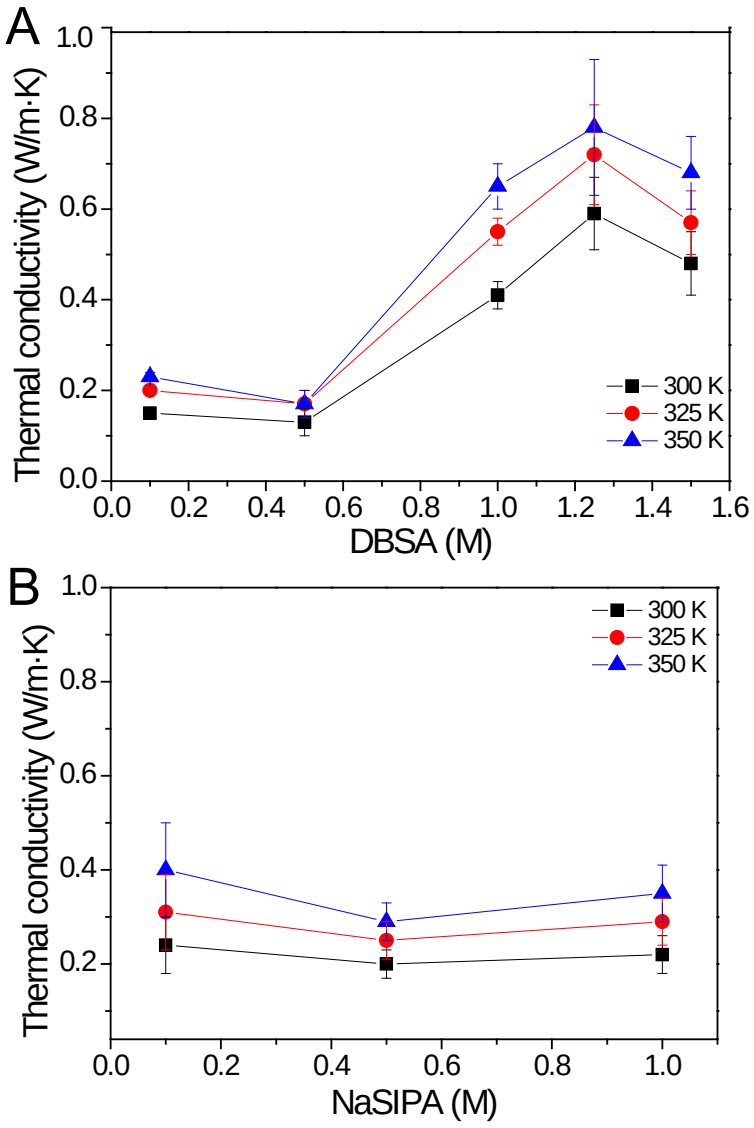

Figure 8. Thermal conductivity of A) PANI-DBSA B) PANI-NaSIPA at 300, 325 and 350 K.

For PANI-DBSA samples, the thermal conductivity (κ) is low and nearly constant (0.14±0.2 W/m·K) for DBSA molar concentrations below 0.5 M, then increases with the doping level up to 0.59±0.08 W/m·K at room temperature. Quite the opposite, the thermal conductivity of PANI-NaSIPA is independent of the charge carriers within

experimental error (0.22±0.02 W/m·K). For both type of PANIs, and like most low crystalline polymers, the thermal conductivity increases with temperature [4,8]. The results lie within the range found in the literature for PANI thermal conductivity, spanning from 0.02 to 0.542 $W.m^{-1}\ K^{-1}$ [5]. Specifically, thermal conductivity values of ~0.2 $W.m^{-1}\ K^{-1}$ have been reported for PANI-DBSA at 300 K [2].

These low κ values and the absence of correlation of the thermal conductivity with electrical conductivity are due to the van der Waals or H-bonding contact between molecules and structural disorder, that cause strong phonon scattering and negligible contribution of electrical carriers [42]. The thermal conductivity is the summation of an electronic part (κ_e) and a lattice contribution ($\kappa_{ph,}$ phonons). A first approximation to the electronic contribution could be made from Wiedemann-Franz (WF) law:

$$\kappa_e = LT\sigma \qquad \textbf{(7)}$$

where σ is the electrical conductivity, T is the temperature and L is the Lorentz factor ($L=2.45\times10^{-8}\ W\Omega\ K^{-2}$). Following **Eq. (7)**, we have calculated a maximum value of κ_e of the order of 10^{-6} to 10^{-4} W/m·K at 300 K. Although applying WF law to the conduction regime of a system like that studied here is a very crude approximation, it can give an idea of the order of magnitude of the electrical contribution to the thermal conductivity. Therefore, in accordance with previous studies on PANI [3,43], we can safely assume that the total thermal conductivity is dominated by the lattice vibrations, which can be affected by the type and dopant concentration that may alter the heat capacity and the density of the polymer [4].

Furthermore, in the case of PANI-DBSA there is an increase in the thermal conductivity with doping level at S/N values > 0.5. These experimental findings may be ascribed to the formation of the layered structure, described in preceding paragraphs. Both the intensity of the low angle reflection and the interlayer d-spacing, increase at high doping levels (Figure S7**A**); this morphology can decrease the boundary phonon scattering and promote the transport of phonons in the heat transfer process.

3.4. Figure of merit

As a final point, the magnitude of the dimensionless thermoelectric figure of merit, ZT, determines the efficiency of the energy conversion. The ZT values of PANI-DBSA and PANI-NaSIPA, shown in **Figure 9**, are of the same order of magnitude than those found

in the literature for pure bulk PANI at room temperature, which span from 7×10^{-7} [44,45] to ~2.75×10^{-5} [8,37]. In particular, a ZT of ~1.5×10^{-5} has been encountered for PANI-DBSA prepared by direct synthesis [2], whereas, as far as we know the thermoelectric properties of PANI-NaSIPA have not yet been investigated.

ZT of PANI-DBSA reaches its maximum values, 3.3×10^{-6} and 3.2×10^{-6}, at high doping levels for DBSA 1 and 1.25M, respectively. Despite the higher electrical conductivity of PANI-DBSA 1.25M, the simultaneous raise of the thermal conductivity, while the Seebeck coefficient remains nearly constant, explains the analogous value in relation with PANI-DBSA 1M. On the contrary for PANI-NaSIPA, ZT linearly decreases from NaSIPA 0.1M (1.0×10^{-5}) to NaSIPA 1M (2.3×10^{-6}), as a result of variations of the Seebeck coefficient and electrical conductivity. Hence, the ZT value of PANI-NaSIPA 0.5 M is two orders of magnitude higher than that of PANI-DBSA 0.5 M, whereas similar ZT values are obtained at 1 M acid concentration. Therefore, based on the variation trends of ZT with molar acid concentration, the present study offers the novel possibility of improving ZT of organic thermoelectric materials focusing on lightly doped PANIs.

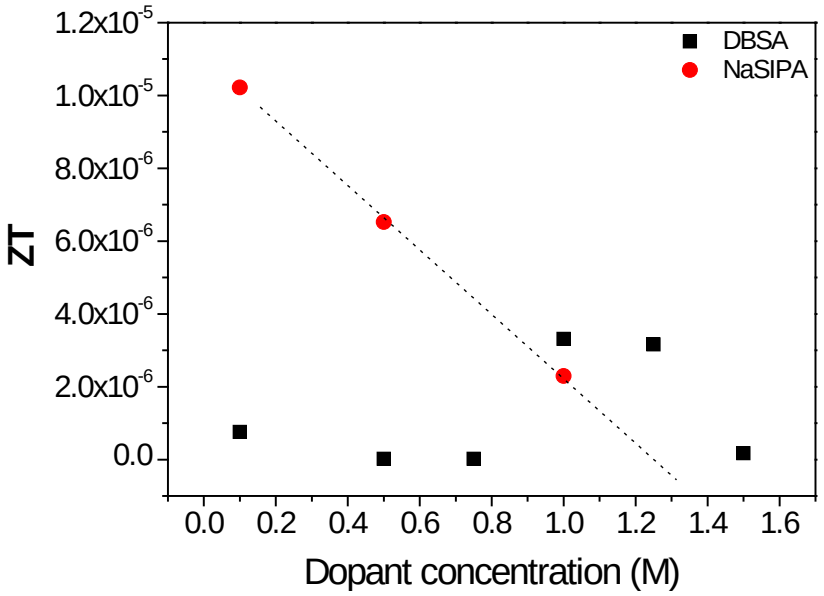

Figure 9. ZT values of PANI-DBSA and PANI-NaSIPA at different acid molar concentrations and 300 K.

4. Conclusions

This study thoroughly describes the characterization of PANI nanorods prepared by an indirect synthetic route and doped with two organosulfonic acids, DBSA and NaSIPA at increasing molar acid concentrations. Carefully choosing the doping agent and adjusting the doping level provide conducting polymers with different structural order, morphology and TE efficiency that may be used for the fabrication of different performing devices for near room temperature applications.

PANI-DBSA materials need high doping levels, in conjunction with the formation of a well-defined layered structure, to achieve moderately high electrical conductivity and thus, maximize ZT, due to the low and constant Seebeck coefficient. The observed hopping behavior mechanism offers potential for thermal power generators with constant voltage that take advantage of the constancy of the Seebeck coefficient over a selected temperature range.

Opposite to this, NaSIPA displays poor doping ability due to its tendency to form dimers, trimers or tetramers in aqueous solutions; thus, the lightly doped PANI-NaSIPA samples show lower electrical conductivities and larger Seebeck coefficients than PANI-DBSA; both magnitudes show opposite trends upon raising the acid molar concentration. Notwithstanding, they have the advantage of moderately high ZT values at low acid molar concentrations, showing a diffusive regimen characteristic of degenerate metallic semiconductors from 200 to 350 K.

Supplementary material

1. Experimental

Measurement of the Seebeck coefficient

Figure S1 shows the home-made device to measure the Seebeck coefficient. Once the base temperature has been stabilized, a voltage (20 mA) is applied to the 300 Ω heater to produce a thermal gradient through the sample. As can be appreciated in **Figure S2A**, the thermoelectric voltage is very stable before applying the voltage to the heater. This is achieved by stabilizing the temperature for a couple of hours, so that the gradient inside the sample is less than 1 mK. This is an important factor for obtaining reliable measurements. Upon heating, the thermoelectric voltage increases progressively up to a thermal gradient of ≈2.5K. At this moment, the heater is switched off and the relaxing voltage is monitored as the thermal gradient decreases. **Figure S2B** the lineal adjustment between the voltage and thermal difference between the edges of the sample can be observed. The slope of the curve is the Seebeck coefficient.

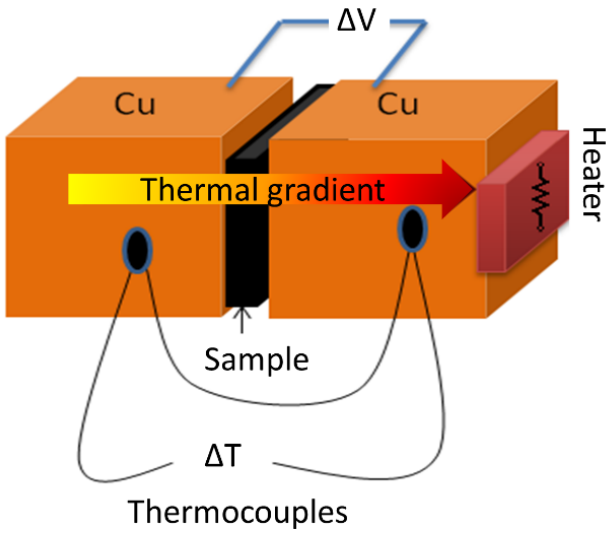

Figure S1. Scheme of the home-made device that measures the Seebeck coefficient.

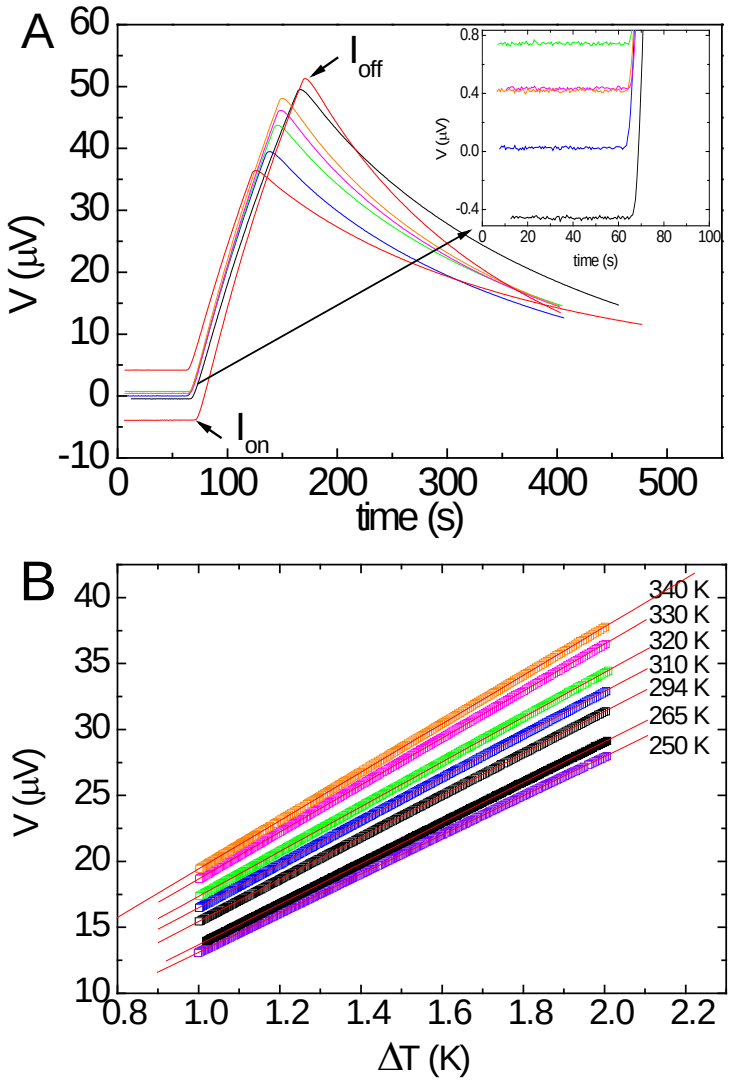

Figure S2. Voltage before and after applying current (A) and adjustment of voltage curves after applying thermal gradient (B).

2. Results

Doping and oxidation levels

In a previous paper, the degree of protonation of DBSA and NaSIPA doped samples calculated as $-N^+/N$ by XPS was found equivalent to the S/N bulk ratio obtained on molar basis by elemental analysis [18]. Thus, the latter has been used to estimate the extent of doping [25]. **Figure S3** depicts the correlation between the electrical conductivity and S/N ratio for PANI-DBSA (R^2= 0.82).

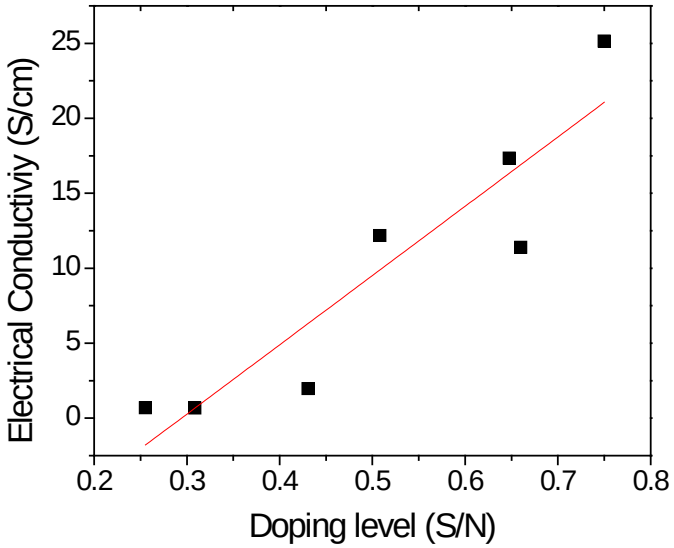

Figure S3. Correlation between electrical conductivity and doping level for PANI-DBSA.

The formation of PANI salts and doping levels have been confirmed by FTIR spectra (**Figure S4** and **Figure S5**). The spectra of PANI salts have been normalized to the absorbance of the quinoid ring-stretching vibration and compared with the original PANI-base. In the range of 1800–800 cm^{-1}, the PANI-base exhibits six major absorption bands at 1592, 1499, 1379, 1307, 1166, and 832 cm^{-1}. They are ascribed to $\nu_{C=C}$ in quinoid ring (Q), $\nu_{C=C}$ in benzenoid ring (B), ν_{C-N} in QBQ units, ν_{C-N} of secondary aromatic amine, N=Q=B/δ_{C-H} and γ_{C-H} (1,4-disubstituted ring), respectively [29].

Protonation with increasing amounts of organic sulfonic acids lead to gradual changes in the spectra. There is an increase in the characteristic absorptions of DBSA and NaSIPA. *DBSA*:2958, 2824 cm^{-1} and 2854 cm^{-1} ($\nu_{CH2asym,}$ ν_{CH2sym}); 1042 and 1010 cm^{-1} ($\nu_{symO=S=O}$ of the anion radicals) [46]; 882 cm^{-1}, 602 and 580 cm^{-1} assigned to S-OH or S-O-C stretching and S-O bending modes). *NaSIPA*:1690 cm^{-1} (ν_{COOH}), 1040 cm^{-1} (ν_{SO3-}), 758 cm^{-1} (1,35-trisubstituted ring of the dopant) and 670 and 622 cm^{-1} (δ_{SO3-}) [20].

Besides, the shoulder assigned to NH^+ deformations at ~1610-1601 cm^{-1} is detected, as well as significant red shifts of the Q and B bands both in PANI-DBSA and PANI-NaSIPA. A positive linear correlation has been found between the red shift of the bencenoid band (B) wavenumber and doping level for DBSA and NaSIPA samples (R^2= 0.85 and 0.99, respectively) (**Figure S6**).

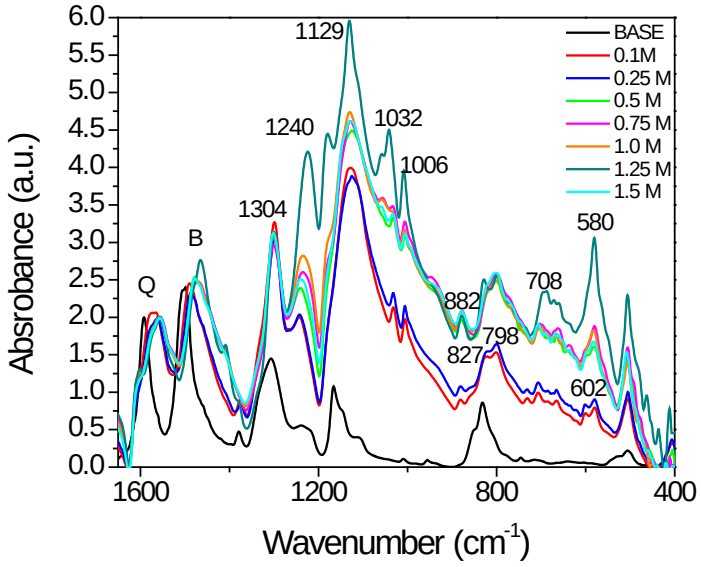

Figure S4. Normalized FTIR spectra of PANI-base and PANI protonated with increasing amounts of DBSA.

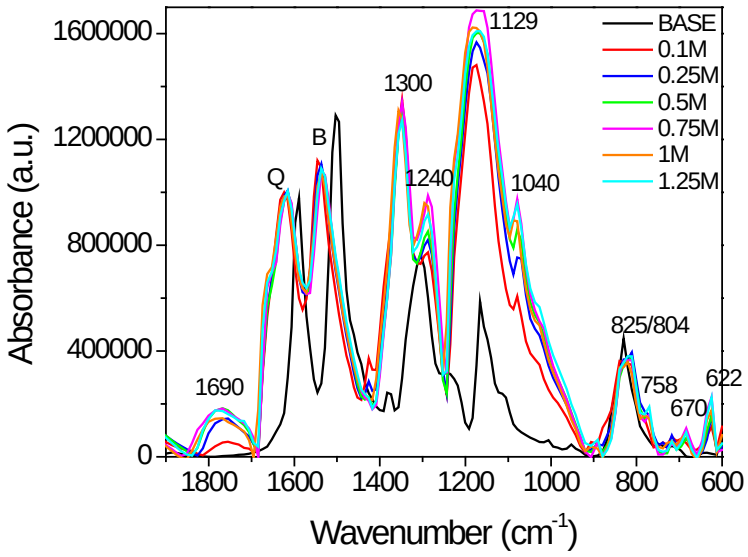

Figure S5. Normalized FTIR spectra of PANI-base and PANI protonated with increasing amounts of NaSIPA in the spectral range between 1900-600 cm^{-1}.

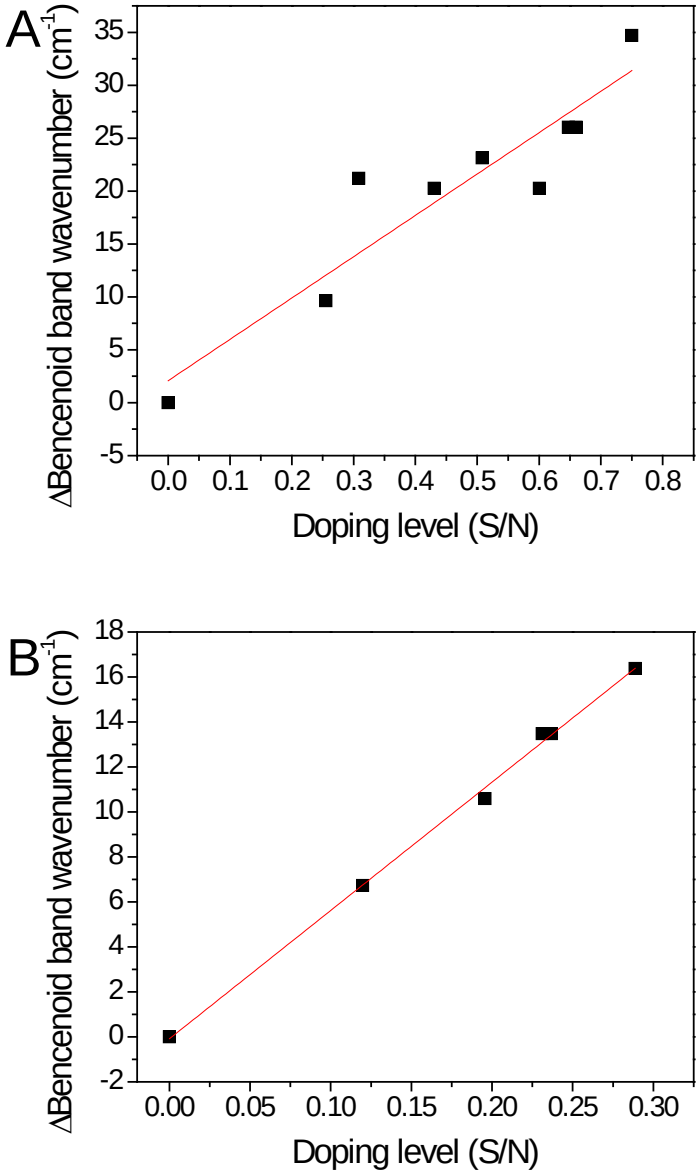

Figure S6. Correlation between the red shift of the bencenoid band wavenumber and doping level of PANI-DBSA (R^2=0.85) (A) and PANI-NaSIPA (R^2=0.99) (B).

XRD

The amorphous PANI-base becomes slightly crystalline when redoped with organosulfonic acids of increasing molarity. The X-ray diffraction patterns of PANI-DBSA and PANI-NaSIPA powders with different doping degrees, normalized to area = 1, are presented in **Figure S7A** and **B**, respectively.

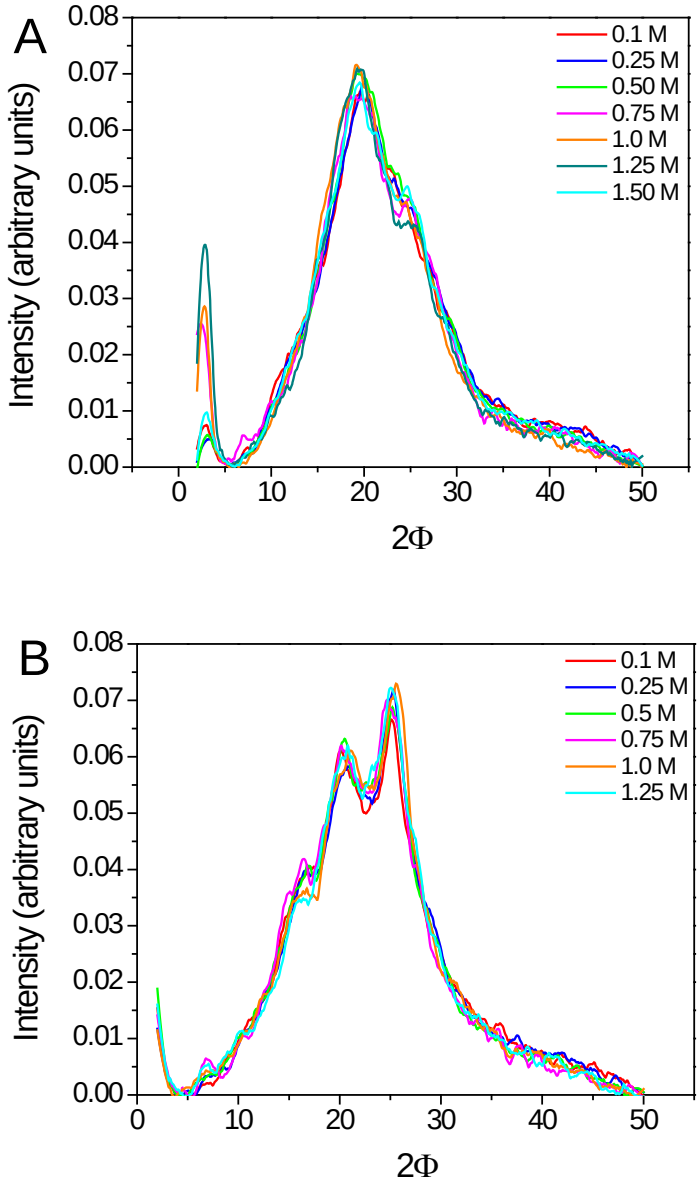

Figure S7. XRD patterns of PANI salts prepared with increasing DBSA (A) and NaSIPA (B) molar concentrations.

The XRD patterns of PANI-DBSA exhibit a broad amorphous peak centered at 2θ~19-21° with some weak features around 25°, which confirm low crystallinity. The corresponding d spacings are related to the transverse PANI interchain distances, thus reflecting the intralayer spacing (chain to chain π-π stacking distance) [12]. Besides, the additional peak observed at small angle (2θ= 2.88° to 3.19°) indicates the presence of layered structures. The corresponding d spacing is indicative of the interlayer distance. Such structure is well-known for PANI-DBSA [30,32,34]. The peak positions, inter and intralayer spacings, normalized intensities and crystallite size for the peak at small angle together with the degree of crystallinity are displayed in **Table S1**. The

determination of the areas and the full width at half-maximum (FWHM) of the peaks at small angle are uncertain due to its incomplete shape. Nevertheless, to extract information on average distance and domain size of the ordered phase, the center and area are determined by fitting the experimental data to a Gaussian function [32].

Table S1. Peak positions (2θ), d-spacings (d x10^{-10}m), normalized intensities (I), crystallite size (L x10^{-10}m) and degree of crystallinity (X_c%) of PANI-DBSA samples of increasing acid molar concentration.

	Interlayer				***Intralayer***				
DBSA (M)	**2θ(°)**	**d**	**I**	**L**	**2θ(°)**	**d**	**2θ(°)**	**d**	**X_c (%)**
0.1	2.9	30.7	0.007	45.6	19.20	4.62	24.65	3.61	13
0.25	3.3	26.9	0.005	49.1	19.85	4.47	-	-	11
0.5	3.1	28.6	0.006	42.1	19.20	4.52	25.50	3.49	12
0.75	2.5	35.6	0.025	40.9	19.15	4.63	-	3.49	18
1	2.7	32.3	0.028	54.3	19.15	4.63	-	-	14
1.25	2.8	31.6	0.040	46.4	19.90	4.46	26.05	3.42	20
1.5	3.0	29.3	0.011	43.0	19.55	4.54	25.95	3.43	10

The low angle reflection is weak for doping levels (S/N < 0.43, [DBSA] < 0.5M) and its intensity linearly increases from this value onwards (R^2= 0.97) (**Figure S8**). From another point of view, the size of the crystalline areas, as determined by L, scale from 41 to 54 A° and no clear correlation is observed with the doping level, although the maximum value corresponds to DBSA 1M (S/N= 0.65).

Moreover, the interlayer d-spacing spans from 26.9 to 35.6 A°. These values are similar to the interlayer distance found for PANI-DBSA in the literature [30,47]. The lamellae distance is primarily determined by the size of the dopant [47] but is also influenced by the doping level [30]. Three distinct doping regimes are observed (**Figure S8B**). Initial doping yields a marked decrease in the interlayer repeat. Further doping, S/N from 0.3 to 0.65, leads to a linear increase in the interlayer spacing up to S/N= 0.66, and finally decreases near saturation doping (S/N= 0.75). Likewise, as can be observed in **Table S1**, reductions in the lamellae distance are followed by a shrinking in the π-π interchain stacking distance between phenyl rings and viceversa. [48].

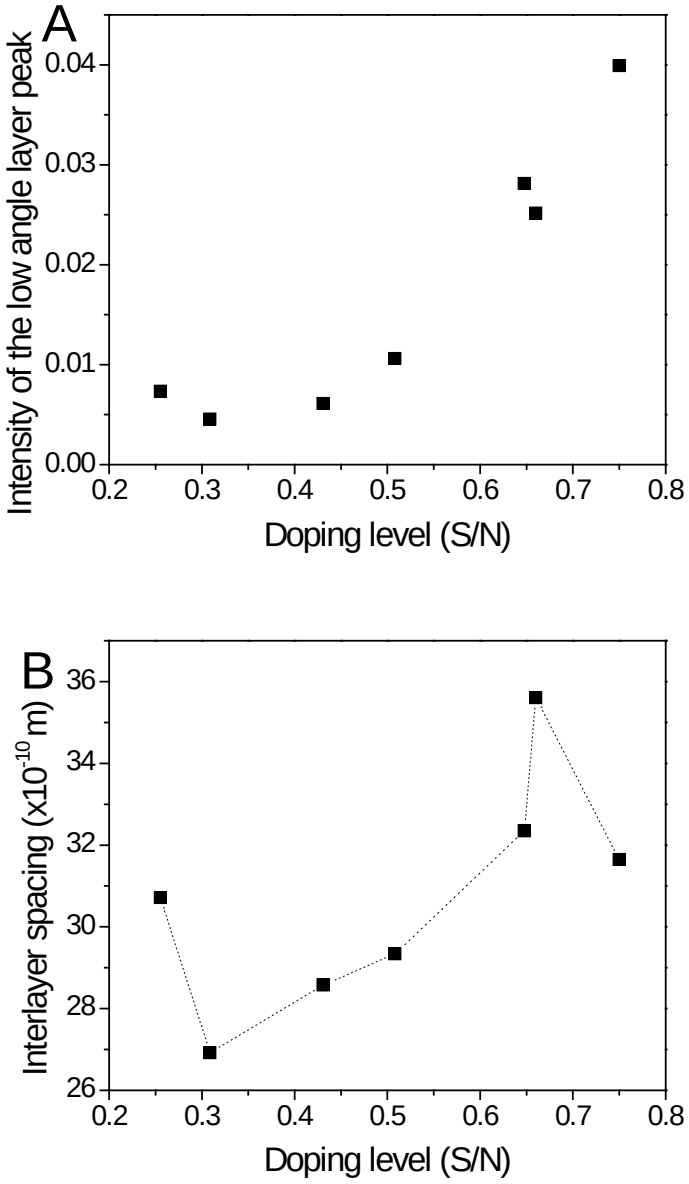

Figure S8. A) Variation of the intensity of the layer ordering reflections of PANI-DBSA as a function of the doping level; B) Variation of the d spacing of the layer ordering reflections of PANI-DBSA as a function of the doping level.

The X-ray diffraction patterns of PANI-NaSIPA samples are similar with that reported earlier for PANI-NaSIPA 0.5M [18], consisting of three sharp peaks, 2θ at ~15.3° ±0.7°, 20.5°±0.4° and 25.2°±0.2°, superimposed on a broad scattering background (**Figure S7B**). These patterns are indicative of crystalline regions of ES-I structure, dispersed in an amorphous medium. In contrast with PANI-DBSA samples, the characteristic peak of an interlayer repeat is not observed at small angle and the degrees of crystallinity are ~twice their values, ranging from 20 to 31% (**Table S2**). Small variations in the degree of

crystallinity and π-π stacking distances are observed with doping level, although no clear correlation has been found with conductivity.

Table S2. Peak positions (2θ), d-spacings (d x10^{-10}m), normalized intensities (I), crystallite size (L x10^{-10}m) and degree of crystallinity (X_c%) of PANI-NaSIPA samples of increasing acid molar concentration.

NaSIPA (M)	**2θ (°)**	**d**	**I**	**2θ**	**d**	**I**	**L**	**X_c (%)**
0.1	20.11	4.41	0.021	25.12	3.54	0.030	35.7	21
0.25	20.83	4.26	0.017	25.28	3.52	0.038	30.1	25
0.5	20.44	4.34	0.019	25.23	3.53	0.026	32.0	20
0.75	20.22	4.39	0.020	24.96	3.57	0.033	27.1	27
1	21.16	4.20	0.023	25.64	3.47	0.041	27.6	31
1.25	20.33	4.37	0.018	25.17	3.54	0.031	30.2	23

References

1. Zhang, Q., Sun, Y., Xu, W. & Zhu, D. *Advanced Materials*, 26, (2014), 6829.

2. Wang, W., Sun, S., Gu, S., Shen, H., Zhang, Q., Zhu, J., Wang, L. & Jiang, W. *RSC Advances*, 4, (2014), 26810.

3. Yan, H., Sada, N. & Toshima, N. *Journal of Thermal Analysis and Calorimetry*, 69, (2002), 881.

4. Bubnova, O. & Crispin, X. *Energy & Environmental Science*, 5, (2012), 9345.

5. Du, Y., Shen, S. Z., Cai, K. & Casey, P. S. *Progress in Polymer Science*, 37, (2012), 820.

6. Khan, Z. U., Edberg, J., Hamedi, M. M., Gabrielsson, R., Granberg, H., Wågberg, L., Engquist, I., Berggren, M. & Crispin, X. *Advanced Materials*, 28, (2016), 4556.

7. Russ, B., Glaudell, A., Urban, J. J., Chabinyc, M. L. & Segalman, R. A. *Nature Reviews Materials*, 1, (2016), 16050.

8. Wu, J., Sun, Y., Xu, W. & Zhang, Q. *Synthetic Metals*, 189, (2014), 177.

9. Bhadra, S., Khastgir, D., Singha, N. K. & Lee, J. H. *Progress in Polymer Science*, 34, (2009), 783.

10. Skotheim, T. A., (CRC press, **1997**).

11. George, S. D., Saravanan, S., Anantharaman, M., Venkatachalam, S., Radhakrishnan, P., Nampoori, V. & Vallabhan, C. *Physical Review B*, 69, (2004), 235201.

12. Lee, K., Cho, S., Park, S. H., Heeger, A., Lee, C.-W. & Lee, S.-H. *Nature*, 441, (2006), 65.

13. Prigodin, V. & Epstein, A. *Physica B: Condensed Matter*, 338, (2003), 310.

14. Bubnova, O. *Thermoelectric properties of conducting polymers*, Linköping University Electronic Press, (2013).

15. Kaiser, A. B., Subramaniam, C. K., Gilberd, P. W. & Wessling, B. *Synthetic Metals*, 69, (1995), 197.

16. Kaiser, A. B. *Advanced Materials*, 13, (2001), 927.

17. Sun, Y., Wei, Z., Xu, W. & Zhu, D. *Synthetic Metals*, 160, (2010), 2371.

18. Horta-Romarís, L., Abad, M.-J., González-Rodríguez, M. V., Lasagabáster, A., Costa, P. & Lanceros-Méndez, S. *Materials & Design*, 114, (2017), 288.

19. Dopico-García, M. S., Ares, A., Lasagabáster-Latorre, A., García, X., Arboleda, L. & Abad, M. J. *Synthetic Metals*, 189, (2014), 193.

20. Saini, P., Jalan, R. & Dhawan, S. K. *Journal of Applied Polymer Science*, 108, (2008), 1437.

21. Park, H.-W., Kim, T., Huh, J., Kang, M., Lee, J. E. & Yoon, H. *ACS Nano*, 6, (2012), 7624.

22. Yang, J. & Weng, B. *Synthetic Metals*, 159, (2009), 2249.

23. Wojdyr, M. *Journal of Applied Crystallography*, 43, (2010), 1126.

24. Pouget, J. P., Jozefowicz, M. E., Epstein, A. J., Tang, X. & MacDiarmid, A. G. *Macromolecules*, 24, (1991), 779.

25. Jayamurgan, P., Ponnuswamy, V., Ashokan, S. & Mahalingam, T. *Iranian Polymer Journal*, 22, (2013), 219.

26. Han, M. G., Cho, S. K., Oh, S. G. & Im, S. S. *Synthetic Metals*, 126, (2002), 53.

27. Duan, J. F. (Google Patents, 2002).

28. Ogurtsov, N. A., Noskov, Y. V., Bliznyuk, V. N., Ilyin, V. G., Wojkiewicz, J.-L., Fedorenko, E. A. & Pud, A. A. *The Journal of Physical Chemistry C*, 120, (2015), 230.

29. Trchová, M. & Stejskal, J. *Pure and Applied Chemistry*, 83, (2011), 1803.

30. Taka, T., Laakso, J. & Levon, K. *Solid state communications*, 92, (1994), 393.

31. Bhadra, S., Singha, N. K., Chattopadhyay, S. & Khastgir, D. *Journal of Polymer Science Part B: Polymer Physics*, 45, (2007), 2046.

32. Zheng, W.-Y., Levon, K., Taka, T., Laakso, J. & Osterholm, J. *Polymer journal*, 28, (1996), 412.

33. Levon, K., Ho, K. H., Zheng, W. Y., Laakso, J., Kärnä, T., Taka, T. & Österholm, J. E. *Polymer*, 36, (1995), 2733.

34. Han, M. G. & Im, S. S. *Journal of applied polymer science*, 71, (1999), 2169.

35. Titelman, G. I., Siegmann, A., Narkis, M. & Wei, Y. *Journal of Applied Polymer Science*, 69, (1998), 2205.

36. Roichman, Y., Titelman, G., Silverstein, M., Siegmann, A. & Narkis, M. *Synthetic Metals*, 98, (1999), 201.

37. Mateeva, N., Niculescu, H., Schlenoff, J. & Testardi, L. R. *Journal of Applied Physics*, 83, (1998), 3111.

38. Kaiser, A. B. *Reports on Progress in Physics*, 64, (2001), 1.

39. Kaiser, A. *Physical Review B*, 40, (1989), 2806.

40. Mott, N. F. & Jones, H., (Courier Corporation, **1958**).

41. Amrithesh, M., Francis Xavier, P. A., Chandraprabhu, V. G., Jayalekshmi, S., Lee, S. T. & Ravi, J. *Transactions of the Indian Institute of Metals*, 64, (2011), 133.

42. Schlitz, R. A., Brunetti, F. G., Glaudell, A. M., Miller, P. L., Brady, M. A., Takacs, C. J., Hawker, C. J. & Chabinyc, M. L. *Advanced Materials*, 26, (2014), 2825.

43. Nath, C., Kumar, A., Syu, K.-Z. & Kuo, Y.-K. *Applied Physics Letters*, 103, (2013), 121905.

44. Yao, Q., Chen, L., Zhang, W., Liufu, S. & Chen, X. *ACS Nano*, 4, (2010), 2445.

45. Limelette, P., Schmaltz, B., Brault, D., Gouineau, M., Autret-Lambert, C., Roger, S., Grimal, V. & Tran Van, F. *Journal of Applied Physics*, 115, (2014), 033712.

46. Lu, X., Ng, H. Y., Xu, J. & He, C. *Synthetic Metals*, 128, (2002), 167.

47. Oh Yoon, C., Hyun Kim, J., Kyung Sung, H. & Lee, H. *Synthetic Metals*, 84, (1997), 789.

48. Hwang, S., Potscavage, W. J., Nakamichi, R. & Adachi, C. *Organic Electronics*, 31, (2016), 31.

CAPÍTULO 5:

Multifunctional electromechanical and thermoelectric polyaniline-poly(vinyl acetate) latex composites for wearable devices

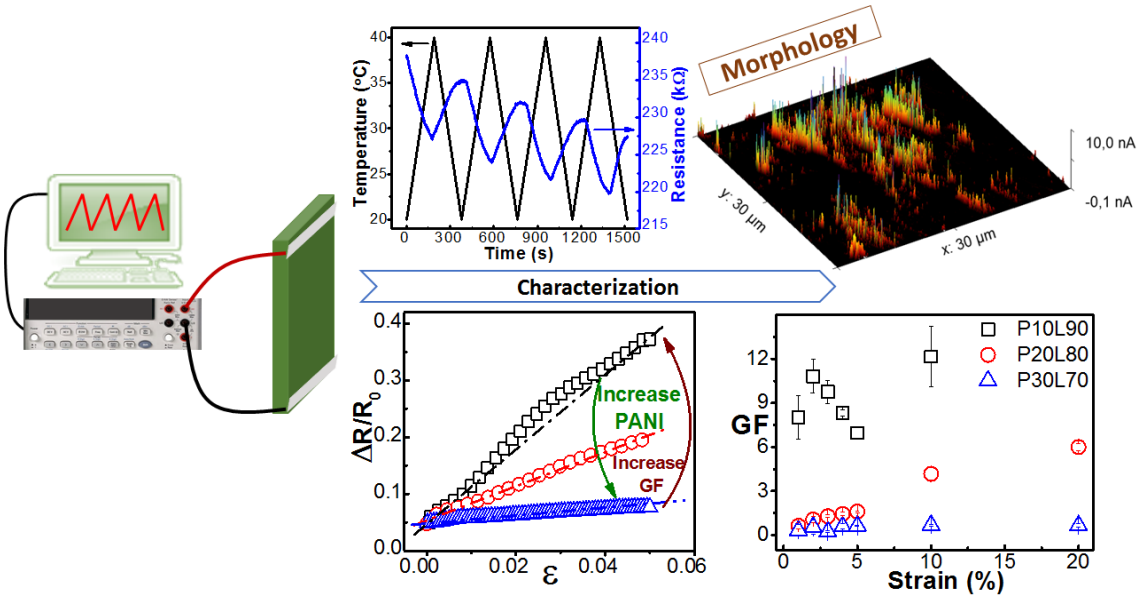

Basado en el artículo:

Horta Romarís, L., González Rodríguez, M. V., Huang, B., Costa, P., Lasagabáster Latorre, A., Lanceros-Mendez, S. & Abad López, M. J. *Journal of Materials Chemistry C* 6**,** (2018), 8502.

1. Introduction

Recently, there has been remarkable accomplishment in the field of stretchable electronics including display panels, radio frequency electronics, light emitting diodes, acoustic devices, elastic conductors, smart sensors, artificial muscles, electronic skin health monitoring systems and other wearable devices[1–6]. Excellent mechanical properties combined with thermoelectric performance, piezoresistive and thermoresistive properties are among the capabilities required for components used in the fabrication of integrated stretchable systems for the aforementioned applications.

The rapid development of next-generation stretchable electronics stimulates the urgent demand for novel, low-cost, ecofriendly, simple processing, light weight and flexible materials. Intrinsically conductive polymers (ICP) such as polyaniline (PANI), poly(3,4-ethylenedioxythiophene) (PEDOT), PEDOT modified with polystyrenesulfonate acid (PEDOT/PSS) or polypyrrole (PPy) represent a fascinating class of materials that can fulfill these requirements and can be an alternative to the currently used commercial metallic and/or ceramics components, although to become competitive with present, novel materials will need to increase in efficiency [3,7–9].

PANI is the most investigated ICP both by academics and industry [7] and can be considered unique owing to its reversible doping/dedoping that affects their electrical conductivity by several orders of magnitude [10]. It has been proven that PANI doped with an inorganic acid, such as hydrochloric acid (PANI-HCl), shows suitable electrical conductivity at room temperature [11]. However, PANI-HCl presents low thermal stability [11] and its electrical conductivity suffers variations for small temperature and humidity changes [12] that can represent a disadvantage for some technological applications, which require heat molding [13]. Other drawbacks are poor mechanical properties [8] and its intractability, i.e., insolubility in common solvents and infusibility, which results in poor processability [14]. A strategy to overcome these issues is the design of novel conductive polymer composites (CPC) which combine the interesting PANI properties with the mechanical performance of insulating thermoplastic or elastomers [15,16]. Thus, the new composites must be molded at room temperature in order to obtain more flexible and ductile materials than PANI.

The literature, presents several examples of PANI blending with several host matrices such as poly(n-butyl methacrylate) (PBMA) [17], poly(dimethysiloxe) (PMDS) [13], styrene-

butadiene-styrene copolymer (SBS) [18,19] or poly(ethylene-vinyl acetate) (PVAc) [20] with promising piezoresistive behaviour for deformation sensors [21]. By contrast, fewer studies have been reported about PANI composites used in the fabrication of flexible temperature sensors [2,22]. Besides, although the thermoelectric performance of many nanocomposites based on PANI-inorganic fillers and PANI-carbonaceous materials has been widely studied [3,23–25], to date, there are no reports describing the thermoelectric properties of PANI-thermoplastic elastomer binary blends. At any rate, tailoring polymeric blends with specific thermal and electrical properties for smart materials is an interesting scientific and industrial alternative for the actual sensors market.

In this context, this paper deals with the development of polyaniline-poly(vinyl acetate) latex nanocomposites (PANI-PVAc) obtained by film–casting at room temperature. Latex technology, which uses water-based polymer emulsions, favors the retention of conductive fillers within the interstitial space between the latex particles upon water evaporation and, thus, the formation of a segregated CPC (s-CPC). This is a low cost and environmentally friendly approach to obtain flexible CPCs with excellent electrical properties, as it does not require the use of toxic and inflammable solvents [26–28].

Morphology and structure were investigated by means of transmission electron microscopy (TEM), atomic force microscopy (AFM), Fourier transform infrared spectroscopy (FTIR) and X-ray diffraction (XRD) and the results were related with the electrical performance. The mechanical properties and thermostability of flexible PANI-PVAc films with 10, 20 and 30 wt.% PANI have been further characterized; these formulations were selected for the evaluation of thermoelectrical, electromechanical and thermoresistive properties in order to elucidate the viability of these materials for large deformations sensors, thermal sensors or other soft-stretchable electronic applications. Composite films with PANI contents near the percolation threshold were more sensitive to mechanical deformation and thermal stimulus than those with PANI contents far above the percolation threshold. By contrast, the latter exhibit higher electrical conductivity and thermoelectric performance as well as improved fatigue resistance.

2. Experimental

2.1. Materials

Aniline and potassium peroxodisulfate (APS) were purchased from Fluka (Steinheim, Germany). Concentrated HCl acid was obtained from Scharlau (Sentmenat, Spain). All the solvents and reagents were at least of 99% purity and used without further purification. Water was purified on a Milli-QUltrapure 109 system (Millipore, Molsheim, France).

Polyaniline doped with hydrochloric acid (PANI-HCl), prepared as described by Park [29], filtered under vacuum and freeze-dried has an estimated molecular weight [30] of 6,300 $g \cdot mol^{-1}$. Vinnapas EP 4014 latex, supplied by Wacker (München, Germany), is an aqueous, plasticizer-free polymer dispersion of poly(ethylene-vinyl acetate) (PVAc) (55 wt.% solids in water). The experimental determined amount of vinyl acetate comonomer from elemental analysis is 72.4%. The densities of PVAc and PANI, calculated by the Archimedes method, are 1.039 and 1.26 $g \cdot cm^{-3}$, respectively.

2.2. Composite preparation

A simple cast film method was followed for the preparation of PANI-PVAc latex composites, preceded by the physical mixture of the components. A prerequisite for the successful implementation of latex technology is the stable dispersion of nanofillers in water [28]. Therefore, after homogenizing PANI powder in a mortar, water was added and the resulting solution was sonicated during 5 min using a Digital Sonifier 450, Branson. The aqueous PANI dispersion was then combined with Vinnapas latex and further sonicated between 5-30 min depending on the composition. Finally, this mixture was cast on a Teflon mold and the solvent was allowed to evaporate for 72 h at room temperature. The resultant dry films have an opaque black appearance with thicknesses ranging from 150 to 300 μm (MarCator 1080, Mahr digital micrometer). The nomenclature adopted for the PANI-PVAc latex composites, the composition and the mechanical behaviour of the films are shown in **Table 1**.

Table 1. Composition of PANI-PVAc composites.

Composites	PANI (wt.%)	PANI (vol.%)*	Type of film
P2.5L97.5	2.5	2.1	Ductile
P5L95	5	4.2	Ductile
P10L90	10	8.4	Ductile
P17L86	17	15	Ductile
P20L80	21	18	Ductile
P30L70	27	23	Ductile
P34L66	34	30	Ductile
P41L59	41	36	Less Ductile
P43L57	43	38	Less ductile
P46L54	46	41	Brittle
P50L50	50	45	Very Brittle
P55L45	55	50	Very Brittle

* The volume additivity law is used to convert weight% to volume%.

2.3. Composite characterization

The morphology of the composites was evaluated by transmission electron microscopy (TEM) with a JEOL JEM 1010 (80 KeV) equipment after applying 10 µL of the aqueous pre-composites dispersions to a copper grid.

Tapping mode atomic force microscopy (AFM) is used to characterize the film topography of a representative composite; measurements at room temperature were performed using a commercial Veeco-Brucker MultiMode system. The system is combined with the high-sensitivity conductive working mode (C-AFM) that allows imaging morphology along with local current. The stylus of the C-AFM tip behaves as the top electrode in the microscale dimension; it is parked on the top of the polymer bump and a voltage scan is applied from 3 to -3 V while measuring the current.

The Fourier-transform infrared (FTIR) data were recorded on a Jasco 4700 spectrometer equipment. The absorption spectrum of the PANI was performed in Potassium Bromide (KBr) pellets. The PVAc and composite films were analyzed in the attenuated reflection mode (ATR-IR) by using the above mentioned spectrometer equipped with the MIRacle^{TM} ZnSe Single Reflection Horizontal ATR Accessory. All the spectra were collected from 4000 to 600 cm^{-1} with a 4 cm^{-1} resolution over 100 scans and subjected to baseline correction. The ATR spectra were further subjected to ATR correction and normalized with respect to the maximum of the carbonyl peak ($\nu_{C=O}$) of PVAc at 1731 cm^{-1}.

X-ray patterns were recorded in step-scan mode from 2° to 50° with a 2θ step of 0.05° using a D5000 diffractometer (XRD, Siemens- Bruker) with CuKα line irradiation (λ= 1.541Å). The PVAc diffractogram was used to subtract the background and amorphous contributions in the composites. The difference patterns were deconvoluted into the crystalline constituents using Gaussian function peak shape approximation in the open-source software Fityk [31]. The degree of crystallinity (X_c) was estimated from the percentage of crystalline peak area to total scattered area. The d-spacing was calculated using the Bragg equation and the crystallite domain size (L) was evaluated using the Debye-Scherrer formula from the full width at half-maximum (FWHM) [32].

Tensile stress–strain properties were characterized using an Instron 5566 universal testing machine (Instron Canton, MA) operating at room temperature and at a crosshead speed of 5 mm·min^{-1} for 5 min, followed by a test speed of 50 mm·min^{-1} until failure. Young modulus (E), strength and strain at break point were calculated from stress-strain curves as the average of five rectangular shaped samples of 150 x 15 mm and thickness of ≈0.5- 0.2 mm.

Thermogravimetric analysis (TGA) was performed with a Perkin-Elmer TGA-7 over a temperature range of 25 to 800 °C at a heat rate of 10 °C·min^{-1} under oxygen atmosphere.

The thermoelectric figure-of-merit (ZT) is a common measure of a material's energy conversion efficiency:

$$ZT = \frac{\sigma\, \alpha^2}{\kappa} T \qquad \textbf{(1)}$$

where σ, α, κ, and T are electrical conductivity, Seebeck coefficient, thermal conductivity and absolute temperature, respectively [24]. The three parameters constituting ZT were measured on the PANI-PVAc latex films.

Electrical resistivity at room temperature was calculated by the four-point method (LORESTA-GP, Mitsubishi Chemical, MCP-T610). The electrical conductivities (σ) reported for each polymer are the mean values of at least 40 readings determined on different samples. Conductivity was measured on the top and bottom surfaces to confirm homogeneity of the composite films.

The Seebeck coefficient (α) was measured using a home-made device [30].The sample was mounted between two copper blocks (4 x 4 mm^2) while a heat pulse was applied to one end of the sample to create a thermal gradient. The total temperature difference was maintained below 2K, and the linear ΔV/ΔT variation was recorded at each base temperature. The measurements were performed under vacuum between 200 and 325 K.

Thermal diffusivities were measured by the flash diffusivity technique with the thermal analyzer (LFA 447 Nanoflash, Germany) at 300 K on square samples of 8 x 0.5 mm of length and thickness, respectively. Test samples were sprayed with a coating of graphite on both sides before testing. Pulse corrected Cape Leman model was used to analyze the data in analysis software. The thermal conductivities were derived from the following equation:

$$\kappa = a\ \rho\ c_p \qquad \textbf{(2)}$$

where κ is the thermal conductivity, a is the thermal diffusivity, ρ is the density of samples and c_p is the specific heat capacity. The density has been estimated from the additivity law. The specific heat capacity was obtained by Differential Scanning Calorimetry (DSC TA Instruments 2010) using sapphire as reference material and following the standard UNE-EN ISO 11357-4[33].Both thermal diffusivity and specific heat capacity are the average value of three replicas for each sample.

Electromechanical measurements were carried out using the universal testing machine (Shimadzu AG-IS) in uniaxial strain mode. Rectangular samples of 20 x 10 mm and thickness of ≈0.5- 0.2 mm were analyzed. The silver painted electrodes were placed inside the mechanical claws for good electrical contact and for avoiding any

deformation during mechanical cycles. The electromechanical behaviour of the PANI-PVAc composites was evaluated as the average of 4 uniaxial load-unload cycles at 1, 5 and 10 mm·min^{-1} for 1, 2, 3, 4, 5, 10 and 20% deformation. The electrical resistivity variation was evaluated with a digital multimeter (Agilent 34401A). In order to analyze the long time electromechanical stability, 100 cycles were performed for 5% deformation at 5 mm·min^{-1}. All experiments were conducted in atmospheric pressure and at room temperature.

The electromechanical sensibility of the blends was evaluated by the gauge factor (GF) defined as [34]:

$$GF = \frac{\Delta R/R_0}{\Delta l/l_0} = \frac{d\rho/\rho_0}{\varepsilon} + 1 + 2\nu \quad \textbf{(3)}$$

where *R* is electrical resistance, ρ is resistivity, *v* is Poisson coefficient, *l* the mechanical displacement and $\varepsilon = \Delta l/l_0$. The geometrical factor $(1 + 2\nu)$ depends on the properties of the materials where the maximum value is *GF* ≈ 2 for elastomers with a Poisson coefficient of 0.5 [35].

The thermal effect on the resistive properties of the blends was measured using a digital multimeter Agilent 34401A (for measuring the electrical resistance) synchronized in real time with the temperature oven Linkam THMSE 600. The temperature changes from 20 up to 40 °C and from 20 up to 100 °C at a rate of 10 °C·min^{-1}. The thermoresistive sensibility (S) is defined as[2]:

$$S = \delta(\Delta R/R_0) \times {}^{100}/_{\delta T} \quad \textbf{(4)}$$

where *R* is electrical resistance and δT the temperature increment in °C.

3. Results and discussion

3.1. Morphological and structural characterization

The morphology of PANI nanoparticles and PVAc latex microspheres in the initial dispersion was determined by TEM. **Figure 1A** shows that pure PVA$_C$ latex consists of spherical particles with diameters between 0.5 and 1 µm. In *P30L70* dispersions (**Figure 1B-C**), PANI exhibits the same nanorod morphology described in a previous work [36]. Nanorods, with 10-15 nm diameter and variable length from 70 to 300 nm, are highly aggregated forming small clusters of thickness ranging from 65 to 95 nm.

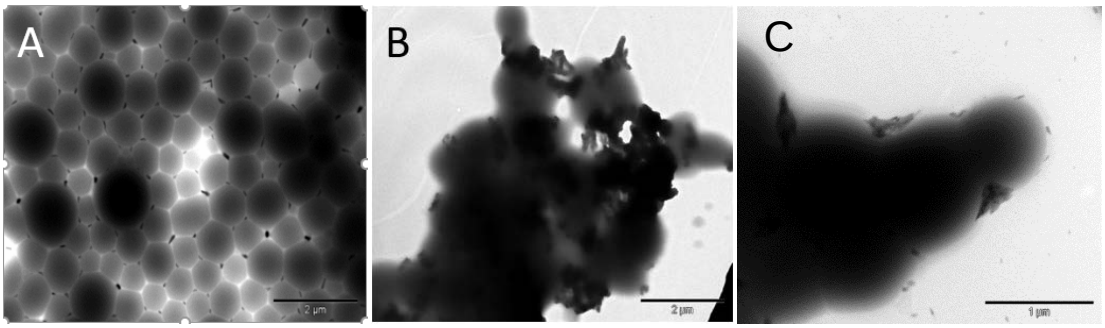

Figure 1. TEM images of A) PVAc latex film and B) *P30L70* dispersion at x15000 magnification and C) *P30L70* x40000 magnification.

Smaller agglomerates or individual nanorods, will eventually fill the interstitial space between the latex μspheres and create the interconnected conductive pathways, as is confirmed by AFM images (**Figure 2**).

AFM in conductive mode is used to image the PANI network inside the blends. Composites with PANI contents below 30 wt.% are too resistive to be measured by this technique; therefore, the surface morphology of the composite *P30L70* was scanned (**Figure 2A** and **D**) and then, the conductive tip was parked on the top of a bump and a voltage scan applied (**Figure 2B, C** and **E**). The 30 x 30 μm three-dimensional and height images provide a detailed view of the particle arrangement and a unique insight of the distribution of the conductive phase within the matrix.

Conductive PANI is organized around oval domains of PVAc latex and confined in the small voids observed at the junction of latex particles, forming a segregated conductive network throughout the observed area, with the inevitable presence of randomly distributed aggregates forming microvoids. Besides, the film topography is dominated by a softly undulating smooth surface with the boundaries of the individual PVAc particles still visible at the surface. The original spherical particles deform, forming large boulder-like bumps, but polymer interdiffusion is not sufficient to make the inter-particle boundaries disappear due to the low drying temperature [37].

Additionally, ATR-FTIR spectroscopy of PANI-PVAc composites provides evidence of interaction between the two components. **Figure 3A** and **3B** show the FTIR spectra of virgin PANI and PVAc film compared to the spectrum of a representative composite film, *P30L70*. In the spectrum of pristine PANI, the main bands at 1559, 1476 and 1299 cm^{-1} are attributed to the stretching vibrations of C=C in quinoid ring (Q), benzenoid ring (B) and to the combination of stretching of C-N secondary aromatic amine, C=N(-

N=quinoid=N-), respectively. The shoulder at ~1599 cm^{-1} is alloted to NH^+ deformations (δ_{NH^+}). The bands characteristics of the conducting protonated salt are observed at 1245 cm^{-1} ($\nu_{C\text{-}N+}$ in the polaron structure) and 1145–52 cm^{-1} (combination of δC-H, δQ-N-B/B-NH·-B). The intensity ratio of the Q/B absorption bands, I_Q/I_B= 0.93, is close to unity, distinctive of the emeraldine form, whereas the position of the δ_{NH^+}, Q and B bands are indicative of a doping or protonation level around 0.55-0.60[36,38]. Regarding pure PVAc, the pronounced peak at 1731 cm^{-1} is assigned to the stretching vibrations of the carbonyl acetate ester group ($\nu_{C=O}$) while the bands at 1230 cm^{-1} and 1018 cm^{-1}correspond to the $\nu_{C\text{-}O\text{-}Casym}$ and $\nu_{C\text{-}O\text{-}Csym}$, respectively[39].

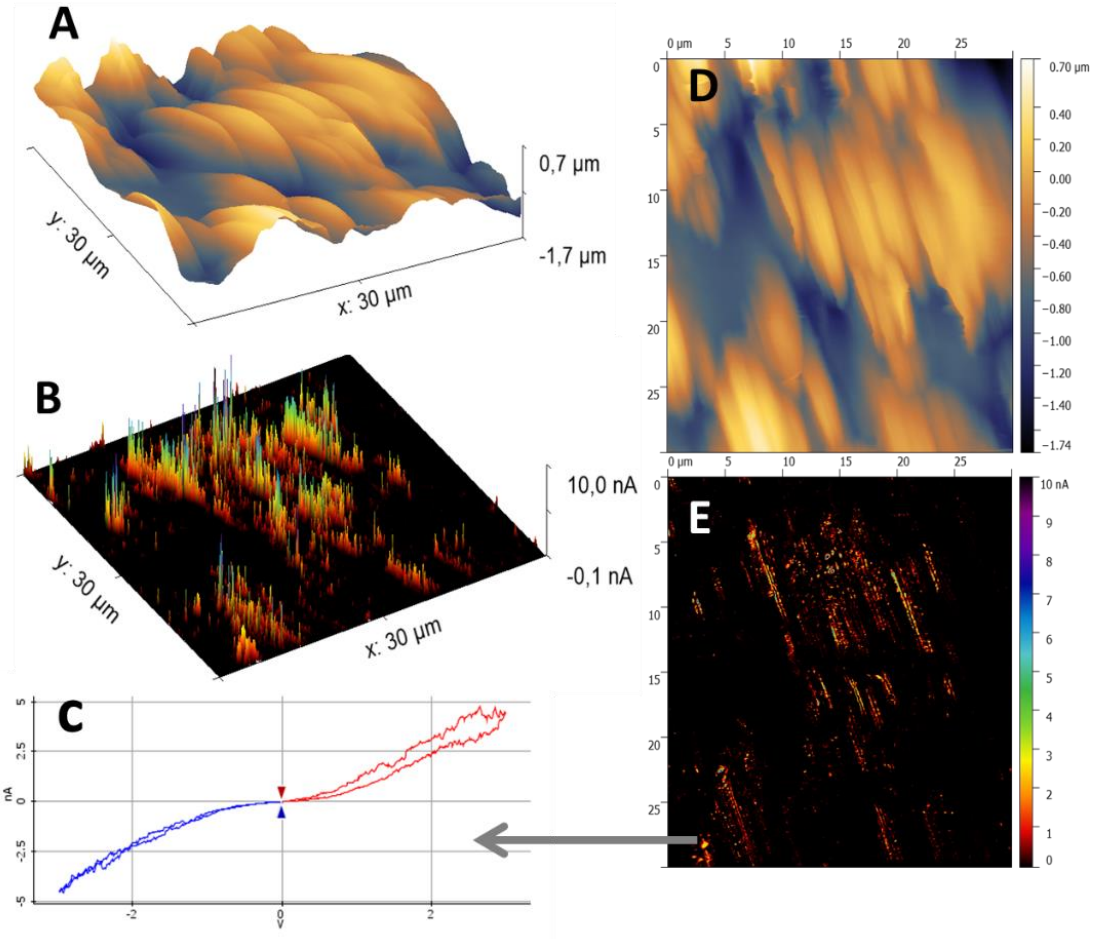

Figure 2. AFM micrographs of P30L70 obtained with a conductive tip. Two types of distinct surface structures 3D (A and B) and 2D (D and E) respectively for: A) topography; B) electrical current intensity; C) Example of the C-AFM measurement.

In all the composites spectra characteristic peaks of both components can be perceived, together with the enhancement of the intensity of PANI peaks upon increasing PANI loading (data not shown). Further, the appearance of new bands and several peak shifts are indicative of interaction between both polymers.

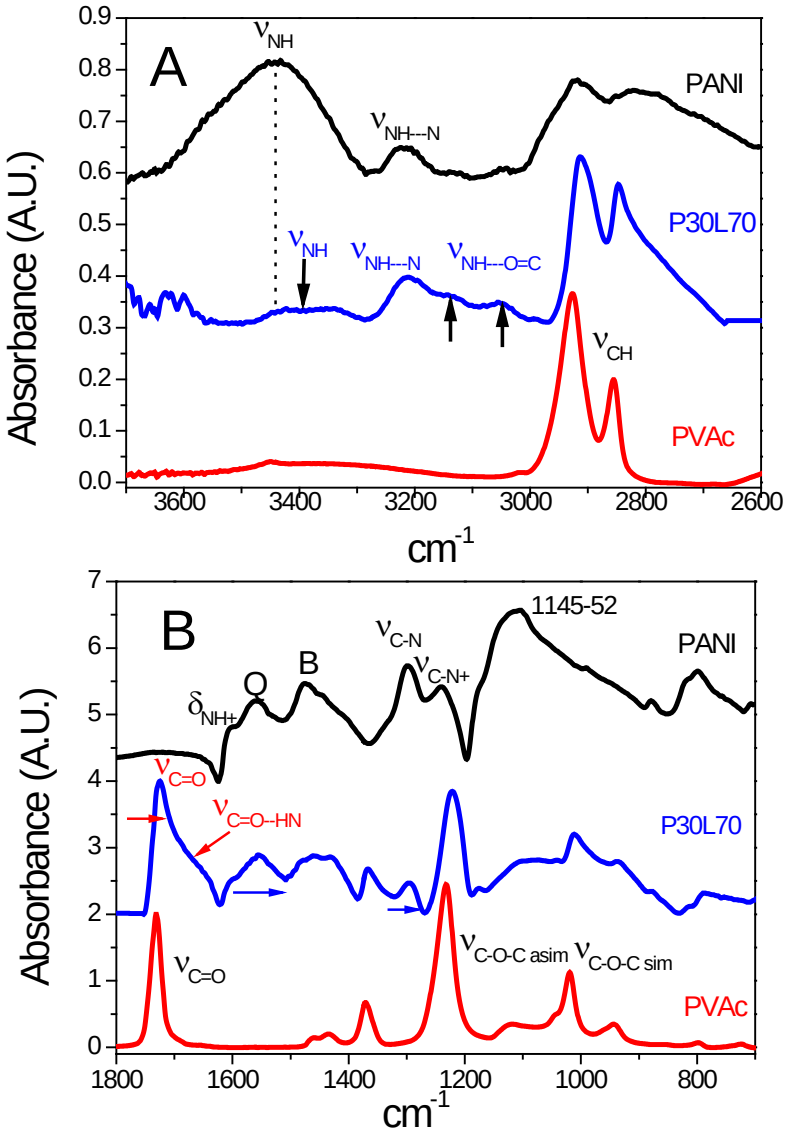

Figure 3. FTIR spectra of PANI, PVAc latex and the composite film P30L70: A) between 3700 and 2600 cm^{-1} and B) 1800 and 600 cm^{-1}.

Specifically, the PANI peaks at 3432 and 3220 cm^{-1} have been assigned to free and hydrogen-bonded (H-bonded) stretching vibrations of secondary amines NH (ν_{NH} and $\nu_{---NH<}$), respectively. The latter is due to H-bonding between amine group and protonated imine nitrogen of PANI ($\nu_{+NH\cdots N(H)<}$). However, in the FTIR spectra of the PANI-PVAc composites the former peak nearly disappears and two new small bands are detected at lower wave numbers, 3130 and 3049 cm^{-1}, as a result of H-bonding between the NH groups and the acetate groups of PVAc. The downshift of the new bands indicates that the H-bonds between the NH groups of PANI and C=O groups of the polymer matrix are stronger than H-bonds between PANI chains (**Figure 3A**). Similar

interactions have been reported between PANI and other polymers containing carbonyl groups [40–42].

Concerning PVAc, the maximum of the carbonyl stretching band ($\nu_{C=O}$) at 1731 cm^{-1} linearly downshifts with increasing PANI loading, reaching the value of 1720 cm^{-1} for composites with high PANI contents. Concurrently, the band broadens due to the gradual development of a shoulder at 1715 cm^{-1}, assigned to vibrations of bound carbonyl groups ($\nu_{C=O\text{--}HN}$) (**Figure 3B** and **Figure S1A**, Supplementary material) [43,44]. The carbonyl band is used to characterize the fraction of H-bonded carbonyl groups (f_b) by analyzing the vibrations of free ($\nu_{C=O}$) and bound ($\nu_{C=O\text{--}HN}$) carbonyl groups, as described in Supplementary material (**Figure S1B**, **Eq.S1**). As shown in **Figure 4**, f_b exponentially increases with the raise of PANI loading (R^2=0.94), reaching a constant value of 0.45 for PANI contents ≥30 wt.%.

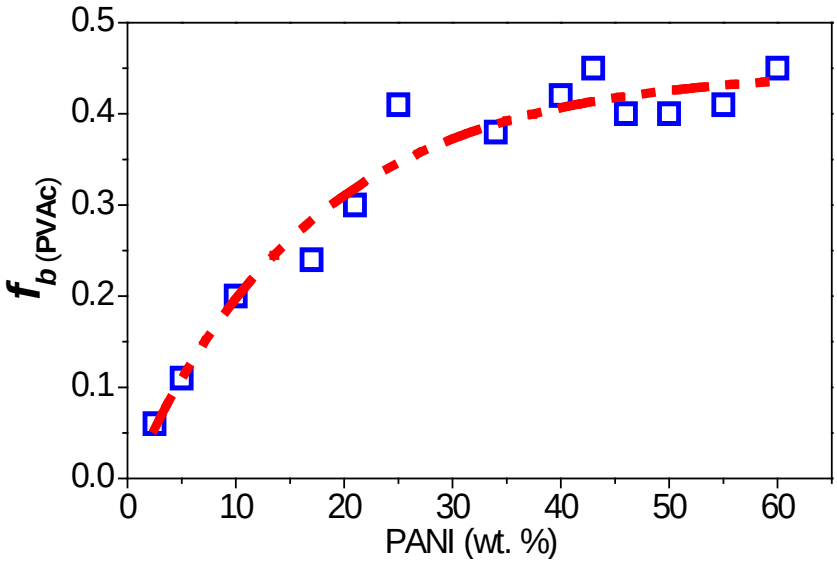

Figure 4. Fraction of bound carbonyl groups (f_b) of PVAc versus wt.% PANI from a fit of two Gaussian bands to the carbonyl region of the ATR spectra. The dashed line is an exponential fit to the data.

Taking into account the above results, H-bonding can be analyzed from the point of view of PANI chains hereafter. The PANI structural formula has 4 potential NH donor groups, whereas PVAc structural formula has 1 carbonyl acceptor group. The data of **Figure 4** mean that, on average, ≈4 NH groups of the PANI structural formula are involved in H-bonding for 5 wt.% PANI; ~2 NH groups for 10 wt.% PANI; ~1 NH group for 21 wt.% PANI and less than 1 NH group for PANI contents ≥30 wt.%.

Additionally, the upshifts of PANI bands (δ_{NH^+}, Q, B) suggest a partial deprotonation of PANI for contents below 30 wt.% (**Figure S2**). On increasing PANI loading, these bands maxima gradually downshift, reaching values similar or lower than those of pristine PANI. These results may be explained by the strong H-bonds between PANI and PVAc which, as stated in the preceding paragraph, encompass more NH groups of the PANI structural formula at low PANI contents than at higher concentrations, thus promoting a partial deprotonation in the former compositions.

XRD analysis confirms the strong dependence of the composites morphology on the PANI content (**Figure 5**).

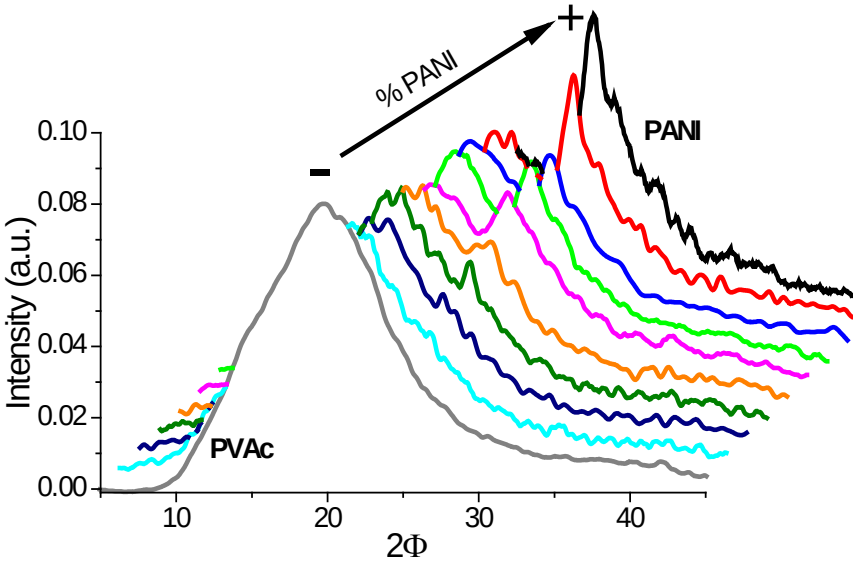

Figure 5. X-ray diffraction patterns of PVAc film, neat PANI, and PANI-PVAc composites of increasing PANI content.

The PVAc film displays the typical behaviour of an amorphous polymer, while neat PANI exhibits partial crystallinity, indicative of the orthorhombic structure of ES-I type, with the most intense reflection at 2θ = 25.6° [32]. In turn, the XRD patterns of the PANI-PVAc composites contain the characteristic features of the scattering of both polymers only for PANI contents above 20 wt.%; beyond this value, the crystallinity fraction of PANI within the composite has been estimated (**Table S1**). Both the crystallinity fraction and the intensity of the peak at 2θ =25.6° linearly increase with increasing the PANI weight fraction, approaching the value of pure PANI. No peak shifts have been observed, but the narrowing of the peak at 2θ =25.6° reflects an increase in the size of the crystals (**Table S1**). In short, the lower crystallinity of the PANI fraction at low filler contents may be enhanced by the partial deprotonation observed by FTIR, as a result

of the greater number of NH groups of the PANI structural formula involved in H-bonding compared to high PANI loadings. It is well known that the crystallinity of PANI salt decreases upon dedoping and vice versa [32].

3.2. Electrical properties

The room temperature electrical conductivities of PANI-PVAc composites, which were identical on both sides, increase from 10^{-7} to 4 S·cm^{-1} as a function of the vol.% PANI (**Figure 6**). Following the percolation theory, the lowest filler concentration for a composite with an insulating matrix to become conductive, corresponds to the so-called percolation threshold (ρ_c). At this limit concentration, a sharp increase in conductivity of several orders of magnitude occurs. For the mathematical determination of ρ_c, the data are fitted to the corresponding power law (inset **Figure 6**) [45,46]. The experimentally estimated percolation threshold (ρ_c) is ~7.5 vol.%, the effective conductivity of PANI within the matrix (σ_0) is ~ 2 S·cm^{-1} and the critical exponent t is 2.86; the latter value indicates that the conduction in this composite occurs in 3D [46].

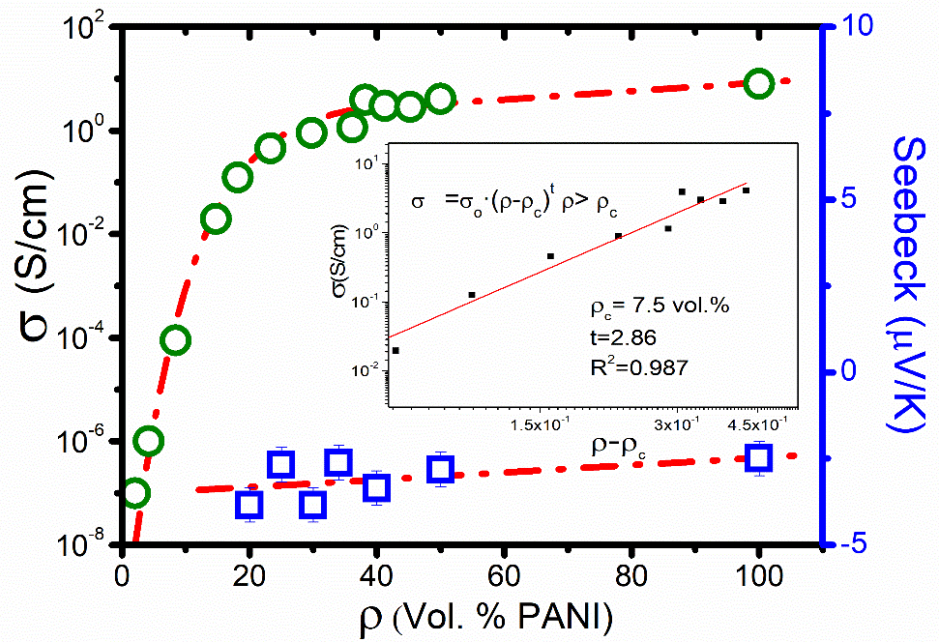

Figure 6. Composite electrical conductivity (σ) (in semi-log plot, green circles) and Seebeck coefficient (blue squares) as a function of the volume fraction of PANI(%) (ρ). The insert shows a log–log plot of the composite conductivity as a function of $\rho-\rho_c$, where σ_0 is the effective conductivity of PANI within the matrix; ρ_c is the percolation threshold and t is the critical exponent dependent on the dimensions of the lattice.

The percolation thresholds (ρ_c) of different PANI-polymer composites prepared by film casting varied from 3 to 10 vol.% [17,47,48]. By contrast, a very low ρ_c of 0.60 vol.% has

been obtained by Levin et al. for a PANI-PVAc segregated network; nonetheless, the geometry and molecular weight of PANI nanoparticles used by these authors are different than ours and the highest electrical conductivity values achieved are two orders of magnitude lower [20]. These discrepancies are not surprising since the values of ρ_c and maximum electrical conductivity reached by different CPCs are strongly dependent on the nature of the fillers, their aspect ratio and shape, filler dispersion, elastomer matrix and filler distribution in the nanocomposite [27].

In the current experiment, the strong H-bond interaction between PANI and the polymer matrix promotes a partial deprotonation of PANI and a lower crystallinity degree at low filler contents. These structural features may account for the obtained percolation threshold. Most importantly, the electrical conductivities of composites with PANI contents above 30 wt.% are similar to pristine PANI.

3.3. Thermoelectric properties

The potential of PANI-PVAc composites as organic thermoelectric materials has been investigated. Despite the significant increase in electrical conductivity, the Seebeck coefficient (α) values of the PANI-PVAc composites are similar to pure PANI (-2.5 $\mu V \cdot K^{-1}$), within experimental error (**Figure 6**, squares). Likewise, the thermal conductivities (κ) (0.4-0.5 $W \cdot m^{-1} \cdot K^{-1}$) are independent of the filler concentration for PANI contents below 40 wt.%, although they are twofold the value of pure PANI (0.22 $W \cdot m^{-1} \cdot K^{-1}$). According to previous authors and opposite to bulk semiconductors, in the case of polymer composites it is easy to enhance electrical conductivity keeping α and κ constant on increasing the filler amount [25,49]. This feature is ideal for tailoring thermoelectric properties and has been explained by the thermally disconnected, but electrically connected, junctions in the segregated conductive networks [49].

Following **Eq. 1**, ZT values are calculated using the three described parameters, σ, α and κ, at room temperature. ZT increases from $1.2 \cdot 10^{-7}$ to $1.2 \cdot 10^{-6}$ for PANI contents spanning from 25 to 50 wt.%. Namely, the ZT values of *P20L80* and *P30L70* are $1.2 \cdot 10^{-7}$ and $3.7 \cdot 10^{-7}$, respectively; the latter is an order of magnitude lower than the ZT of pristine PANI ($3.4 \cdot 10^{-6}$). Even though the experimental ZT is still low for commercial applications, the results are promising since these lightweight stretchable composites are ecofriendly, low cost and easily scalable for industrial implementation without

dimensional limitations. Apart from ZT, the global efficiency of a thermoelectric device depends on the thermodynamic efficiency and device design. From the design point of view, these flexible, low cost PANI-PVAc composites display higher versatility than nanocomposites based on inorganic particles, therefore widening potential applications, specifically in large area applications [24].

3.4. Mechanical properties

The influence of PANI on the mechanical properties of PVAc based composites was studied by tensile testing for three formulations above the percolation threshold, *P10L90, P20P80* and *P30L70.* At PANI loadings larger than 40 wt.% the composite films become brittle, probably due to the fragile behaviour of filler particles and their agglomerates. The Young modulus (*E*), the stress (σ) and strain (ε) at the break point were measured from the stress–strain curves (**Figure S3** ESI and **Table 2**).

Table 2. Summary of the characteristic degradation temperaturas of PANI, PVAc and PANI-PVAc composites taken from the minima of DTG curves and tensile parameters from the stress-strain curves.

Sample	$T_{moisture}$ (weight loss)	T_{HCl} (weight loss)	T_{10}	$T_{deacetylation}$	E (MPa)*	σ(MPa)**	ε (%)**
PANI	87 (5.2%)	235 (7.2%)	263	-	-	-	-
PVAc	-	-	365	395	0.85±0.07	1.5±0.3	492±67
P10L90	132 (1.6%)	246 (1.6%)	364	395	2.5±0.2	2.7±0.1	517±93
P20L80	138.5 (2.8%)	237 (2.8%)	354	392	5.6±0.8	2.5±0.7	302±173
P30L70	117.0 (3.2%)	240 (3.7%)	341	387	12±2	3.4±0.2	330±78

(* measured at 5 mm·min^{-1}. ** measured at 50 mm·min^{-1})

$T_{moisture}$: temperature assigned to the release of moisture and volatile components, including partial loss of HCl; **T_{HCl}:** temperature corresponding to the loss of bound HCl from deep inside PANI; **T_{10}:** temperature at which 10% of the total mass is volatilized; **$T_{deacetylation}$:** temperature of PVA_c deacetylation; ***E***: Young modulus; **σ**: stress at the break point; **ε**: strain at the break point.

Upon increasing PANI content, the composites exhibit an increase in stiffness and tensile strength compared to pure PVAc latex. The enhancement of Young modulus is expected due to the presence of rigid benzene rings in PANI chains (E_{PANI} ≈1.5-2.2 GPa and ε_{PANI} ≈5-10%) [50,51]. In addition, the strong H-bond interaction, described in the structural characterization section, enhance the interfacial adhesion between the PANI network and PVAc matrix, improving the tensile strength.

Concerning ductility, the deformation at break point of the three composites suffers a slight reduction with respect to pure latex, within the experimental error. More to the point, the relative error increases as a function of PANI content; this result reveals that the composites heterogeneity augments with higher filler amounts, owing to the agglomeration of PANI particles. Furthermore, the three composites assayed have broken without plastic deformation, confirming retention of the elastomeric nature. They all show an acceptable behaviour for their use as stretching electrically conductive elastomers. These results are encouraging, as enhancing both the tensile strength and ductility of s-CPC remains a challenge and, so far, few researchers have successfully improved these properties [28].

More importantly, stretching an electrically conductive elastomer nanocomposite often results in increased electrical resistance, owing to the permanent breakdown of the filler network. Hence, the electrical conductivity was measured before and after mechanical stretching. It decreases two orders of magnitude, to half the original value and one order of magnitude for *P10L90, P20L80* and *P30L70* films, respectively (**Figure S4**). This fact is very relevant for the electro-mechanical properties and sensor applications [27].

3.5. Thermal stability

The effect of PANI on the thermostability of the composites is appreciated by the change of position of the main weight losses in the TGA and DTG curves (**Figure S5**). PANI shows three main weight loss stages in the temperature ranges 40-155, 155-318 and 318-700 °C, assigned to release of moisture and volatile components and partial loss of HCl acting as dopant, to the loss of bound HCl from deep inside the bulk of the PANI clusters, followed by degradation of PANI chains, respectively [36]. By contrast, PVAc latex is thermally stable up to 250 °C. The thermal degradation occurs in three steps ranging 250-470, 470-537 and 537-615 °C corresponding to deacetylation

(removal of the pendant acetate ester involving the replacement of the acetyl group, CH_3CO, with an hydrogen atom yielding an hydroxyl group), chain scission reactions of deacetylated vinyl acetate entities and ethylene units, respectively [52].

The relative thermal stability of the PANI-PVAc films is evaluated by comparing decomposition temperatures at various percentage weight losses, which are presented in **Table 2**. The three composites exhibit shifts of the moisture and HCl evaporation of the PANI phase to higher temperatures, with reduction of weight losses, as compared with those of neat PANI; on the contrary, T_{10} and the deacetylation step of PVAc move to lower temperatures for *P20L80* and *P30L70*, compared with those of pure PVAc latex, owing both to the increase in moisture and HCl contents and to the catalytic effect of HCl acid on the deacetylation reaction [53]. At any rate, the thermostability decrease is negligible for *P10L90.*

3.6. Electromechanical response

The PANI-PVAc composites present piezoresistive properties for PANI contents up to 30 wt.%. The piezoresistive response was analysed for *P10L90, P20L80* and *P30L70.* They all follow the typical behaviour: the electrical resistance increases while the film is stretched and decreases when the composite recovers to the initial deformation [54]. As an example, **Figure 7A** depicts the electromechanical performance of a *P10L90* film for 5% of deformation at 5 $mm \cdot min^{-1}$. Besides, the three formulations display excellent linear behaviour between mechanical stimulus and electrical resistance variation which allows GF calculation, as illustrated in **Figure 7B**. Additionally, the electromechanical behaviour of the three composites as a function of deformation, velocity and number of cycles is presented in **Figure 8A-C**.

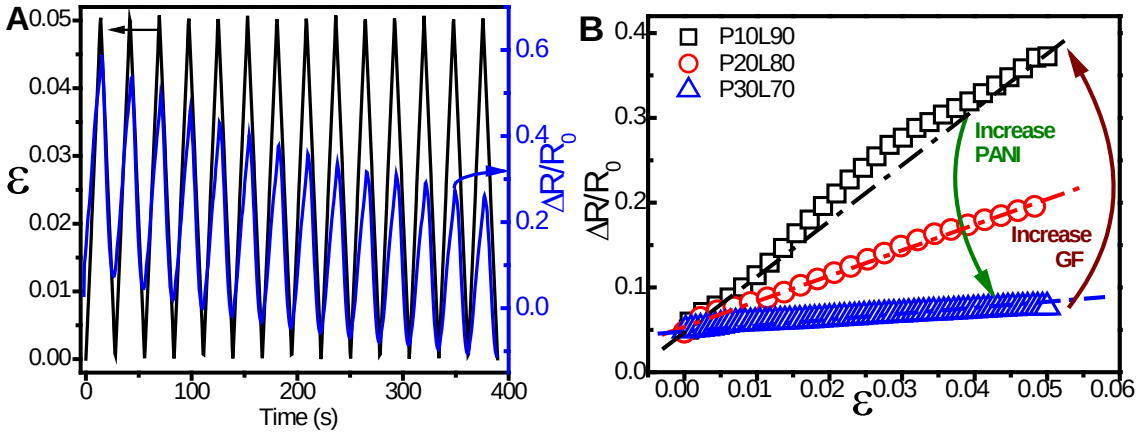

Figure 7. Illustration of electromechanical behaviour: A) Cycles for P10L90 for 5% of deformation at 5 mm·min^{-1} and B) GF sensitivity (**Eq. 3**) as function of the PANI content in the composites.

The electromechanical sensibility or gauge factor (GF) (**Eq. 3**) declines upon increasing PANI content (**Figure 7B**). *P10L90, P20L80* and *P30L70* films have GF ranges of 7-12, 1-6 and 0.5-1, respectively, depending on the experimental conditions (**Figure 8A** and **B**). As previously reported, the piezoresistive effect is larger near the percolation threshold, due to the tenuous connections of the conductive network that are more easily disconnected when stretched [20,55]. Accordingly, as has been observed in , the electrical conductivity of *P10L90 i*s near the percolation threshold. On the other hand, the electrical conductivities of *P20L80* and *P30L70* lie above-the electrical threshold in the curve.

This enhancement in sensitivity with decrease of PANI loadings is apparently in contrast with the results obtained by Levin et al [20] for analogous PANI-PVAc s-CPC. The reason for this discrepancy is that all the formulations assayed by these authors are well above the percolation threshold. Quite the reverse, our results are similar to most carbon based CPCs [54].

More to the point, the GF of *P30L70* is mainly determined by the geometrical piezoresistive response (1+2*v*) for all experimental conditions (**Eq. 3**), whereas in the case of *P20L80* only for deformations less than 5% [35] (**Figure 8A-C**). On the contrary, the piezoresistive effect of *P10L90* film is mainly influenced by an intrinsic contribution of the electrical resistance variation upon mechanical deformation. Its high GF is comparable to literature reports for elastomer based nanocomposites and larger than classical metal-foil strain gauges [13,20].

Besides the macroscopic percolation theory, several conductive mechanisms explain the electrical response upon mechanical deformation in conductive nanocomposites[27]. Within the PANI crystalline region, conductivity depends on the ability of the charge carriers to move along the polymer backbone (intra-chain mechanism) and between the polymer chains (inter-chain coupling)[10]. Besides, these "crystalline islands" form metallic regions of higher conductivity, modeled as spheres of metal grains, separated by amorphous insulating regions. Charge transport between conducting grains may be explained by one or more theoretical models such as resonance tunneling, hopping conduction among others[56]. Both the intermolecular distance between the PANI chains in the crystalline domains and separation distance of the metallic grains, which are critical for conduction, increase when the material is deformed by uniaxial stress in tension, increasing electrical resistance.

From another point of view, *P20L80* and *P30L70* show suitable electromechanical properties up to strains as large as 20% of deformation at several velocities; by contrast, *P10L90* only shows electromechanical response up to 10%, due to the low PANI content. Moreover, for *P10L90,* the *GF* variation with strain and velocity is erratic, but it achieves a maximum value at 10% deformation and at the highest speed of 10 $mm \cdot min^{-1}$ (**Figure 8A-B**). When strain is applied, conductivity fluctuation is greater at low conductive filler concentrations due to destruction and formation of conductive paths [54].

Besides, *GF* steadily increases in *P20L80* and *P30L70* with the augment of the external stimulus, both deformation and velocity. The enhancement of the GF with strain is higher for *P20L80* than for *P30L70*. On the basis of the described conduction mechanism, the lower crystallinity degree of PANI in *P20L80* compared to *P30L70*, decreases the overall conductivity as well as the stiffness, increasing the mobility of PANI chains and, as a consequence, leading to a larger piezoresistive response.

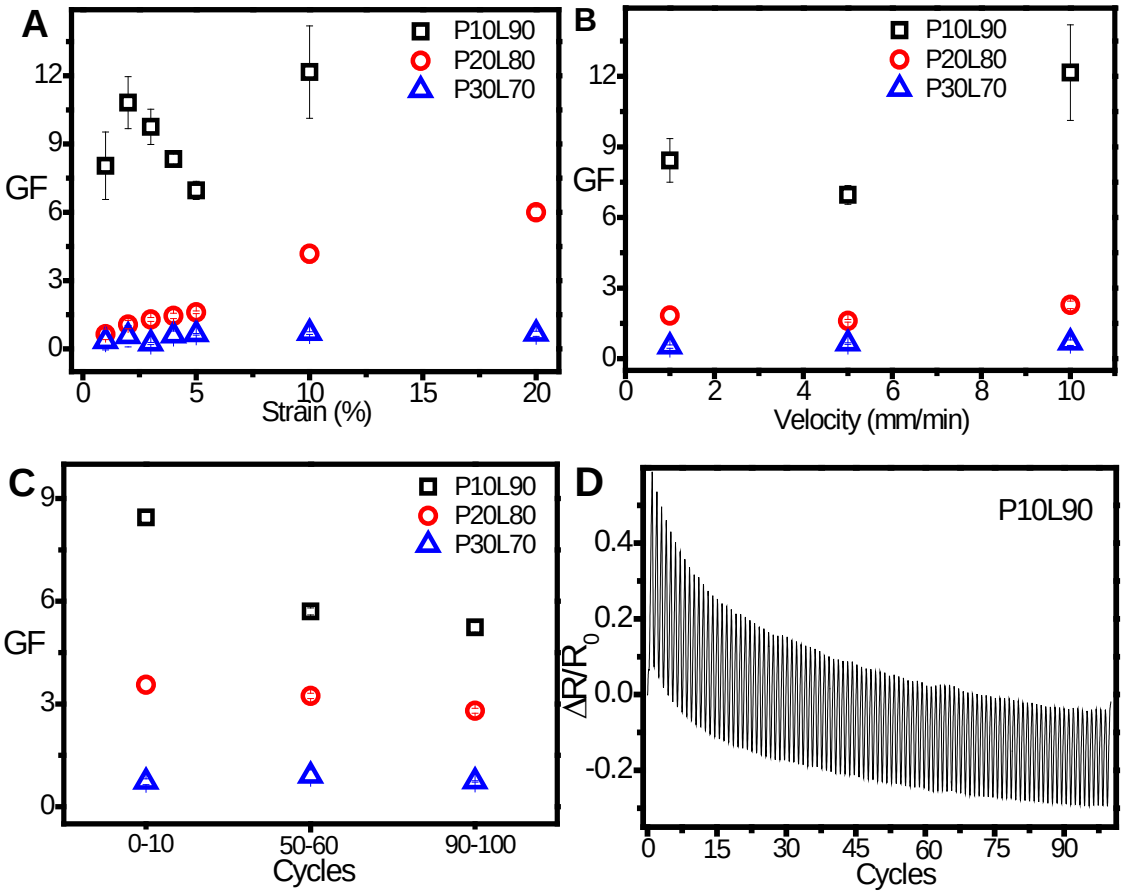

Figure 8. Piezoresistive sensitivity of PANI-PVAc composites: A) GF of P10L90 up to 10% strain and P20L80 and P30L70 up to 20% strain at 5 mm·min^{-1}; B) GF up to 5% of deformation at several velocities (1, 5 and 10 mm·min^{-1}); C) GF as a function of the number of cycles; D) Cycle stability of the piezoresistive response of P10L90 at 5% deformation and 5 mm·min^{-1} over 100 cycles.

Finally, experiments were performed as function of the number of stretching cycles to assess the stability and fatigue of the PANI-PVAc composites. As can be observed in **Figure 8C-D**, the electrical resistance variations decrease with increasing the number of cycles in the electromechanical measurements, tending to stabilize after around 50 cycles. Nevertheless, the decline is more abrupt for *P10L90*, which decreases from ≈8 to 5 after 100 cycles and negligible for *P30L70*. Near the percolation threshold, fewer conductive channels are formed and, thus, repeated deformation-relaxation cycles result in a permanent damage to the network with possible disrupture of H-bonds between PANI and the matrix. This sensitivity loss is a common feature of thermoplastic elastomer-based CP nanocomposites [20].

3.7. Thermoresistive properties

Conductive networks within a composite film also dominate the resistance-temperature behaviour. The PANI-PVAc composites, *P10L90, P20L80* and *P30L70*,

present thermoresistive properties. The electrical resistance decreases linearly with increasing temperature and vice versa, a clear indicator of negative temperature coefficient (NTC) behaviour. The resistivity dependence on temperature shows intrinsic semiconducting properties, which is dominated by thermally activated charge carriers [1]. The literature reports analogous thermal properties for PANI-DBSA samples [36].

Similar to what was observed for the GF, the thermal sensitivity of PANI-PVAc composites declines with increasing PANI content. This is a common behaviour as a lower carrier density is preferred to achieve higher sensitivity of NTC thermistors [1]. As an example, the results of *P10L90* films corresponding to four heating/cooling cycles from 20 to 40 °C and 20 to 100 °C at 10 °C·min^{-1} are depicted in **Figure 9A** and **B**, respectively. The thermoresistive sensibility (S) (**Eq. 4**) is near 0.25 ±0.06 %· °C^{-1} and 0.17 ±0.05 %· °C^{-1} for 20 to 40 °C and 20 to 100 °C.

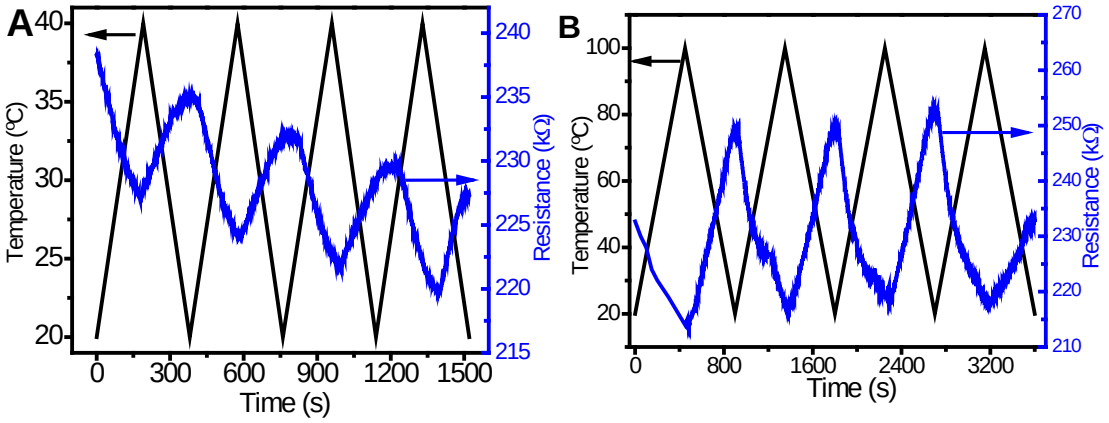

Figure 9. Thermoresistive behaviour of P10L90 from 20 to 40 °C (A) and from 20 to 100 °C (B) at 10 °C·min^{-1}.

Good repeatability is observed, although a drop in resistance of ≈7 KΩ is detected at the end of the fourth cycle after heating to 40 °C and an increase of ≈4 KΩ after heating to 100 °C. The former observation may be due thermal doping, or to transformation of some unbound water and unbound HCl to bound forms as dopants induced by thermal energy [57]. By contrast, the latter result can be explained by the partial evaporation of moisture and volatile components (HCl) at 100 °C, thus favouring PANI deprotonation, as described in TGA experiments.

4. Conclusions

PANI-PVAc composites have been prepared by a simple, eco-friendly and scalable latex technology. Morphological and microstructural analysis revealed a 3D PANI segregated network with strong H-bonding between the polymers and differences in the doping level and crystallinity of PANI on increasing its loading. Composite films exhibit an electrical percolation threshold (ρ_c) around 7.5% and a maximum conductivity similar to pristine PANI. Specifically, films with PANI contents ranging from 10 to 30 wt.% are useful for applications involving electrical conductivity and elastomeric performance, showing satisfactory electromechanical and thermoresistive properties.

Both the GF and thermal sensitivity of PANI-PVAc composites decline with increasing PANI content, displaying the largest values near the electrical percolation threshold. Thus, composites with 10 wt.% PANI present the highest GF, similar to literature reports for elastomeric composites[13,27,58] and outperforming metal-foil strain gauges; besides, the thermal sensitivity in the temperature range 20-40 °C is suitable for flexible and wearable temperature sensors intended for monitoring human health [4]. By contrast, films with 20 wt.% and 30 wt.% PANI present the best compromise between thermoelectric properties (ZT) and mechanical behaviour.

In short, by adjusting the composition ratio of the PANI-PVAc composites it is possible to tune their thermoelectric, electromechanical and thermoresistive properties, making them potential candidates for lightweight, stretchable electronics that could be employed as temperature and strain sensors for wearable devices.

Supplementary material

1. FTIR

The carbonyl band is used to characterize the amount of PVAc bound to the NH groups of PANI by analyzing the vibrations of free ($\nu_{C=O}$) and bound ($\nu_{C=O\cdots HN}$) carbonyl groups. After subtraction of the baseline, the intensity of the two peaks at 1730 and 1715 cm^{-1}, respectively, is estimated by fitting two Gaussians to the data (**Figure S1B**).

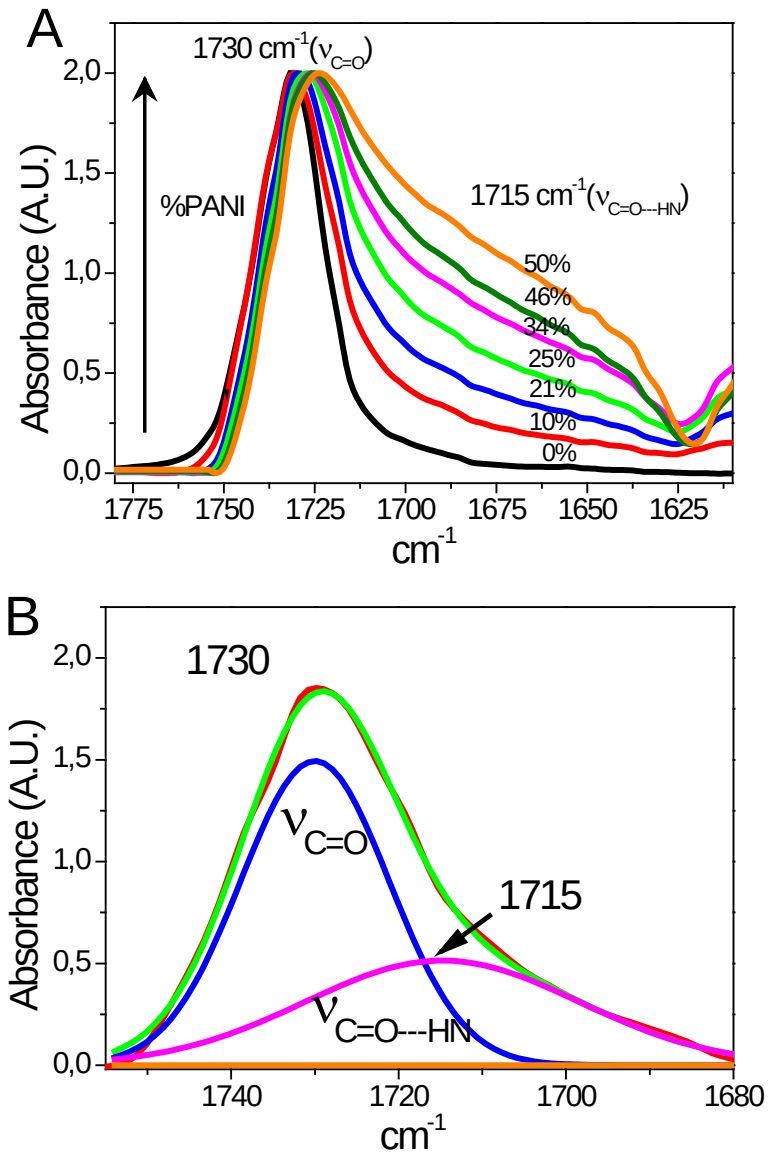

Figure S1. A) Carbonyl region of the FTIR absorption spectra of composites of increasing PANI concentration. The intensities of the spectra are normalized with respect to the peak of free C=O; B) Fit of two Gaussians to the data for the *P30L70* film. The areas under the two peaks are assigned to bound ($\nu_{C=O\cdots HN}$) and free ($\nu_{C=O}$) carbonyl groups.

The areas under the peak correspond to the relative amount of $C{=}O_{bound}$ (A_b) and $C{=}O_{free}$ (A_f). Nevertheless, here the fraction of H-bonded carbonyl groups (f_b) is roughly calculated by **Eq. S1**, where *a* is the ratio of the molar absorption coefficients. A value of 1.5 was taken for the *a* ratio, according to previous studies[60].

$$f_b = \frac{A_b\,/a}{A_b/a + A_f} \qquad (\mathbf{S1})$$

From another point of view, the locations of the δ_{NH^+}, Q and B bands are indicative of the doping level of PANI[36,38]. At low PANI contents, the band maxima are observed at higher wavenumbers compared to pure PANI. On increasing the PANI content, the bands δ_{NH^+} and B gradually downshift to wavenumbers similar to pristine PANI (**Figure S2A-B**). Concerning the Q band, it is located at higher wavenumbers than pure PANI for composites with PANI contents below 34% (shifting from 1575 to 1565 cm^{-1} on increasing PANI from 5 to 25 %wt.); it further downshifts to 1556 cm^{-1} in the range spanning from 34 to 46% wt and finally, decreases to 1541 cm^{-1} for PANI contents ≥50 %wt (**Figure S2A**). At PANI loadings below 30 % wt, a probable partial deprotonation may explain the band locations. A gradual increase in the doping level, along with H-bonding with PVAc, accounts for further downshift [61].

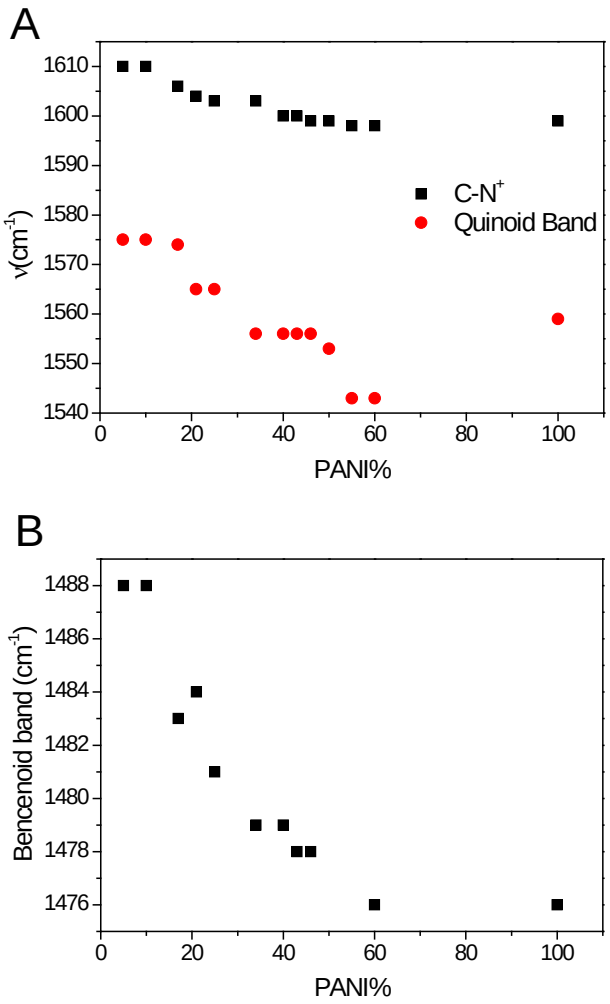

Figure S2. Shifts of PANI FTIR bands upon increasing the PANI %wt in PANI-PVAc composites: A) wanumbers of the $\delta_{NH}{}^{+}$ (squares) and Quinoid band (Q) (circles) and B) bencenoid band (B).

2. XRD

The XRD pattern of neat PANI exhibits partial crystallinity with characteristic reflections at 2θ = 9.3, 15.1, 20.5, 25.6, 27.1 and 30.0° and a broad asymmetric scattering of the amorphous phase. These structural features are indicative of the orthorhombic structure of ES-I type. The most intense reflection at 2θ = 25.6° is due to periodicity perpendicular to the polymer chain [32].

The same PANI features are observed for composites with PANI contents ≥ 17% wt. In order to evaluate the PANI phase contribution in the composite films, the normalized diffractogram of amorphous PVAc was subtracted from the normalized composites patterns. The obtained difference patterns were used to estimate the degree of crystallinity of the PANI phase (X_c). The intensities of the peak at 2θ= 25.6°, the

crystallite sizes (L), estimated from the widths of the peak at 25.6°, and X_c are presented in **Table S1**.

Table S1. Intensity of the peak at 2θ= 25.6°, crystallite size (L) estimated from the width of the peak at 25.6° and degree of crystallinity (X_c) of the PANI phase within the composites.

PANI (wt %)	Intensity	L(x10^{-10} m)	X_c (%)
17	0.011	-	19
21	0.021	-	24
25	0.015	-	23
34	0.024	29.8	30
40	0.033	34.2	37
43	0.033	47.6	39
46	0.035	51.3	37
55	0.057	60.4	48
100	0.068	57.3	57

3. Mechanical properties

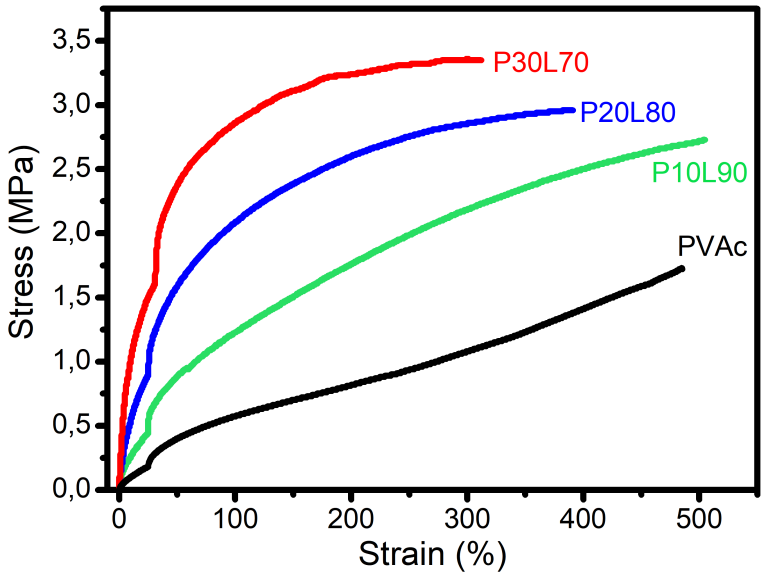

Figure S3. Stress-strain curves until rupture of pure PVAc and PANI-PVAc composites: *P10L90*, *P20L80* and *P30L70*

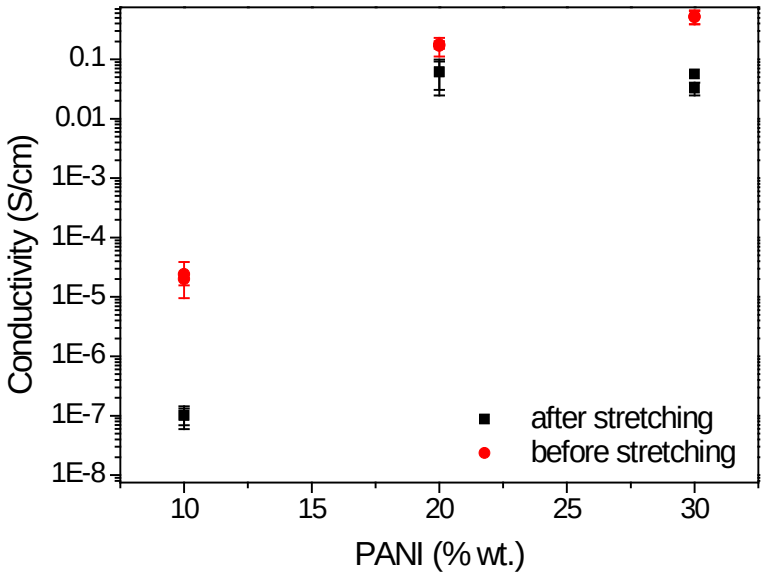

Figure S4. Changes in conductivity of *P10L90*, *P20L80* and *P30L70* composites after tensile testing.

4. Thermal stability

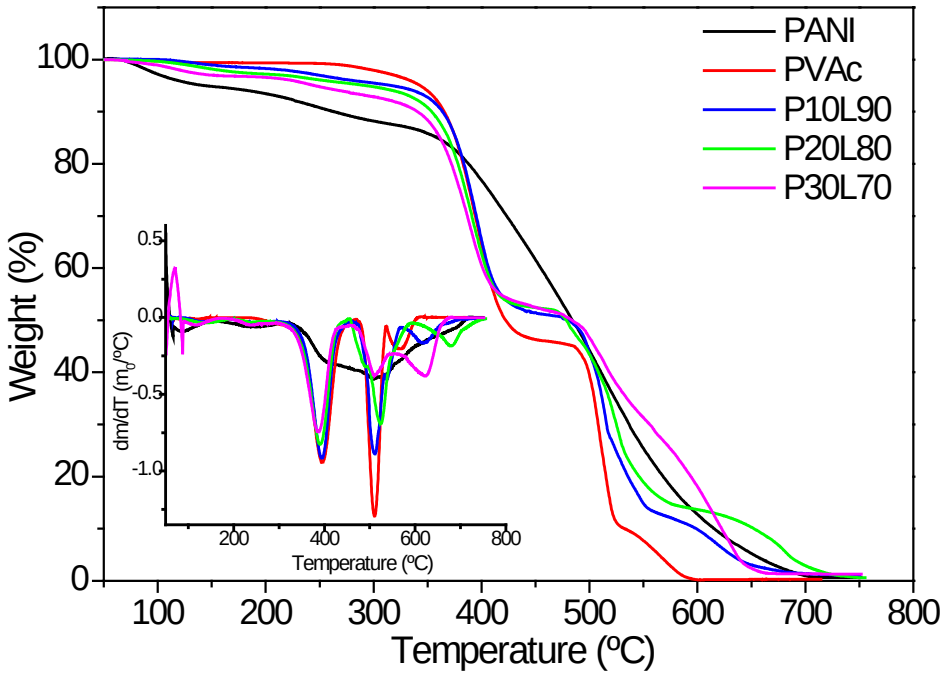

Figure S5. TGA and DTG (inset) curves of PANI-HCl, PVAc and PANI-PVAc composites: *P10L90, P20L80* and *P30L70*.

References

1. Yan, C., Wang, J. & Lee, P. S. *ACS Nano* 9**,** (2015), 2130.

2. Hong, S. Y., Lee, Y. H., Park, H., Jin, S. W., Jeong, Y. R., Yun, J., You, I., Zi, G. & Ha, J. S. *Advanced Materials* 28**,** (2016), 930.

3. Russ, B., Glaudell, A., Urban, J. J., Chabinyc, M. L. & Segalman, R. A. *Nature Reviews Materials* 1**,** (2016), 16050.

4. Takei, K., Honda, W., Harada, S., Arie, T. & Akita, S. *Advanced Healthcare Materials* 4**,** (2015), 487.

5. Wang, B., Huang, W., Chi, L., Al-Hashimi, M., Marks, T. J. & Facchetti, A. *Chemical Reviews* 118**,** (2018), acs. chemrev.8b00045.

6. Yang, Y. & Gao, W. *Chemical Society Reviews* (2018), doi:10.1039/C7CS00730B

7. Khandelwal, V., Sahoo, S. K., Kumar, A. & Manik, G. *Composites Part B: Engineering* 136**,** (2018), 149.

8. Alonso, E., Faria, M., Mohammadkazemi, F., Resnik, M., Ferreira, A. & Cordeiro, N. *Carbohydrate Polymers* 183**,** (2018), 254.

9. Hamid Elsheikh, M., Abdulameer Shnawah, D., Mohd Sabri, M. F., Mohd Said, S. B., Haji Hassan, M., Ali Bashir, M. B. & Mohamad, M. *Renewable and Sustainable Energy Reviews* 30**,** (2014), 337.

10. Falletta, E., Costa, P., Della Pina, C. & Lanceros-Mendez, S. *Sensors and Actuators A: Physical* 220**,** (2014), 13.

11. Geethalakshmi, D., Muthukumarasamy, N. & Balasundaraprabhu, R. *Optik* 125**,** (2014), 1307.

12. Xu, S., Yan, J., Feng, Z., Qiu, S., Shao, F., Li, M., Yu, M. & Qiu, H. *Thin Solid Films* 608**,** (2016), 44.

13. Gong, X. X., Fei, G. T., Fu, W. B., Fang, M., Gao, X. D., Zhong, B. N. & Zhang, L. De. *Organic Electronics: physics, materials, applications* 47**,** (2017), 51.

14. Ray, S., Easteal, A. J., Cooney, R. P. & Edmonds, N. R. *Materials Chemistry and Physics* 113**,** (2009), 829.

15. Abdel Rehim, M. H., Youssef, A. M., Al-Said, H., Turky, G. & Aboaly, M. *RSC Advances* 6**,** (2016), 94556.

16. Gajendiran, M., Choi, J., Kim, S. J., Kim, K., Shin, H., Koo, H. J. & Kim, K. *Journal of Industrial and Engineering Chemistry* 51**,** (2017), 12.

17. Del Castillo-Castro, T., Castillo-Ortega, M. M. & Herrera-Franco, P. J. *Composites Part A: Applied Science and Manufacturing* 40**,** (2009), 1573.

18. Teixeira, J., Horta-Romarís, L., Abad, M. J., Costa, P. & Lanceros-Méndez, S. *Materials and Design* 141**,** (2018), 1.

19. Barra, G. M. O., Matins, R. R., Kafer, K. A., Paniago, R., Vasques, C. T. & Pires, A. T. N. *Polymer Testing* 27**,** (2008), 886.

20. Levin, Z. S., Robert, C., Feller, J. F., Castro, M. & Grunlan, J. C. *Smart Materials and Structures* 22**,**

(2013), 15008.

21. Micolini, C., Holness, F., Johnson, J. & Price, A. *Sensors* 17**,** (2017), 2768.

22. Hong, S. Y., Oh, J. H., Park, H., Yun, J. Y., Jin, S. W., Sun, L., Zi, G. & Ha, J. S. *NPG Asia Materials* 9**,** (2017), 1.

23. Du, Y., Shen, S. Z., Cai, K. & Casey, P. S. *Progress in Polymer Science* 37**,** (2012), 820.

24. Culebras, M., Gómez, C. & Cantarero, A. *Materials* 7**,** (2014), 6701.

25. Dey, A., Bajpai, O. P., Sikder, A. K., Chattopadhyay, S. & Shafeeuulla Khan, M. A. *Renewable and Sustainable Energy Reviews* 53**,** (2016), 653.

26. Tkalya, E. E., Ghislandi, M., de With, G. & Koning, C. E. *Current Opinion in Colloid and Interface Science* 17**,** (2012), 225.

27. Guo, B., Tang, Z. & Zhang, L. *Progress in Polymer Science* 61**,** (2016), 29.

28. Pang, H., Xu, L., Yan, D. X. & Li, Z. M. *Progress in Polymer Science* 39**,** (2014), 1908.

29. Park, H. W., Kim, T., Huh, J., Kang, M., Lee, J. E. & Yoon, H. *ACS Nano* 6**,** (2012), 7624.

30. Horta-Romarís, L., González-Rodríguez, M. V., Lasagabáster, A., Rivadulla, F. & Abad, M.-J. *Synthetic Metals* 243**,** (2018), 44.

31. Wojdyr, M. *Journal of Applied Crystallography* 43**,** (2010), 1126.

32. Pouget, J. P., Jozefowicz, M. E., Epstein, A. J., Tang, X. & MacDiarmid, A. G. *Macromolecules* 24**,** (1991), 779.

33. UNE-EN ISO 11357-4. (2014),

34. Costa, P., Nunes-Pereira, J., Oliveira, J., Silva, J., Moreira, J. A., Carabineiro, S. A. C., Buijnsters, J. G. & Lanceros-Mendez, S. *Composites Science and Technology* 153**,** (2017), 241.

35. Gonçalves, B. F., Oliveira, J., Costa, P., Correia, V., Martins, P., Botelho, G. & Lanceros-Mendez, S. *Composites Part B: Engineering* 112**,** (2017), 344.

36. Horta-Romarís, L., Abad, M.-J., González-Rodríguez, M. V., Lasagabáster, A., Costa, P. & Lanceros-Méndez, S. *Materials & Design* 114**,** (2017), 288.

37. Patel, A. A., Feng, J. R., Winnik, M. A., Vancso, G. J. & Mcbain, C. B. D. *Polymer* 37**,** (1996), 5577.

38. Trchová, M., Šeděnková, I., Tobolková, E. & Stejskal, J. *Polymer Degradation and Stability* 86**,** (2004), 179.

39. D'Amelia, R. P., Gentile, S., Nirode, W. F. & Huang, L. *World Journal of Chemical Education, Vol. 4, 2016, Pages 25-31* 4**,** (2016), 25.

40. Moon, H. & Park, J. *Journal of Polymer Science Part A: Polymer Chemistry* 36**,** (1997), 1431.

41. Ogurtsov, N. A., Noskov, Y. V, Fatyeyeva, K. Y., Ilyin, V. G., Dudarenko, G. V & Pud, A. A. *The Journal of Physical Chemistry B* 117**,** (2013), 5306_5314.

42. Tomar, A. K., Mahendia, S. & Kumar, S. 2**,** (2011), 327.

43. Füllbrandt, M., Purohit, P. J. & Schönhals, A. *Macromolecules* 46**,** (2013), 4626.

44. Dopico-García, M. S., Ares, a., Lasagabáster-Latorre, a., García, X., Arboleda, L. & Abad, M. J. *Synthetic Metals* 189**,** (2014), 193.

45. Crawford, J. D. *Reviews of Modern Physics* 63**,** (1991), 991.

46. Weber, M. & Kamal, M. R. *Polymer Composites* 18**,** (1997), 711.

47. Beadle, P., Armes, S. P., Gottesfeld, S., Mombourquette, C., Houlton, R., Andrews, W. D. & Agnew, S. F. *Macromolecules* 25**,** (1992), 2526.

48. Wu, X., Lu, C., Xu, H., Zhang, X. & Zhou, Z. *Applied Materials & Interfaces* 6**,** (2014), 21078.

49. Yu, C., Kim, Y. S., Kim, D. & Grunlan, J. C. *Nano Letters* 8**,** (2008), 4428.

50. Meixiang, Wan; Lijuan, Liu; Jun, W. *Chinese Journal of Polymer Science* 16**,** (1998),

51. Valentová, H. & Stejskal, J. *Synthetic Metals* 160**,** (2010), 832.

52. Rimez, B., Rahier, H., Van Assche, G., Artoos, T. & Van Mele, B. *Polymer Degradation and Stability* 93**,** (2008), 1222.

53. Monteiro, E. C. & Thaumaturgo, C. *Composites Science and Technology* 57**,** (1997), 1159

54. Kanoun, O., Müller, C., Benchirouf, A., Sanli, A., Dinh, T., Al-Hamry, A., Bu, L., Gerlach, C. & Bouhamed, A. *Sensors* 14**,** (2014), 10042.

55. Ferrreira, A., Rocha, J. G., Ansón-Casaos, A., Martínez, M. T., Vaz, F. & Lanceros-Mendez, S. *Sensors and Actuators, A: Physical* 178**,** (2012), 10.

56. Lin, Y. F., Chen, C. H., Xie, W. J., Yang, S. H., Hsu, C. S., Lin, M. T. & Jian, W. Bin. *ACS Nano* 5**,** (2011), 1541.

57. Chen, T., Dong, C., Li, X. & Gao, J. *Polymer Degradation and Stability* 94**,** (2009), 1788.

58. Costa, P., Silvia, C., Viana, J. C. & Lanceros Mendez, S. *Composites Part B: Engineering* 57**,** (2014), 242.

59. Yang, J. & Weng, B. *Synthetic Metals* 159**,** (2009), 2249.

60. Kuo, S.-W., Chan, S.-C. & Chang, F.-C. *Polymer* 43**,** (2002), 3653.

61. Yuan, N. Y., Ma, F. F., Fan, Y., Liu, Y. B. & Ding, J. N. *Composites Part A: Applied Science and Manufacturing* 43**,** (2012), 2183.

CAPÍTULO 6:

Conclusiones

CONCLUSIONES

Durante el desarrollo del trabajo de tesis, se han diseñado y caracterizado nuevos polímeros intrínsecamente conductores o compuestos conductores basados en polianilinas, con el objetivo de obtener materiales con un buen balance entre sus propiedades eléctricas, termoeléctricas o mecánicas y su coste. Además, se ha buscado el desarrollo de materiales más sostenibles y respetuosos con el medio ambiente, que pudiesen ser utilizados en la fabricación de sensores y/o generadores termoeléctricos. Los resultados obtenidos en el estudio pueden ser resumidos en las siguientes conclusiones:

1. Se han sintetizado cuatro tipos de polianilinas a través de polimerización química oxidativa, usando rutas de síntesis sencillas, directa e indirecta: PANI dopado con HCl y PANI dopado con DBSA, ambos por síntesis directa; así como PANI dopado con DBSA y PANI dopado con NaSIPA, por síntesis indirecta través del procedimiento dedoping-redoping. Se observaron cambios característicos en la morfología, orden estructural, estado de oxidación, nivel de dopaje, así como en los perfiles de degradación térmica de las PANIs obtenidas, en función del tipo de síntesis y dopante, todos ellos aspectos clave que explican la conductividad eléctrica de los materiales y su dependencia con la temperatura.
2. Las PANIs dopadas con DBSA, obtenidas por las rutas directa e indirecta, mostraron una mejor retención de conductividad eléctrica durante los ciclos de envejecimiento térmico, revelando su utilidad para fabricar sensores de temperatura.
3. Se evaluó la eficiencia termoeléctrica de las PANIs dopadas con DBSA y NaSIPA a través de rutas indirectas, en función de su morfología y concentración de dopante. Los resultados muestran que la PANI-DBSA con altos niveles de dopaje y una morfología en capas bien definida, presenta una alta conductividad eléctrica y un coeficiente Seebeck constante (en el rango de temperaturas estudiado), lo que maximiza su eficiencia termoeléctrica (ZT). En cambio, la PANI-NaSIPA presenta un bajo nivel de dopaje debido a su capacidad para formar dímeros, trímeros y tetrámeros en disolución, y por tanto, baja conductividad eléctrica, pero un coeficiente Seebeck más alto que la anterior. Estos datos

prueban su utilidad en la fabricación de generadores termoeléctricos para aplicaciones cercanas a la temperatura ambiente.

4. El estudio de los mecanismos de conducción eléctrica de las polianilinas mostró que la PANI-DBSA presenta un comportamiento tipo *hopping,* con una concentración de huecos entorno al 0,49, mientras que la PANI-NaSIPA presenta un régimen difusivo, entre 200-350K, en el que la densidad de portadores estimada es de $3 \cdot 10^{21}$ e/cm^3.
5. Con el objetivo de obtener materiales flexibles y baratos, que presentaran buenas propiedades eléctricas y piezorresistivas, se desarrollaron compuestos flexibles de PANI-HCl y PVAc, a través de la tecnología látex, un procedimiento sencillo, respetuoso con el medio ambiente y escalable a nivel industrial. El análisis morfológico y microestructural de los compuestos, mostró la formación de una red segregada tridimensional de partículas de PANI en la matriz de látex, con fuertes enlaces de hidrógeno entre polímeros. Las propiedades de dicha red varían en función del contenido en PANI y la cristalinidad de los films. La concentración umbral de percolación eléctrica está alrededor del 7,5% en masa de PANI. Al aumentar el contenido de PANI en el compuesto hasta un 30% en masa, la conductividad eléctrica alcanzó valores similares a la polianilina de partida, con la ventaja de que los compuestos PANI/Látex son más flexibles y más baratos.
6. Se evaluaron las propiedades piezorresistivas y termorresistivas de los films de PVAc con contenidos de PANI-HCl entre el 10-30%. El estudio concluyó que los compuestos con un 10% en masa de PANI presentan el valor más alto de Gauge Factor, además de que su sensibilidad térmica, entre 20-40°C, los hace adecuados para la fabricación de sensores de temperatura flexibles y portátiles, que pueden usarse para control de la salud. Por el contrario, los films con 20-30% en masa de PANI presentaron un mejor compromiso entre propiedades termorresistivas y mecánicas.

ANEXO I:

Financiación recibida

Los autores agradecen la financiación a la Xunta de Galicia-FEDER (Programa de consolidación y estructuración de unidades de investigación competitivas (GRC2014/036).

Además, se agradece el apoyo financiero de la Agrupación Europea de Cooperación Territorial Galicia – Norte de Portugal (GNP-AECT) a través del programa IACOBUS destinado a desenvolver un sistema de intercambio transfronterizo en investigación.

ANEXO II:

Contribuciones a congresos

Parte del trabajo incluido en esta tesis doctoral ha sido presentado en los congresos que se detallan a continuación:

Pósters

- **ENHANCING THERMOELECTRIC CHARACTERISTICS OF POLYANILINES**; L. Horta Romarís, M.J. Abad López, M.V. González Rodríguez, A. Ares Pernas, A. Lasagabáster Latorre; XXXV Reunión Bienal de la Real Sociedad Española de Química, A Coruña (España) 19-23 julio de 2015.
- **TEMPERATURE DEPENDENCE OF ELECTRICAL CONDUCTIVITY FOR DBSA DOPED POLYANILINE SYNTHETIZED BY DIFFERENT ROUTES**; L. Horta Romarís, A. Ares Pernas, M.J. Abad, M. V. González-Rodríguez, A. Lasagabáster, P. Costa, S. Lanceros-Mendez; Organic Semiconductors Conference, Cavtat, Dubrovnik (Croatia) 22-25 septiembre de 2016.
- **THERMOELECTRIC PROPERTIES EVALUATION FOR INDIRECTLY DOPED POLYANILINE**; L. Horta Romarís, A. Ares Pernas, M.J. Abad, M. V. González-Rodríguez, A. Lasagabáster, F. Rivadulla Fernández; Organic Semiconductors Conference, Cavtat, Dubrovnik (Croatia) 22-25 septiembre de 2016.

Comunicación oral

- **COMPOSITES POLIANILINA-LÁTEX CON APLICACIONES TERMOELÉCTRICAS**; L. Horta Romaris, M. V. González Rodríguez, A. Lasagabáster Latorre, F. Rivadulla Fernández, M.J. Abad López; IX Congreso de Jóvenes Investigadores en Polímeros, Platja de la Pineda, Tarragona (España) 5-8 junio de 2017.

ANEXO III:

Portadas de artículos

Materials and Design 114 (2017) 288–296

Contents lists available at ScienceDirect

Materials and Design

journal homepage: www.elsevier.com/locate/matdes

Cyclic temperature dependence of electrical conductivity in polyanilines as a function of the dopant and synthesis method

Laura Horta-Romarís [a], María-José Abad [a,*], M. Victoria González-Rodríguez [a], Aurora Lasagabáster [a,b], Pedro Costa [c], Senentxu Lanceros-Méndez [c,d,e]

[a] Universidade da Coruña, Grupo de Polímeros, Centro de Investigacións Tecnolóxicas, Campus de Ferrol, 15471 Ferrol, Spain
[b] Dpto Química Orgánica I, Facultad de Óptica y Optometría, Universidad Complutense de Madrid, Arcos de Jalón 118, Madrid 28037, Spain
[c] Center/Department of Physics, University of Minho, Campus de Gualtar, 4710-057 Braga, Portugal
[d] BCMaterials, Parque Científico y Tecnológico de Bizkaia, 48160 Derio, Spain
[e] IKERBASQUE, Basque Foundation for Science, Bilbao, Spain

HIGHLIGHTS

- PANI-DBSA prepared by direct and indirect synthesis scalable to industrial volumes is a promising material as thermal sensor
- PANI-DBSA exhibits electrical linearity and reversibility in heating-cooling cycles
- Direct route leads to higher amplitude of electrical response in cyclic test
- Indirect route reduces moisture dependence of electrical conductivity

GRAPHICAL ABSTRACT

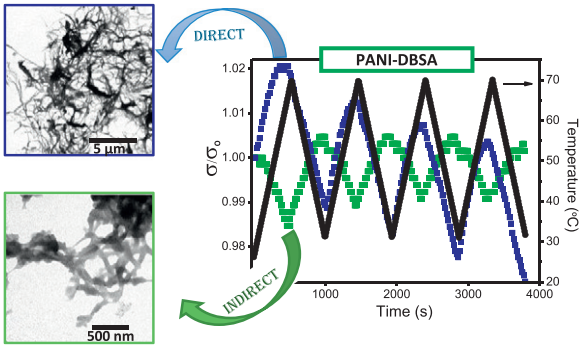

ARTICLE INFO

Article history:
Received 29 September 2016
Received in revised form 2 November 2016
Accepted 4 November 2016
Available online 9 November 2016

Keywords:
Polyaniline
NaSIPA
DBSA
Electrical conductivity
Heating-cooling cycles
Ageing

ABSTRACT

Most of the studies dealing with polyanilines (PANIs) are focused on electrochemical polymerization; however, chemical polymerization is more suitable for large–scale production. In order to develop commercially viable, clean, effective materials for thermal sensor devices, temperature dependent electrical response has been studied in PANIs obtained by simple, low-cost synthesis conditions, transferable to industrial processing. PANIs doped with HCl, dodecylbenzene sulfonic acid (DBSA) and sodio-5-sulfoisophtalic acid (NaSIPA) were prepared by chemical oxidative polymerization, through direct and indirect routes of synthesis. TEM images disclosed formation of nanorods and microfibrils. Microstructural analysis confirmed differences in doping level and crystallinity which were related with the PANI conductivity.

Two PANI-DBSA synthesized by direct and indirect methods, exhibit the best conductivity retention up to 150 °C. In cyclic tests, they show excellent performance after 4 heating-cooling cycles up to 70 °C. The amplitude of electrical response for PANI-DBSA obtained by direct synthesis is twice the value of PANI-DBSA prepared by indirect route. Conversely, the latter displays slightly better repeatability due to its lower moisture content. This study suggests that both PANI-DBSA are suitable for use in electronic applications, under ambient conditions below 150 °C, and are promising materials for temperature sensor applications.

* Corresponding author.
E-mail address: mjabad@udc.es (M.-J. Abad).

http://dx.doi.org/10.1016/j.matdes.2016.11.021
0264-1275/

Synthetic Metals 243 (2018) 44–50

Contents lists available at ScienceDirect

Synthetic Metals

journal homepage: www.elsevier.com/locate/synmet

Thermoelectric properties and intrinsic conduction processes in DBSA and NaSIPA doped polyanilines

Laura Horta-Romarís[a], M. Victoria González-Rodríguez[a], Aurora Lasagabáster[a,b], Francisco Rivadulla[c], María-José Abad[a,*]

[a] Universidade da Coruña Grupo de Polímeros, Centro de Investigacións Tecnolóxicas, Campus de Esteiro, 15471 Ferrol, Spain
[b] Dpto Química Orgánica I, Facultad de Óptica, Universidad Complutense de Madrid, Arcos de Jalón 118, Madrid 28037, Spain
[c] Centro de Investigación en Química Biolóxica e Materiais Moleculares, Campus Vida, Universidade de Santiago de Compostela, 15782, Santiago de Compostela, Spain

ARTICLE INFO

Keywords:
Conducting polymers
Polyaniline
Electrical conductivity
Seebeck coefficient
Thermoelectrical properties

ABSTRACT

Seeking to gain fundamental understanding of the thermoelectric (TE) behavior of polyanilines (PANIs), structure- property relationships of PANI nanorods, doped with dodecylbenzenesulfonic acid (DBSA) and 5-sulfoisophtalic acid sodium salt (NaSIPA), and prepared by an indirect synthetic route, are discussed in terms of the contribution of the acid concentrations on the thermoelectric properties.

The synergistic combination of high doping level and layer structure, accounts for the moderately high electrical conductivities (σ) and low constant Seebeck coefficients (α) of PANI-DBSA. Conversely, the poor doping ability of NaSIPA and low crystallinity degree explain the low electrical conductivities along with significant increases in Seebeck coefficient values. In relation to conduction mechanisms, PANI-DBSA shows a hopping behavior with a carrier concentration of $c \approx 0.49$ (hole type), while PANI-NaSIPA displays a diffusive regime, characteristic of degenerate metallic semiconductors, with an estimated charge carrier density of $n \approx 3 \times 10^{21}$ e/cm^3.

1. Introduction

The organic thermoelectric (TE) materials, as intrinsically conducting polymers (ICPs), are interesting candidates for green thermoelectric energy conversion applications, given their low cost and environmental safety [1–3]. The energy–conversion efficiency of a TE device is a function of the material's figure-of merit (ZT), average working temperature of the device and temperature difference between the hot and cold ends [4]. ZT is directly proportional to the electrical conductivity (σ) and the Seebeck coefficient (α) and inversely proportional to the thermal conductivity (κ) [1,2,4–6].

$$ZT = \frac{\sigma\alpha^2}{\kappa}T \quad (1)$$

Thus, a good thermoelectrical material should have high σ and α, but poor κ. The three thermoelectrical parameters are interdependent in bulk materials and decoupling these parameters is definitely non-trivial [7].

Polyaniline (PANI) as one of the important ICPs has caused a lot of scientists' interests due to high stability, facile synthesis and tunable electronic properties [8]. Electrical conductivity of PANI increases with doping, which may be achieved by an acid-base reaction. As a result of the protonation of the nitrogen sites in the emeraldine base (EB), the cation radical of one nitrogen acts as a polaronic hole and these holes are charge carriers (p-type doped PANI) [9] (Fig. 1). Electrical conductivity occurs via inter-polaron hopping along and across polymer chains [10,11]. Therefore, the carrier density depends on the degree of protonation or doping level [4,12]. Furthermore, in most cases PANIs appear to be amorphous, sometimes with some degree of crystallinity, thus heterogeneous conduction is set up involving "islands" of higher conductivity regions separated by lower conductivity regions. The polaron structures are responsible for electrical conduction through the hopping mechanism in the crystalline region [9], while intergrain resonance tunnelling occurs through the strongly localized states in the amorphous media [13]. These systems are featured with low charge carrier mobility and low electrical conductivities, even at high carrier densities [14,15]. This mixture of metallic and non-metallic behaviour is a key characteristic of all ICPs, including PANI [16].

By contrast, the Seebeck coefficient is more complex and difficult to predict. The reduction of the total number of charge carriers increase the Seebeck coefficient while lowering the electrical conductivity, but because the power factor (PF) scales with α^2, a net increase in the PF

* Corresponding author.
E-mail address: mjabad@udc.es (M.-J. Abad).

https://doi.org/10.1016/j.synthmet.2018.06.002
Received 18 April 2018; Received in revised form 31 May 2018; Accepted 5 June 2018

Journal of Materials Chemistry C

PAPER

View Article Online
View Journal | View Issue

Cite this: J. Mater. Chem. C, 2018, 6, 8502

Multifunctional electromechanical and thermoelectric polyaniline–poly(vinyl acetate) latex composites for wearable devices†

Laura Horta Romarís,[a] M. Victoria González Rodríguez,[a] Bincheng Huang,[b] P. Costa,[cd] Aurora Lasagabáster Latorre,[ae] S. Lanceros-Mendez[fg] and María José Abad López *[a]

This paper reports on the piezoresistive, thermoresistive and thermoelectric behaviour of polyaniline–poly(vinylacetate) (PANI–PVAc) nanocomposites prepared by simple, scalable, green latex technology. The relationship between the electrical properties and the PANI–PVAc ratio was analyzed in the framework of the percolation model and related to morphological and structural changes. Composites with 10, 20 and 30 wt% PANI combine suitable electrical conductivities and the beneficial mechanical properties of the polymer matrix, hardly decreasing the polymer matrix thermostability. They exhibit satisfactory electromechanical and thermoresistive properties for use in sensor applications. Both the gauge factor (GF) and thermal sensitivity decay for PANI contents beyond the percolation threshold. Composites with 10 wt% PANI achieve the highest GF up to 12 for 10% deformation and a thermal sensitivity of 0.25% C^{-1} between 20–40 °C, suitable for flexible and wearable temperature sensors for monitoring human health. Composites with 20 wt% PANI are appropriate for larger strain deformations and have superior fatigue resistance. The high electrical conductivities of samples with 20 and 30 wt% PANI are essentially preserved after large deformations of ~300%, which is important in the design of stretchable elastomer conductors; they both provide the best compromise between thermoelectric (*ZT*) and mechanical properties. This tunability together with the soft nature of the composites paves the way for low-cost, macroscale, diverse applications such as strain and temperature sensors in stretchable and wearable electronics.

Received 14th May 2018,
Accepted 20th July 2018

DOI: 10.1039/c8tc02327a

rsc.li/materials-c

1. Introduction

Recently, there have been remarkable accomplishments in the field of stretchable electronics including display panels, radio frequency electronics, light emitting diodes, acoustic devices, elastic conductors, smart sensors, artificial muscles, electronic skin health monitoring systems and other wearable devices.[1–6] Excellent mechanical properties combined with thermoelectric performance, and piezoresistive and thermoresistive properties are among the capabilities required for components used in the fabrication of integrated stretchable systems for the aforementioned applications.

The rapid development of next-generation stretchable electronics stimulates the urgent demand for novel, low-cost, ecofriendly, simple processing, light weight and flexible materials. Intrinsically conductive polymers (ICPs) such as polyaniline (PANI), poly(3,4-ethylenedioxythiophene) (PEDOT), PEDOT modified with polystyrenesulfonate acid (PEDOT/PSS) or polypyrrole (PPy) represent a fascinating class of materials that can fulfill these requirements and can be an alternative to the currently used commercial metallic and/or ceramics components, although to become competitive with present, novel materials they will need to increase in efficiency.[4,7–9]

PANI is the most investigated ICP both by academics and industry[7] and can be considered unique owing to its reversible doping/dedoping that affects its electrical conductivity by several

[a] Grupo de Polímeros, Centro de Investigacións Tecnolóxicas, Universidade da Coruña, Campus de Ferrol, 15471 Ferrol, Spain. E-mail: mjabad@udc.es
[b] Department of Automobile Engineering, School of Transportation Science and Engineering, Beihang University, Beijing, 100191, China
[c] Centre of Physics, University of Minho, 4710-057 Braga, Portugal
[d] Institute for Polymers and Composites IPC/I3N, University of Minho, 4800-058 Guimarães, Portugal
[e] Dpto Química Orgánica I, Facultad de Óptica, Universidad Complutense de Madrid, Arcos de Jalón 118, 28037 Madrid, Spain
[f] BCMaterials, Basque Center for Materials, Applications and Nanostructures, UPV/EHU Science Park, 48940 Leioa, Spain
[g] IKERBASQUE, Basque Foundation for Science, 48013 Bilbao, Spain

† Electronic supplementary information (ESI) available: Determination of the molecular weight of PANI; description of the home-made device employed to measure the Seebeck coefficient; detailed description of the FTIR spectra of pure components, characterization of the fraction of free and H-bonded polymer matrix and description of significant FTIR band shifts; degree of crystallinity of PANI within the composites from X-ray diffraction data and graph showing the changes in conductivity after tensile testing (PDF). See DOI: 10.1039/c8tc02327a